EFFECTS OF CLIMATE CHANGE ON SOIL EMBANKMENTS

Shubhra Pk

A Thesis Submitted to the Faculty of Graduate Studies
In Partial Fulfillment of the Requirements
For The Degree of
Master of Applied Science

Graduate Program in Civil Engineering
York University
Toronto, Ontario

September 2017

Abstract

The Intergovernmental Panel on Climate Change has reported that the climate change process will continue over the next century. The changes in climate variables can make the currently stable embankments unstable. It is therefore imperative that we understand how climate change will affect embankments. This research focuses on understanding and quantifying the effects of climate change on the stability of soil embankments in Ontario, Canada. The stability of embankments was analyzed for the current and future climates using numerical modeling technique. The effects of future climate were then quantified by comparing the future stability of embankments with its historical stability. The results of this research show that the effects of climate change also depend on the hydraulic properties of the fill materials. Embankments with sand fill withstand the adverse effects of climate change, and showed better performance over the embankments with silt fill.

Acknowledgements

My thanks go to my supervisors Dr. Rashid Bashir and Dr. Ryley Beddoe for their continuous support and encouragement throughout this research.

I would also like to acknowledge the help and support of the Ministry of Transportation, Ontario (MTO). This project would not have been possible without them and their support. I also want to acknowledge the support of PC-Progress engineering software developer and Geo-Slope International Limited during the model development stage of this work. Thanks also go to the Laboratory of Mathematical Parallel Systems, York University; Institute for Energy, Environment and Sustainable Communities, University of Regina; and Environment Canada for sharing their climate data.

Thanks also to Dr. Jit Sharma and Dr. Usman T Khan, York university for their help and advice during the model development and data processing stages of this research.

Table of Contents

List of Tables

List of Figures

List of Abbreviations

AE	Actual Evaporation
AEV	Air Entry Value
AT	Actual Transpiration
BC	Baseline Climate
DC	Design Climate
CCDP	Climate Change Data Portal
DD	Dry Density
DTM	Digital Terrain Model
FC	Future Climate
GCM	General Circulation Model
GTA	Greater Toronto Area
GUI	Graphical User Interface
HCF	Hydraulic Conductivity Function
IDF	Intensity, Duration, Frequency Curve
IPCC	Intergovernmental Panel on Climate Change
IEESC	Institute of Energy, Environment and Sustainable Communities
LAMPS	Laboratory of Mathematical and Parallel Systems
MTO	Ministry of Transportation, Ontario
NOAA	National Oceanic and Atmospheric Administration
OC	Organic Content
OCCP	Ontario Climate Change Projections
OPSS	Ontario Provincial Standard Specification
PTF	Pedotransfer Function

PWP	Pore-Water Pressure
RCM	Regional Climate Model
SRES	Special Report on Emission Scenario
STDV	Standard Deviation
SWCC	Soil Water Characteristic Curve
USDA	United State Department of Agriculture
VG	van Genuchten
WG	Weather Generator
WH	Water Content at Fixed Capillary Pressure

List of Symbols

Γ	Slope of saturated vapor pressure versus temperature curve
Q_n	Net radiation at the water (or saturated) surface
η	Psychrometric constant
E_a	A function of wind speed and vapor pressure deficit
W_w	Wind speed
u_v^{air}	Vapor pressure in the air above the water surface
u_{v0}^{air}	Saturated vapor pressure at the mean air temperature
L_d	Length of daylight
N	Number of days in a month
T_a	Average monthly air temperature
I	Annual heat index
a_t	Complex function of the variable I
P	Precipitation
PE	Potential evaporation
PE_m	Monthly potential evaporation
NI	Net infiltration
RO	Runoff
T_{ef}^*	Effective air temperature
$T_{\max}$	Maximum air temperature

T_{avg}	Average air temperature
T_{mir}	Minimum air temperature
h	Pressure head at the soil surface
E	Maximum potential rate of evaporation or infiltration
h_A	Minimum allowed pressure head under the prevailing soil conditions
h_S	Maximum allowed pressure head under the prevailing soil conditions
R	Gas constant
T	Temperature
M	Molecular weight of water
g	Gravitational acceleration
I_m	Annual moisture index
Q	Volume of water flowing per unit time
K_{sat}	Saturated hydraulic conductivity
$K(h)$	Unsaturated hydraulic conductivity
i	Hydraulic gradient
A	Cross-sectional area
τ_f	Shear stress at failure
c'	Effective cohesion
$(\sigma-u_w)_f$	Effective stress at failure
σ	Total normal stress
σ_{ff}	Total normal stress on the failure plane at failure

σ'	Effective stress
c'	Effective friction
S	Shear strength of soil
u_{wf}	Pore-water pressure at failure
ϕ'	Effective angle of internal friction
θ	Volumetric water content
θ_s	Saturated volumetric water content
θ_r	Residual volumetric water content
ψ	Suction
ψ_r	Suction Corresponding to residual water content
a, m_1, n_1	Fitting parameters for the SWCC model of vn Genuchten (1980)
α, m_2, n_2	Fitting parameters for the SWCC model of Fredlund and Xing (1994)
t	Time
u_a	Pore-air pressure
u_w	Pore-water pressure
χ	Pmpirical parameter for the effective stress equation of Bishop (1959)

Chapter 1. Introduction

1.1 Introduction

Global surface temperatures have shown a rising trend in last two centuries. The Intergovernmental Panel on Climate Change (IPCC) has reported that the global mean surface temperature has increased by 0.85°C since 1880 (IPCC 2013). In Canada the increase in mean surface temperature between 1950-2010 is 1.5°C which is almost double the global average (Environment Canada 2011a). However, this increase in surface temperature in Canada is not uniform across the year. Winter and Spring temperatures have shown the highest increases, while Fall temperature has shown the lowest increase (Vincent et al. 2012). Along with temperature, other climate variables such as precipitation also has shown noticeable increment. As a whole, total annual precipitation has increased by 16% across Canada between 1950-2010 (Mekis and Vincent 2011). Like temperature, precipitation also has shown temporal variability. Annual rainfall has shown an increasing trend over most of Canada. Meanwhile snowfall has shown a decreasing trend in southern Canada, where snowfall is gradually shifting to rainfall (Mekis and Vincent 2011). In addition, a noticeable increase has been observed in the frequency of extreme precipitation events in Canada between 1950-2010 (Vincent and Mekis 2006).

When trying to understand changes in the climate, historical climate records are used to benchmark typical climate trends over long periods of time. Based on these trends and future socio-economic storylines, the future greenhouse gas emission scenarios are predicted. The future climate can then be predicted based on the emission scenarios using general circulation models (GCMs). GCMs are the most advanced tools currently available for simulating the response of the global climate system to increasing greenhouse gas concentrations. A significant number of GCMs have been developed in various research centers around the world, and are used to predict future climate.

The predicted future surface temperature follows the historical increasing trend. The overall projected surface temperature shows an increase in the length, frequency and intensity of warm spells and heat waves over most of the land areas, including Canada (Natural Resources Canada 2014). It has been predicted that the mean surface temperature could increase by as much as 10°C in some parts in northern Canada within this century (Government of Canada 2010b). Like the historical climate, the future surface temperature in Canada is also expected to show more prominent increase in winter than in summer. The average annual precipitation also shows an increasing trend over the Canada. It is predicted that the winter precipitation could increase significantly over Canada, while summer precipitation could decrease in some parts of southern Canada (Government of Canada 2010b). Therefore, the future summers could be warmer and dryer, and the winters could be warmer and more wet. The frequency of heavy precipitation events could increase significantly, and the rare events are projected to become about twice as frequent by the mid-century over most of Canada (Natural Resources Canada 2014). A significant declining trend in snow cover days is also predicted over Canada, especially in southern Canada. These changes in climate variables have the potential for negative, possibly catastrophic effects on geotechnical infrastructure, especially those that rely heavily on their water balance for strength, such as soil embankments.

Soil embankments are widely used as foundations in transportation networks, and as water retention infrastructures. Canada has over 1 million km of roads and 72, 000 km of railways linking the country together. Ontario has approximately 16,500 km of highways, with over 30% in the Greater Toronto Area (GTA) alone. The foundations of these roads and railways are often constructed on top of soil embankments. These embankments are exposed to the atmosphere, and their strength and stability largely depend on climate. Climate primarily affects embankments through infiltration and evaporation of water. When water infiltrates into the embankments, they can become saturated with increases in weight and pore pressures. Consequently, the effective stresses within the embankments decrease, resulting in a loss of shear strength. When water is evaporated through the ground surface, the embankments become unsaturated which leads to a decrease in pore pressures, and consequently increase in effective stress and shear strength within the soil. In an unsaturated soil, matric suction develops within the pore spaces due to capillary action. This suction also could increase shear strength within the unsaturated soil. Therefore, it is clear that the climate variables play a vital role in the strength and stability of embankments.

The water infiltration and evaporation processes at the ground surface are generally controlled by the prevailing climatic condition and soil water content. Water comes from the atmosphere in the form of precipitation. A portion of this precipitation is trapped by leaves, tree branches and the forest floor, and then evaporated, which is called interception. After interception loss, the precipitation reaches to the ground surface. A portion of this precipitation flows over the ground as overland flow (if the precipitation rate exceeds the infiltration rate), and rest of it infiltrates into the ground. The overland flow on a slope depends upon several factors including slope angle, vegetation, and roughness of sloping surface. The infiltration rates primarily depend upon the hydraulic conductivity of soil. However, hydraulic conductivity of a soil is not constant, and changes with soil suction.

The total amount of water that infiltrates into the ground can impact the pore pressures and stability of embankments. However, a significant portion of this water is extracted through the ground surface as actual evaporation, and through the plant roots as actual transpiration. These two processes by which water moves upward from the ground surface are collectively called actual evapotranspiration. The maximum potential evapotranspiration rate can be calculated from the climate variables such as air temperature, relative humidity, wind speed, and net radiation. The actual evapotranspiration rate then can be estimated from the potential evapotranspiration rate, available soil water near the ground surface, and vegetation characteristics. The remain amount of water in the ground after the actual evapotranspiration loss is called net infiltration. The net infiltration can be positive or negative based on the amount of actual evapotranspiration.

The relation between the stability of soil embankments and climate variables along with the major governing hydrogeological processes have been discussed in the previous paragraphs. It is clear that the climate variables have potential to affect the stability of soil embankments. Therefore, it is critical now more than ever that we understand how climate change will affect the stability of soil embankments.

1.2 Thesis Objectives

The primary objective of this thesis is to quantify the impacts of future climate change on soil embankments, with a specific focus on soil embankments in Toronto, Ontario. To achieve this objective, the following works have been completed:

I. Literature review (with emphasis on hydrological and geotechnical modeling of embankments);

II. Identification and selection of a suitable combination of hydrological and geotechnical modeling software;

III. Selection of design parameters including design profile, geological and groundwater settings;

IV. Estimation of unsaturated hydraulic properties of soil;

V. Collection, processing, and analysis of historical and future climate data, and construction of design climate events;

VI. Development of soil-atmospheric and slope stability models;

VII. Conducting soil-atmospheric and slope stability analyses of soil embankments for the selected design parameters

VIII. Assessment of modeling procedures, and review of results

1.3 Thesis Outline

This thesis is presented in a chapter format. Chapter 1 is a general introduction, including overarching research objectives. Chapter 2 is a literature review of relevant research areas. Chapter 3 through 5 present the selection of embankments design parameters and study methodology. The results of this research are presented in Chapter 6, followed by the conclusions in Chapter 7.

1.3.1 Chapter 2

This chapter presents a review of the previous related studies, and the processes involved in the modeling of climate change impacts on slopes. It starts with the quantification of the water balance at the ground surface. The compilation and application of the historical and future climate data are then discussed briefly. The effects of partial saturation on the physical properties of soils are then reviewed along with the mathematical models used to express the behavior of unsaturated soil. The next part of this chapter presents a review of the commonly used hydrological and geotechnical modeling programs. The last part of this chapter presents a detailed review of the related previous studies.

1.3.2 Chapter 3

Chapter 3 presents pertinent details of historical and future climate of Toronto. Firstly, the historical climate of Toronto is analyzed based on 30 years of recorded data. Then, the potential sources of climate change information for Ontario are identified. The quality of this climate change information is then assessed by comparing the measured and back-predicted model results. Based on this performance analysis, recommendations are made to select a suitable source of future climate information for Ontario. The future 90 years of climate data is then collected from the selected source, and analyzed to understand probable changes in future climate. The results are compared with the historical climate to construct embankment design climate. Finally, the design climate is selected to conduct numerical modeling.

1.3.3 Chapter 4

The selection of the embankment design parameters, including design profile, generalized geology, and groundwater settings are discussed at the beginning of this chapter. The second part of this chapter presents the estimation of soil hydraulic properties, and selection of soil properties for the numerical modeling.

1.3.4 Chapter 5

Chapter 5 outlines the methodologies employed in this study. Methodology to simulate pavement in highway embankments is also discussed in this chapter. The detailed procedures of the development of the hydrological and geotechnical models, and their coupling technique are presented towards the end of the chapter.

1.3.5 Chapter 6

This chapter contains the results. The results are presented in two separate sections based on two sets of design climates. The first part of chapter 6 presents the results for the first set of design climate. The first set of design climate contains historical and future climate ensembles comprising of 30 years of climate data. The second part of chapter presents the results of second set of design climate based on historical and future intensity duration and frequency (IDF) curves. A comparison between the historical and future stabilities of the embankments is then presented to understand potential impacts of climate change. This chapter concludes with the review of the results.

1.3.6 Chapter 7

Chapter 7 presents the major findings, and conclusions of this research. The impacts of this research are also presented in this chapter. This chapter concludes with recommendations for future research.

Chapter 2. Literature Review

2.1 Introduction

Soil embankments for transportation networks are typically constructed by cut and fill. The fills are usually raised above the ground surface, and remain unsaturated in most instances. The pore space of unsaturated soils is filled with both air and water (Fredlund et al. 2012). The presence of both air and water in pore space results in matric suction, which allows soil to maintain a slope stepper than their angles of repose (Fredlund et al. 2012). Therefore, stability of these embankments is largely governed by the amount of water and air present in soil pores. Since the amount of water and air in soils is controlled by the climatic parameters, any change in these climatic parameters could affect the stability of embankments. For example, an increase in precipitation will allow more water to seep into the soil, and consequently reduce its strength which could make the slope vulnerable. On the contrary, increased temperature, and decreased precipitation have the potential to make an embankment dry out and shrink. Therefore, it is important to understand the interaction between the climate and ground surface, and how it influences the embankments stability.

2.2 Ground Surface Water Flux

The embankments are exposed to the atmosphere. The ground surface is the boundary between the soil and the atmosphere. The exchange of water between the soil and the atmosphere occurs through this boundary. For example, this boundary is periodically exposed to precipitation in the form of rain or snow. The snow will either accumulate at the ground surface, or can quickly melt and behave like rain. At other times water moves upward from the ground surface as evaporation and transpiration. Quantifying the magnitude and direction of the water flux across the ground surface is important in all subsurface water movement studies. However, determination of the net water flux at the ground surface is challenging, and contains numerous complexities (Fredlund et al. 2012).

Quantification of the net water flux at the ground surface requires climate, soil, and vegetation data (Davies 2011). The climate variables can be measured at weather stations, while the soil and vegetation properties can be determined either in the laboratory or in the field (Fredlund et al. 2012). The commonly required climate variables are precipitation, temperature, relative humidity, wind speed, and solar radiation. A portion of the precipitation can infiltrate into the ground, and can move downwards or laterally. If the rate of precipitation is greater than the infiltration capacity of the soil, surface runoff is generated. Evaporation and transpiration are functions of the other four above-mentioned climate variables and are responsible for the movement of the water from the soil to the atmosphere (Fredlund et al. 2011).

The components of the ground surface water flux and the net infiltration at the ground surface can be written as follows:

$$NI = P - AE - AT - RO \tag{2.1}$$

where:

$NI =$ net infiltration, mm/day,

$P =$ precipitation, mm/day,

$AE =$ actual evaporation, mm/day,

$AT =$ actual transpiration, mm/day, and

$RO =$ runoff, mm/day.

To estimate *NI* at the ground surface, each of the components of the water balance must be estimated accurately. However, the computational procedures are complex, and contain numerous assumptions (Davies 2011). Fredlund et al. (2012) presented a detailed analysis on these computational procedures, and has concluded that the calculation of *AE* is the most critical and challenging component. They have also suggested that the physics associated with the determination of *PE* must be fully understood prior to the estimation of *AE*.

2.2.1 Potential evaporation

The potential evaporation (*PE*) is the maximum amount of water that can evaporate from the ground surface if plentiful water is available. The availability of the thermal energy at the ground surface, and the ability of the lower atmosphere to transport water vapor away from the ground surface are the two primary factors controlling the *PE* (Fredlund et al. 2011). *PE* is higher on a sunny and windy day, when the net radiation, and wind speed are higher. The higher net radiation provides more thermal energy at the ground surface, and the higher wind speed quickly removes the vapor-saturated air above the ground surface to enhance evaporation.

Potential evaporation can be estimated from the climate variables or can be measured directly using an evaporation pan. The climate variables required for the estimation of *PE* are routinely measured at most weather stations. A significant number of studies have been conducted since the 1920s to estimate the amount of *PE* (Pereira and Pruitt 2004), and several mathematical relationships have been proposed (e.g., Penman 1948, Thornthwaite 1948). Each of the proposed relationships uses specific weather data. The commonly used *PE* estimation equations in geotechnical engineering are summarized in the following sections.

Penman (1948) equation: The Penman equation uses routine weather data such as air temperature, relative humidity, wind speed, and net radiation as input. The Penman equation can be written as follows:

$$PE = \frac{\Gamma Q_n + \eta E_a}{\Gamma + \eta} \tag{2.2}$$

where:

$PE =$ potential evaporation, mm/day,

$\Gamma =$ slope of saturated vapor pressure versus temperature curve, kPa/°C,

$Q_n =$ net radiation at the water (or saturated) surface, mm/day,

$\eta =$ psychrometric constant, kPa/°C,

$E_a =$ a function of wind speed and vapor pressure deficit,

$$2.625(1+0.146W_w)(u_{v0}^{air} - u_v^{air}), mm/day,$$

$W_w =$ wind speed, km/h,

$u_v^{air} =$ vapor pressure in the air above the water surface, kPa, and

$u_{v0}^{air} =$ saturated vapor pressure at the mean air temperature, kPa.

The Penman (1948) equation considers the vapor pressure gradient between the water surface and the air above the water surface as the primary controlling parameter for evaporation. The performance of this equation is validated by comparing results with pan evaporation and evaporation from lake surface, and satisfactory results are obtained (Fredlund et al. 2012, Dingman 2015). However, applications of this method could be restricted due to large number of input variables.

Thornthwaite (1948) equation: The primary input variables require for the Thornthwaite (1948) equation are the mean monthly temperature, the length of daylight hours, and an empirical constant. The Thornthwaite equation calculates daily *PE*, and for a month of 30 days and 12 hours of average daylight length, can be written as follows:

$$PE = 0.533\left(\frac{L_d}{12}\right)\left(\frac{N}{30}\right)\left(\frac{10T_a}{I}\right)^{a_t} \tag{2.3}$$

where:

$PE =$ potential evaporation, mm/day,

$L_d =$ length of daylight, hr.,

$N =$ number of days in the month,

$T_a =$ average monthly air temperature, °C,

$I =$ annual heat index, sum of the function $(T_a/5)^{1.514}$ for 12 months, and

$a_t =$ Complex function of the variable I;

$$a_t = (6.75\times10^{-7})I^3 - (7.71\times10^{-5})I^2 + (1.79\times10^{-2})I + 0.492.$$

The Thornthwaite equation uses mean monthly air temperature, and calculates daily *PE* from the length of daylight hours. This equation gained widespread acceptance since it requires only average monthly temperature as input (Pereira and Pruitt 2004).

Pereira and Pruitt (2004) equation: The Pereira and Pruitt (2004) equation is a modified form of the Thornthwaite (1948) equation. The Thornthwaite equation has been found to underestimate *PE* under arid conditions (Pelton et al. 1960, Stanhill 1961, Pruitt and Doorenbos 1977, Malek 1987), and overestimates *PE* for certain humid climates (Camargo et al. 1999). Pereira and Pruitt (2004) proposed an adjustment to the Thornthwaite (1948) equation after Camargo et al. (1999). The modified equation requires daily maximum and minimum air temperature data in addition to the daily average data. The potential evaporation for a standard month of 30 days, each day with 12 hours of daylight was computed by Thornthwaite as a function of the mean monthly temperature as follows:

$$PE_M = 16\left(10\frac{T_a}{I}\right)^{a_t} \qquad 0°C \le T_a \le 26°C \tag{2.4}$$

$$PE_M = -415.85 + 32.24T_a - 0.43T_a^2 \qquad T_a > 26°C \tag{2.5}$$

where:

$PE_m =$ monthly potential evaporation, mm/month.

Pereira and Pruitt (2004) replaced the average monthly air temperature of the Thornthwaite's equation by the effective average monthly air temperature. The daily effective average air temperature equation can be written as follows:

$$T_{ef}^* = [\frac{1}{2}k(3T_{\max} - T_{\min})]\frac{L_d}{24 - L_d} \quad T_{avg} \le T_{ef}^* \le T_{\max} \tag{2.6}$$

where:

$T_{ef}^* =$ effective air temperature, °C,

$k =$ constant, a recommended value for k is 0.69

$T_{\max} =$ maximum air temperature, °C,

$T_{avg} =$ average air temperature, °C, and

$T_{\min} =$ minimum air temperature, °C.

In order to convert the estimated monthly *PE* to daily time scale the following correction factor (*C*) was applied using the length of daylight hours:

$$C = \frac{L_d}{360} \tag{2.7}$$

Pereira and Pruitt (2004) validated their proposed adjustment of the Thornthwaite's equation by comparing the estimated values with lysimeter measurements. The authors reported that a good agreement was observed between the estimated and measured values.

2.2.2 Actual evaporation

Actual evaporation (*AE*) is the actual amount of water that can be evaporated from the soil surface. The geotechnical engineers require the *AE* to calculate water balance at the ground surface. The *AE* from a soil surface might be considerably lower than the *PE* (Fredlund et al. 2011). The net radiation and wind are the two major climate variables that control the *PE*, while the soil suction plays an important role for the *AE*. The *AE* rate from a saturated soil surface can be assumed equal to the *PE*. But, when the soil begins to dry, it tries to hold onto the water more strongly. In other word, the soil suction increases as the soil dries. This increased suction tries to hold the soil water, while the net radiation and wind try to evaporate. Consequently, the evaporation rate from the soil surface gradually decreases with the increase in soil suction (i.e., *AE*).

Several methods have been proposed for *AE* calculations; however, these methods differ mainly on the assumptions related to the air and soil temperatures (Fredlund et al. 2011). The difference between the air temperature and the ground surface temperature gives rise to various coupled and uncoupled moisture and heat flow formulations. Fredlund et al. (2012) compiled three *AE* calculation methods, two of which are based on thermodynamics, and one is based on experiment. These three methods are: (i) the Wilson-Penman method (Wilson 1990), (ii) the limiting function method (Wilson et al. 1997), and (iii) the experimental-based method (Wilson et al. 1997). Wilson et al. (1994) modified the Penman (1948) equation to calculate *AE* by considering the difference in temperature and relative humidity between the air and soil surface, which became known as the Wilson-Penman equation. The limiting function method was proposed by Wilson et al. (1997) to calculate *AE* from the *PE*. This method calculates relative humidity at the ground surface and at the air above the ground surface based on an assumption that the air and soil temperatures are same. The experimental-based method also was proposed by Wilson et al. (1997). A unique relationship between total suction and the ratio between actual and potential evaporations for soils was developed. The experimental method shows that the soil suction at the ground surface primarily controls the actual evaporation. Finally, the authors proposed an equation of *AE* calculation that fits the experimental data.

The above discussed three *AE* calculation methods have been used in many computer codes to develop soil atmospheric models. For example, the Wilson-Penman method is implemented in the SoilCover (Wilson 1993) and SVFlux computer codes (Fredlund 2001). This *AE* calculation methods also is used in the VADOSE/W, a module of GeoStudio package (Geo-Slope International Ltd. 2014a). However, some other techniques have been used in other computer codes. For example, a system depended boundary condition using an approach proposed by Neuman et al. (1974) is implemented in HYDRUS (Šimŭnek et al. 2016). This boundary condition limits the absolute value of fluxes by satisfying following two conditions:

$$\left| -K(h)\left(\frac{\partial h}{\partial x}+1\right) \right| \le E \tag{2.8}$$

and

$$h_A \le h \le h_S \tag{2.9}$$

where:

$h =$ pressure head at the soil surface, m,

$E =$ maximum potential rate of evaporation or infiltration, m/s,

$h_A =$ minimum allowed pressure head under the prevailing soil conditions, m,

$h_S =$ maximum allowed pressure head under the prevailing soil conditions, m.

The value of h_A can be calculated from the air Humidity, H_r, as follows (Šimŭnek et al. 2016):

$$h_A = \frac{RT}{Mg}\ln(H_r) \tag{2.10}$$

where:

$R =$ gas constant, 8.31×10^3 N m kmol^{-1} K^{-1},

$T =$ temperature, K,

$M =$ molecular weight of water, 18.02 g/mol,

$g =$ gravitational acceleration, 9.81 m/s^2.

When the potential evaporation rate exceeds the capability of the soil to deliver enough water toward the soil surface the system dependent boundary condition occurs. In this case the *PE* reduces to an *AE* rate that is again controlled by the soil. Feddes et al. (1974) have discussed details of the methods for calculating *E* and h_A on the basis of atmospheric data.

2.2.3 Transpiration

Actual evaporation accounts the movement of water from the ground surface to the air. While the term transpiration uses to describe the movement of water within plants and the subsequent loss of water through stomata. The *AE* from the ground surface plus the *AT* from plants form the term actual evapotranspiration (Fredlund et al. 2012).

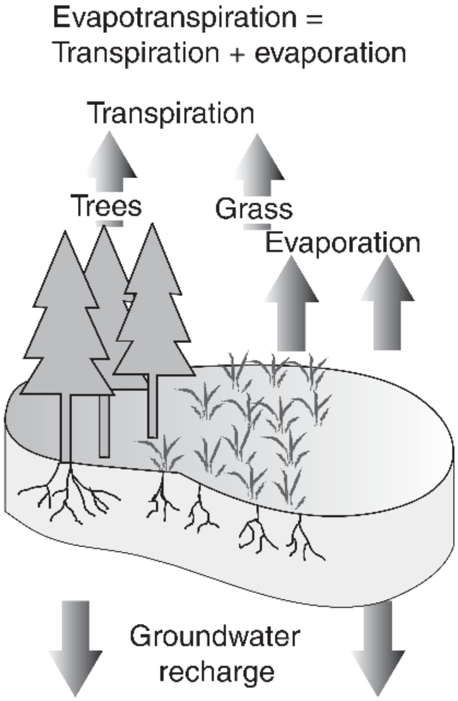

Figure 2.1 Components of evapotranspiration (Fredlund et al. 2012)

The mechanisms of *AE* and *AT* along with the formation of evapotranspiration is shown in Figure 2.1. The quantification of the transpiration flux primarily depends upon the soil profile at root zones as well as the characteristics of vegetation (Rouainia et al. 2009). The influencing vegetation characteristics include the size and number of stomata, their functions, and the leaf area (Tindall et al. 1999). Tratch (1995) provided a four-step methodology to calculate transpiration flux from the *PE* and plant characteristics. The vegetation type varies widely from one site to another, and therefore Rushton (2004) suggested to establish a reference crop. The characteristics of all other crops then can be determined by relating with the reference crop.

2.2.4 Runoff

Runoff is generated if the precipitation intensity exceeds the infiltration capacity of the soil or if the groundwater table rises to the ground surface and prevents further infiltration (Davies 2011). Modeling runoff is extensively used in surface water hydrology, and there are many watershed models those are capable of modeling runoff. Borah and Bera (2003) reviewed the available governing flow equations for runoff, and classified them into five categories as follows: (i) Dynamic wave equations, (ii) Diffusive wave equations, (iii) Kinematic wave equations, (iv) Storage-based or nonlinear reservoir equations, and (v) Curve number and empirical equations. Each of these equations offer varying degrees of simplicity, accuracy, and, modeling efficiencies. For example, the physically based runoff models using the dynamic wave equations and diffusive wave equations are suitable for small areas where detailed study is required, while for larger catchment areas more simplified methods are more suitable. Therefore, selection of these models depends upon the requirements of the users.

2.3 Climate classification

Climate classification in geotechnical engineering is based on the calculation of water balance at the ground surface (Fredlund et al. 2012). It provides an estimation of water availability or scarcity at the ground surface at a particular site. Geotechnical engineers frequently use climate classification in their projects related to water balance, and infiltration. For example, for design of soil cover systems, it is important to understand the long-term climatic conditions at the initial design stage. Climate classification also facilitates an understanding of the trend of long-term climate, and is frequently used in the climate change studies (e.g., McCabe and Wolock 1992, Whitfield and Cannon 2000, Grundstein 2008, Tabari and Hosseinzadeh Talaee 2013, Leao 2014).

Geotechnical engineers commonly use the climate classification system proposed by Thornthwaite and Hare (1955) (e.g., Bashir et al. 2015). This climate classification system is based on the calculation of an annual moisture index that takes into consideration the annual P and PE. The precipitation data can be collected from the weather stations, while the PE can be estimated using standard methods such as Penman (1948) and Thornthwaite (1948). The equation of the annual moisture index can be written as follows:

$$I_m = 100\left(\frac{P}{PE} - 1\right) \tag{2.11}$$

where:

$I_m =$ annual moisture index,

$P =$ total annual precipitation, and

$PE =$ total annual potential evaporation calculated as the sum of the monthly potential evaporation calculated using equation (2.4.

The I_m values can be calculated from the ratio between annual P and PE. The climate type then can be determined using the Thornthwaite climate classification criteria, which are shown in Table 2.1. A I_m value of zero indicates neutral or zero water balance at the ground surface. A positive I_m value means a surplus of net water, and the climate is in wet side of the classification system (i.e., Moist humid to Perhumid). While a negative I_m value indicates a scarcity of net water, and the climate is in dry side (i.e., Dry Subhumid to Arid).

Table 2.1 Criteria for climate classification (Thornthwaite 1948)

I_m	Category of climate
>100	Perhumid
20 to 100	Humid
0 to 20	Moist humid
-33 to 0	Dry subhumid
-67 to -33	Semiarid
-100 to -67	Arid

2.3.1 Seasonal considerations

In many regions in Canada the temperature remains below zero for several months (Fredlund et al. 2012, Bashir et al. 2015). During this period, the ground surface is frozen and there is little to no water movement through the ground surface. Therefore, the evaluation of net water flux at the ground surface can be different during various times of the year, and partitioning of each year is helpful to understand the ground surface water movement.

A sketch with tentative partitioning of annual climate is shown in Figure 2.2. In winter, the atmosphere as well as the ground are frozen, and this period is usually defined as the inactive period (Fredlund et al. 2012, Bashir et al. 2015). The precipitation in inactive periods commonly comes in the form of snow, and accumulates over the ground surface. A portion of this snow is moved away by the wind, and rest of it remains at the ground surface. At the beginning of the spring, when the temperature rises above freezing and the ground thaws, a portion of the accumulated precipitation of inactive period infiltrates into the ground and the rest of it flows over the ground as surface runoff.

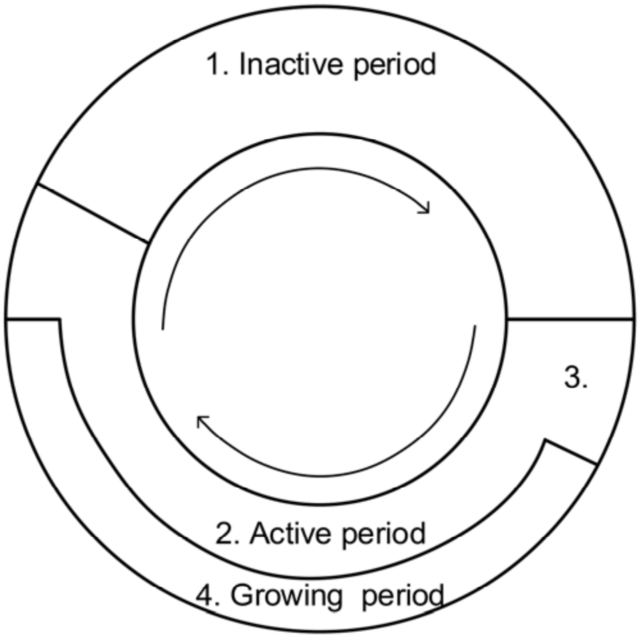

Figure 2.2 Partitioning of annual climate in active and inactive portions (modified from Fredlund et al. 2012)

The area 1 in Figure 2.2 shows the length of inactive period, and area 3 shows the portion of spring time when the accumulated precipitation of inactive periods melts. From the end of an inactive period to the start of the next inactive period, the atmosphere and ground both remain unfrozen. This period is defined as active period (area 2 in Figure 2.2). A portion of the active period is defined as growing period, which is area 4 in Figure 2.2. A growing period starts with the seeding date when 10 days average daily temperature is above 5°C, and continue until fall frost when minimum daily temperature is 0°C or until October 31st, whichever comes first (Government of Canada 2013).

2.4 Predicting the Future Climate

The observed changes in historical climate trends have driven the need to predict future climate. A significant number of climate models have been developed around the world to predict the future climate. These models incorporate the physical processes and interactions of atmosphere, ocean, land surface, biosphere, and cryosphere in various complexities, and are used as an important tool to understand climate and climate change (IPCC 1996). However, before applying a model for future climate prediction, it is important to assess its ability to predict historical climate first. If satisfactory performance is observed, the model can be applied to predict future climates for various scenarios of future greenhouse gas and aerosol emissions (Halifax Regional Municipality 2007). The outputs from the climate models are often across a large spatial scale, which needs to be downscaled for them to be useful at the regional and municipal scale. Davies (2011) has outlined the challenges of generating small scale climate change data, and suggested to take special care when downscaling.

2.4.1 Climate models

The most advanced and commonly used climate models are the atmospheric and oceanic general circulation models (GCMs) (IPCC 1996). Besides atmosphere and ocean, these models also consider other climate system related complex processes including land surface processes, and sea ice related processes. GCMs are primarily based upon physical laws that describe the atmospheric and oceanic dynamics and physics. The physical laws are incorporated using mathematical equations, and these equations are solved numerically using a three dimensional grid over the globe (IPCC 1996). Typically, GCMs have a horizontal resolution of 250 km and a vertical resolution of 1 km (IPCC 1996).

There are a number of GCMs used around the world, all with a varying degree of capability of projecting future climates (Flato et al. 2013). The validation results of these models often vary and therefore, it is important to review the maturity and performance of the GCMs before selecting them (Flato et al. 2013). The most recent Canadian models are the fourth generation coupled global climate model (CGCM4/CanCM4), and the Canadian earth system model (CanESM2) (Government of Canada 2010a).

2.4.2 Future emission scenarios

The IPCC recommends that a scenario of future climate can be developed based on several assumptions concerning future greenhouse gas emissions. To maintain consistency in climate change research and modelling around the world, the IPCC decided to publish global climate change scenarios to be used by anyone. The first set of emission scenarios was published in 1992, called IS92 (Wayne 2013). In the year 2000, a second generation of projections was released by IPCC, which was collectively referred to as the special report on emission scenarios (SRES) (Wayne 2013). The same emission scenario was used in the next two subsequent reports; the third assessment report (TAR) and assessment report four (AR4).

Their latest assessment report (AR5) was published in 2014, and used a different approach than their previous scenarios for generating plausible trajectories (Wayne 2013). The new scenarios are called representation concentration pathways (RCPs). There are four pathways: RCP2.6, RCP4.5, RCP6.0, and RCP8.5. Each of the pathways contains a set of starting values and the estimated emissions up to 2100 which is defined as radiative forcing (Wayne 2013). The RCPs are named based on the radiative forcing target level for 2100, and the radiative forcing estimates are based on the assumptions on greenhouse gas emissions and other forcing agents (Vuuren et al. 2011). A detailed description of RCPs can be found in Vuuren et al (2011), with a brief overview as follows:

RCP2.6 is an aggressive greenhouse gas mitigation pathway. It considers that the radiative forcing reaches to peak at 3 W/m^2 (~490 ppm CO_2 eq) before 2100, and then gradually declines to 2.6 W/m^2 by 2100.

The second and third representation concentration pathways, RCP4.5, and RCP6.0 are called stabilization scenarios. The medium-low RCP4.5 scenario considers that the radiative forcing stabilizes at 4.5 W/m^2 (~650 ppm CO_2 eq) by 2100. The RCP6.0 is considered as medium-high scenario. This scenario assumes that the radiative forcing stabilizes at 6 W/m^2 (~850 ppm CO_2 eq) by 2100.

The fourth pathway, RCP8.5 is based on very high baseline emission scenario. This pathway considers that the radiative forcing reaches to 8.5 W/m^2 (~1370 ppm CO_2 eq) by 2100, and then keeps increasing.

2.4.3 Downscaling

The spatial resolution of GCMs is quite large (often 250 km to 500 km grids), and therefore, the outputs of these models need to be downscaled before it can be used at a regional or municipal level. The downscaling approaches can be classified into three broad categories; simple, statistical, and dynamical. The simple downscaling contains adding coarse scale climate changes to higher resolution observations (the delta approach), and more sophisticated – interpolation of coarser resolution results (Giorgi and Mearns 1991). The statistical downscaling is a two-step process consisting of i) the development of statistical relationships between local climate variables (e.g., surface air temperature, precipitation) and large-scale predictors (e.g., pressure fields), and ii) the application of such relationships to the output of GCMs to simulate local climate characteristics in the future. The dynamical downscaling contains application of regional climate models (RCMs) using GCMs boundary conditions. These models use physical principles to reproduce local climates, but are computationally intensive. Oftentimes, dynamical and statistical approaches are used in conjunction, and are called dynamical-statistical or statistical-dynamical downscaling.

The Institute of Energy, Environment and Sustainable Communities (IEESC), university of Regina used a dynamical approach to downscale outputs of GCMs for Ontario (CCDP 2017). A RCM named regional climate model system (RegCM) with a spatial resolution of 25 km was used. On the other hand, the Laboratory of Mathematical and Parallel Systems (LAMPS), York university used the statistical downscaling approach to generate climate data of 10 km resolutions for Ontario (OCCP 2017). Davies (2011) used a dynamical-statistical approach to generate more localized (5 km) predictions for the England. The author reported that the quality of the localized climate data is largely governed by the performance of the weather generators (WGs), and special care should be taken when selecting a RCM and WG.

2.5 Saturated and Unsaturated Soil Mechanics

For most soil mechanics applications soils are either considered fully saturated or completely dry. However, the voids within a soil can be filled with both the air and water, and the soil is called ‘unsaturated’ or ‘partially saturated’. Both the hydraulic and strength properties of the unsaturated soil vary with time, and involve complexities in quantifications. The following sections present an overview of saturated and unsaturated soil mechanics along with commonly used numerical modeling techniques.

2.5.1 Saturated soils

The voids in a saturated soil are filled with water. Therefore, the water flow through saturated soils depends upon the hydraulic conductivity, and hydraulic gradient. The hydraulic conductivity of a saturated soil is considered as constant, and the flow is only controlled by the hydraulic gradient. The water flow rate within a saturated soil can be calculated using Darcy’s law which can be written as follows:

$$Q = K_{sat}\ i\ A \tag{2.12}$$

where:

$Q =$ volume of water flowing per unit time, m^3/s,

$K_{sat} =$ Saturated hydraulic conductivity, m/s,

$i =$ hydraulic gradient, and

$A =$ cross-sectional area, m^2.

The mechanical behavior of the saturated soil can be described by the effective stress formula of Terzagih. The effective stress within a saturated soil decreases with the increase in pore water pressure and consequently the soil shear strength decreases. The shear strength of saturated soils can be quantified by the Mohr-Coulomb failure criterion which can written as follows:

$$\tau_f = c' + (\sigma - u_w)_f \tan\phi' \tag{2.13}$$

where:

$\tau_f =$ shear stress at failure (kPa),

$c' =$ effective cohesion (kPa),

$(\sigma - u_w)_f =$ effective stress at failure (kPa),

$\sigma_{ff} =$ total normal stress on the failure plane at failure (kPa),

$u_{wf} =$ pore-water pressure at failure (kPa), and

$\phi' =$ effective angle of internal friction (degree).

On a plot of shear stress versus effective normal stress the failure envelope is defined by a straight line with a slope equal to the effective angle of internal friction and an intercept on the shear stress axis at effective cohesion.

2.5.2 Unsaturated soils

Unsaturated soils are considered a three-phase medium containing soil as the solid, water as the liquid, and air as the gas. The ratio of water to the total volume of voids is the degree of saturation. The presence of air and water in the unsaturated soils generates negative pore pressure which is known as matric suction. Total suction within a unsaturated soil is made up of a combination of matric suction and osmotic suction (Fredlund et al. 2012). The matric suction within unsaturated soil is the difference between the pore air pressure and the pore water pressure, and can be expressed as a function of volumetric water content and/or degree of saturation. The relationship between matric suction and volumetric water content is called soil-water characteristic curve (SWCC). Figure 2.3 shows typical SWCCs for soils ranging from sand to clay. When soil is in saturation state, the matric suction is zero, at this time the water content is saturated water content, θ_s. If minimal suction is applied, still no water will be drained.

With the increase of suction to a critical value, water starts draining. This critical suction is called air entry value (AEV) or bubbling pressure. After exceeding AEV, with the increase in suction soil continuously drains water until it reaches to the residual water content, θ_r. In the residual condition, the water is tightly held to the soil and flow only occurs as vapor flow.

The grain size of soil has potential effects on SWCCs. As shown in Figure 2.3 the θ_s, and AEV are the highest for the fine grain clay, and then decrease for the silt and sand. It also can be seen in Figure 2.3 that the shape of the intermediate draining portion of the SWCCs also varies with the soil types. The fine grain clay shows a gradual draining curve, while the slope of the draining portion of the SWCCs increases for the silt and sand. The θ_r also is the highest for the clay, and decreases for the silt and sand (Figure 2.3).

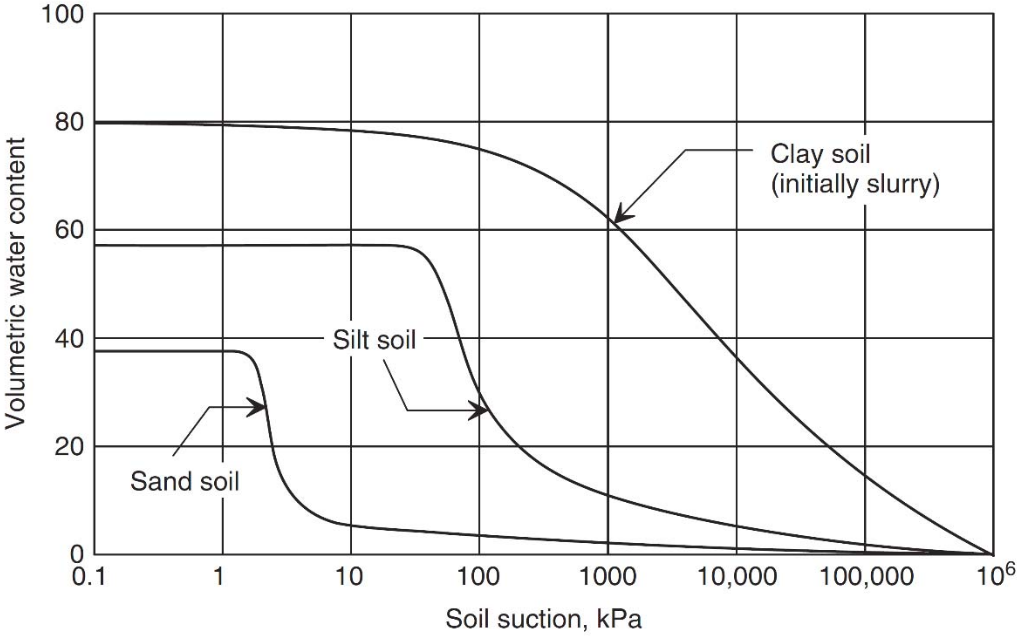

Figure 2.3 Comparative typical SWCCs for sand, silt, and clay soils (Fredlund et al. 2012)

The SWCC is the primary unsaturated soil information as many behavior and properties of soils can be derived from it. For SWCC to be used in the constitutive models of unsaturated soil, it has been described using mathematical relationships. Many mathematical models have been proposed that describe the SWCC with varying degrees of success. Two widely used

SWCC models are the van Genuchten (1980) model, and Fredlund and Xing (1994) model. These two models are shown in the equations (2.14 and 2.15 respectively.

$$\Theta = \left[\frac{1}{1+(a\psi)^{n_1}} \right]^{m_1} ; \; \Theta = \frac{\theta - \theta_r}{\theta_s - \theta_r} ; \; m_1 = 1 - \frac{1}{n_1} \tag{2.14}$$

where:

$\theta =$ volumetric water content (m^3/m^3),

$\theta_s =$ saturated volumetric water content (m^3/m^3),

$\theta_r =$ residual volumetric water content (m^3/m^3),

$\psi =$ suction (m),

$a =$ fitting parameter related with inverse of air entry value (1/m), and

$m_1, n_1 =$ model's fitting parameters.

$$\theta = C \frac{\theta_s}{\left[\ln\left(e + \left(\frac{\psi}{\alpha} \right)^{n_2} \right) \right]^{m_2}} ; \; C = 1 - \frac{\ln\left(1 + \frac{\psi}{\psi_r} \right)}{\ln\left[1 + \left(\frac{10^6}{\psi_r} \right) \right]} \tag{2.15}$$

where:

$C =$ correction factor which is a function of suction corresponding to θ_r,

$e =$ natural logarithm base,

$\alpha =$ fitting parameter related with air entry value (m),

$m_2, n_2 =$ model's fitting parameters, and

$\psi_r =$ Suction corresponding to residual water content (m).

The hydraulic conductivity of unsaturated soils is also a function of matric suction. The unsaturated hydraulic conductivity function (HCF) can be estimated from SWCC. van Genuchten (1980) used the statistical pore-size distribution model of Mualem (1976) to obtain a predictive equation for the unsaturated HCF in terms of soil water retention parameters. The expression of van Genuchten (1980) can be written as follows:

$$\frac{k_h}{k_{sat}} = \Theta^l \left[1 - \left(1 - \Theta^{\frac{1}{m_1}}\right)^{m_1}\right]^2 ; \; \Theta = \frac{\theta - \theta_r}{\theta_s - \theta_r} ; \; m_1 = 1 - \frac{1}{n_1} \qquad (2.16)$$

where:

$k_h =$ hydraulic conductivity (m/s),

$k_{sat} =$ saturated hydraulic conductivity (m/s),

$l =$ a constant set to 0.5, and

$n_1 =$ fitting parameter of SWCCs.

In unsaturated soils, the volumetric water content and hydraulic conductivity are function of matric suction. This dependency of hydraulic conductivity on matric suction has made the water flow process a function of matric suction as well. The water flow within unsaturated soil is modeled using the Richards equation (Richards 1931) which can be written for two dimensional water flow as follows:

$$\frac{\partial \theta}{\partial t} = \frac{\partial}{\partial x}\left[K(h)\frac{\partial h}{\partial x}\right] + \frac{\partial}{\partial z}\left[K(h)\left(\frac{\partial h}{\partial z} + 1\right)\right] - S_w \qquad (2.17)$$

where:

$\theta =$ volumetric water content (m^3/m^3),

$t =$ time (s),

$K(h) =$ unsaturated hydraulic conductivity (m/s),

$h =$ soil water matric head (m), and

$S_w =$ sink term that represents the volume of water removed per unit time from a unit volume of soil ($m^3m^3s^{-1}$),

The Richards equation (equation (2.17) is directly used by many investigators, and in some forms within many hydrological software codes to investigate water flow through unsaturated soils. However, the main drawbacks of this approach are that it is assumed that the soil is rigid and incompressible (Davies 2011).

The mechanical behavior of a soil can be described by the state of stress (Fredlund et al. 2012). The Terzaghi's principle of effective stress can be used to describe the stress state variable of saturated soil (Lu and Likos 2006, Fredlund et al. 2012). However, calculation of effective stress in unsaturated soils is more complex because of its three-phase nature. An overview of the historical development of effective stresses calculation in unsaturated soils has been presented by Lu and Likos (2006). The effective stress calculation method proposed by Bishop (1959) achieved widespread use (Davies 2011), it can be written as follows:

$$\sigma' = (\sigma - u_a) + \chi(u_a - u_w) \tag{2.18}$$

where:

$\sigma' =$ effective stress (kPa),

$\sigma =$ total stress (kPa),

$u_a =$ pore-air pressure (kPa),

$u_w =$ pore-water pressure (kPa), and

$\chi =$ empirical parameter that can be expressed as a function of the degree of saturation.

The Bishop's effective stress equation of the unsaturated soils considers that the soil suction or negative water pressure has the potential of adding strength to a soil. In contrast, the positive pore water pressures decrease the effective stress and thereby decrease the strength. Therefore, the shear strength of the unsaturated soils is also a function of matric suction, and can be quantified using the soil water characteristic curves and the effective shear strength parameters. Considerable research has been conducted to estimate shear strength of unsaturated soils using SWCCs (e.g., Fredlund et al. 1996, Vanapalli et al. 1996, Lu et al. 2010). The most frequently used method is by Vanapalli et al. (1996) which can be written as follows:

$$s = c' + (\sigma - u_a)\tan\phi' + (u_a - u_w)\left[\left(\frac{\theta - \theta_r}{\theta_s - \theta_r}\right)\tan\phi'\right] \qquad (2.19)$$

where:

$s =$ shear strength of soil (kPa).

The above equation (2.19 can be used to estimate unsaturated shear strength of soils using SWCCs and effective shear strength parameters c' and ϕ'.

2.6 Review of the Hydrological and Geotechnical Modeling Software

Predicting climate change impacts on slope stability contains three different steps: prediction of small scale future climate data, estimation of pore-water pressure (PWP) within slopes, and estimation of factor of safety of slopes for the predicted PWP. These three steps contain many complexities, and several simplifications have been applied to link them together (Buma 2000). Buma and Dehn (1998) proposed a method of predicting climate change impact on slope stability by linking slope models to climate scenarios obtained through downscaling of GCMs.

A similar method was used by Dehn and Buma (1999) to assess the future activity of landslides in SE France. The future climate data was generated by downscaling the outputs of three GCMs. The downscaled climate data was used as an input to a simple slope stability model. The probability of landslide occurrence was then estimated by comparing predicted groundwater level with a critical level. The critical groundwater level was determined by statistical analysis of the historical annual maximum groundwater levels. Dixon and Brook (2007) studied the impact of climate change on landslides at Mam Tor, Derbyshire, UK. A rainfall threshold of landslide triggering was determined by statistical modeling of historical precipitation data. The future predicted precipitation was then compared with the threshold value to estimate climate change impacts on future landslides.

Collison et al. (2000) studied climate change impacts on future landslides for south-east England. The climate change data was generated by downscaling the outputs of GCMs. The downscaled climate data was then linked to a simplified hydrological model to estimate the mean water table depth. The calculated mean water table was then distributed over a 4-km section using digital terrain models (DTMs). The stability of slopes was finally estimated from the water table height and DTMs using an infinite slope model.

Chiang and Chang (2011) studied the impacts of climate change on typhoon-triggered landslides in Taiwan. A four steps methodology containing selecting a GCM, correcting GCM data, downscaling of temporal resolution, and calculating the factor of safety was applied. The slope stability model used considers daily rainfall and upslope contributing drainage area along with soil properties to calculate stability of slopes (Montgomery and Dietrich 1994).

Rouainia et al. (2009) used a coupled hydrological (SHETRAN) and geotechnical (FLAC) model to study climate change impacts on a cutting on the Newbury bypass in southern England. Downscaled climate data was used as an input in the hydrological model to estimate

PWP within the slope. The factor of safety of the slope was then calculated using the estimated PWP. The authors reported that the coupled hydrological and geotechnical model was capable to predict PWP changes effectively, and can be used in climate change impact assessment studies. Davies (2011) also used the same combination of hydrological and geotechnical model and reported similar findings. However, the transfer of PWP from the hydrological model to geotechnical model was identified as the main challenge for the physically based slope stability modeling (Davies 2011).

2.6.1 Hydrological models

The application of physically based hydrological and geotechnical models has become popular in climate change impact on slope stability studies, and has been applied in many locations around the world (e.g., Davies 2011, Robinson et al. 2017). Hydrological models in the context of slope stability use climate data, and soil hydraulic properties as input, and calculate PWP within slopes. Pore pressures distribution is the primary factor affecting slope stability and needs to be quantified accurately. Therefore, a hydrological model should have the capabilities to calculate the pore pressure distributions accurately. Davies (2011) suggested that a hydrological model at least should satisfy following requirements to be effective in climate change impact assessment studies:

- Two or three dimensional model
- Capable of simulating climate data of higher resolutions (i.e., hourly)
- Should be able to calculate the rate of infiltration, evaporation, and runoff
- Should be able to simulates variably saturated flow
- Vegetation should be simulated at ground surface
- Preferentially capable of simulating hysteresis within the SWCC and HCF

Three commonly used physically based hydrological modeling programs that satisfy most of these requirements are: HYDRUS (PC-Progress), VADOSE/W (Geo-Slope) and SHETRAN (Newcastle University). These three models each have some distinct advantages over others when modelling variably saturated slopes. The general features of the programs are shown in Table 2.2.

Table 2.2 General characteristics of the selected hydrological models (Davies 2011)

	HYDRUS	VADOSE/W	SHETRAN
Code	Finite element	Finite element	Finite Difference
1D/2D/3D	1D, 2D and 3D	2D	3D
One phase/two phase	1	1	1
Unsaturated flow equation	Modified form of the Richards equation	Richards equation with modifications for vapour flow by Wilson (1990) and Milly (1982)	Richards equation
Soil hydraulic model	Brooks and Corey, 1964; van Genuchten, 1980; modified van Genuchten, Kosugi, 1996;	Arya and Paris (1981); modified Kovacs; Fredlund and Xing (1994); van Genuchten, (1980)	Van Genuchtenen, 1980
Hysteresis	Yes	No	No
Evapotranspiration model	Yes (system dependent boundary condition, Neuman et al. 1974)	Yes (Penman-Wilson, 1990)	Yes (Penman-Monteith, 1965)
Root uptake model	Yes	Yes	Yes
Seasonal vegetation effects	Yes	Yes	Yes
Runoff	1D model assumes water can stand on surface, 2D and 3D models assume all water that does not infiltrate is reported as runoff	Water that does not infiltrate is accumulated at the ground surface or reported as runoff	Yes Modified St. Venant equation

The review of the commonly used hydrological models shows that each of the models has some distinct advantages over others. HYDRUS is the only program that considers the hysteretic behavior of SWCC and HCF; however, it uses a simplified calculation method for actual evapotranspiration and surface runoff. In contrast, VADOSE/W and SHETRAN do not consider hysteresis, but use physically based models to calculate actual evapotranspiration.

2.6.2 Geotechnical models

Geotechnical models take the pore pressure distributions from the hydrological models as input, and estimate the stability of slopes. One of the primary selection criteria of a geotechnical model in climate change impacts on slope stability studies is that it should be capable to consider the effects of changes in PWP calculated in hydrological model (Davies 2011). A significant number of commercial codes is available in the market. An overview of few of the commonly used geotechnical models is presented in the following sections.

HYDRUS has two add-on slope stability modules to calculate stability of embankments, dams, earth cuts and anchored structures (PC-Progress 2014). These slope modules are coupled with the hydrological model and provide an easy way to transfer pore water pressure. Moreover, these modules provide both the limit equilibrium and finite element method of slope stability analyses. However, the limit equilibrium module only considers the saturated effective strength parameters, and do not account the effect of additional strength from the suction component of unsaturated soil.

SLOPE/W is a limit equilibrium 2D slope stability modeling program which is developed by the Geo-Slope International Ltd. as a part of the Geo-Studio package (Geo-Slope International Ltd. 2014b). This program provides a wide range of modeling facilities including PWP and rapid drawdown. It supports a comprehensive list of material models including Mohr-Coulomb, undrained, high strength, impenetrable, bilinear, anisotropic strength, stress history and normalized soil engineering properties (SHANSEP), spatial Mohr-Coulomb and more. The prime advantage of SLOPE/W over others is that this program has inbuilt unsaturated shear strength models which allow the modeling of unsaturated soil. However, SLOPE/W does not have facility to model progressive failure of a slope due to successive shrink and swell cycles (Davies 2011).

PLAXIS is a powerful commercial finite element package available in both 2D and 3D formats. It provides a user friendly interface of analysis of deformation and stability in geotechnical engineering and rock mechanics (Brinkgreve and Vermeer 1998). This program contains advanced constitutive models which consider nonlinearity, time dependency, and anisotropic behavior of soils. Moreover, it is capable to model the progressive failure of slopes due to seasonal swell and shrink. However, PLAXIS does not have inbuilt unsaturated shear strength models to simulate unsaturated flows, but separate add-on module can be used to simulate unsaturated flows.

FLAC is a finite difference program, available in both 2D and 3D formats. This package is capable to model many complex geotechnical problems, such as staged analysis, large displacements and strains, non-linear material behavior, and unstable system (ITASCA Consulting Group, Inc. 2017). Like PLAXIS, FLAC also does not have inbuilt unsaturated constitutive soil models, but add-on module allows modeling of unsaturated flows (Davies 2011). The main advantage of this program is that it contains an inbuilt programming language called FISH, which allows user to write custom functions within the code.

Based on the review of few commonly used geotechnical models, following conclusions can be made. HYDRUS has both the limit equilibrium and finite element module, but the limit equilibrium module does not consider the suction strength of the unsaturated soils. The PLAXIS and FLAC codes contain advanced modeling techniques; however, these two codes require separate add-on modules to model the unsaturated soils. On the other hand, SLOPE/W has inbuilt unsaturated constitutive models, but unable to model progressive failure of a slope.

The technique of modeling climate change impacts on slopes has been evolved from simple statistical relationship to detailed physically based relationships. A significant number of physically based hydrological and geotechnical modeling programs have become commercially available. However, each of these models have a wide range of advantages over the others, and it is important for the users to make a suitable choose.

2.7 Studying the Effect of Climate Change on Slope Stability

Recent evidences and future predictions show that the future climate could show significant changes. It is now critical that engineers can assess how their infrastructure/designs will behave under a variety of future climate scenarios. The slope and embankment are highly climate dependent engineering infrastructure. It is important to ensure that the slope and embankment are safe against future climate change. In the last two decades the climate change impact assessment studies have started in the context of slope stability. Collison et al. (2000) conducted a regional study on climate change impacts on landslides for southeast England. Future climate change was predicted using a GCM, HADCM2 developed by UK Hadley center. The GCM outputs were downscaled using the downscaling technique of Buma and Dehn (1998). The downscaled climate data were used in a one dimensional hydrological model to estimate the location of groundwater table. The groundwater table prediction from the 1D model was then distributed over the whole region using a DTM. Finally, the slope stability assessments were conducted using the groundwater depth, slope geometry, and soil properties. Collison et al. (2000) concluded that the effects of increasing precipitation could be counterbalanced by increasing evaporation. Some of the limitations of their study are use of a simplified method of future climate data generation, and prediction of regional groundwater table using a one dimensional hydrological model.

Later in 2004, Schmidt and Dikau studied the influence of historical climate variability on the stability of three hillslopes in Bonn, Germany. The historical climate was classified into three clusters: high precipitation and low temperature (before 1750 AD), low precipitation and intermediate temperature (1750-1850 AD), and low precipitation and high temperature (after 1850 AD). A physically based distributed hydrological model was used to calculate lateral and vertical saturated flow, and groundwater depth. The hydrological model was coupled with a slope model, and calculated factor of safety of slopes using planar slope model (Barnes 2010). Schmidt and Dikau (2004) found that the precipitation pattern is the prime factor affecting the stability of the slopes. The authors also reported that the critical condition occurred for the climate scenario that contained the highest number of extreme precipitation events. Some of the shortcomings of the study are neglecting the Vadose zone, and use of a simplified method of climate classification.

A detailed study on climate change impact on a railway embankment at Newbury, southern England was conducted by Davies (2011) for his doctoral research at Newcastle University in the UK. Future climate data of 5 m grid was generated from the outputs of GCMs using a weather generator, EARWIG. A coupled hydrological and geotechnical model was used to estimate the stability of embankments for the historical and future climatic conditions. Davies (2011) concluded that the future climate with high temperature and short but intense precipitation improves stability of embankments. One of the drawback of the study is only the worst case of high emissions for 2080 scenario was considered for future climate, and left the effects of other scenarios unknown. Recently, Vardon (2015) reviewed the potential of climate change on geotechnical infrastructures from the European climatic perspective, and recommended to consider climate change effects on geotechnical designs.

The knowledge on climate change impacts on slopes and embankments in North America is still limited. It has been predicted that a significant change in future climate variables could be observed in some places in North America (IPCC 2013). This might make many currently stable slopes and embankments vulnerable to instabilities. Therefore, it is imperative to understand the impacts of future climate change on the stability of embankments and slopes. In a very recent time, Robinson et al. (2017) conducted a study on the impact of future extreme precipitation events on landslides in an area near Seattle, Washington. The design extreme climate events were constructed using intensity duration frequency (IDF) curves. A duration of 7-day, and frequency of 50-year was selected for both the baseline and future climates. A coupled stress – unsaturated flow finite element model was used to estimate the stability of a hypothetical natural slope. The results of the study show that the future IDF curves have detrimental effects on slopes, and use of historical IDF curves could lead to underestimation. The authors suggested that the engineered slopes also could show similar behavior. One of the limitation of the study is use of a single intensity and duration for the design climate, which leaves the actual behavior of slopes unknown for other storms.

Studying climate change impact on slopes and embankments in Canada can be more challenging due to its wide range of geological, geomorphological, and climatological settings (Bo et al. 2008, Cloutier et al. 2016). In addition, the mode and type of slope failures also show large variation which has included more complexity (Hungr et al. 2014). The existence of perennially frozen ground (permafrost), glaciers in the mountain slopes, and marine clay deposits make the slopes more vulnerable to instabilities for climate change (Cloutier et al. 2016). The historical climate (1948-2014) shows an average increase of 1.6°C in annual mean temperature in most regions of Canada (Cloutier et al. 2016). This rising trend could continue over the next century, and the mean temperature could increase from 9°C to 15°C in eastern Canada (Colombo et al. 2007). This projected increase in temperature is higher in the winter seasons compared with the summers. Besides temperature, historical precipitation also shows a rising trend over period 1948-2012 (Natural Resources Canada 2014). It has been predicted that the future precipitation could follow this rising trend with higher magnitude in the winters and springs (Natural Resources Canada 2014). This increasing spring precipitation along with high antecedent moisture from the winter snow melt, could potentially increase the vulnerability of embankments and slopes to failures.

The potential threat of climate change on slopes and embankments in Canada is presented in previous studies (e.g., Bo 2008, Cloutier et al. 2016). However, the knowledge of quantifying the impact of future climate change is still limited. Natural slopes in Canada are identified as more vulnerable than the engineered embankments (Bo et al. 2008); however, failures of engineered slopes could cause high economic losses. For example, closer of a major transportation corridor due to failure of an embankment in a transportation network may cause a large socio-economic loss in terms of indirect costs. Therefore, it is important to ensure the safety of the existing and to be constructed embankments against the adverse effects of climate change. Quantification of the impacts of climate change on the stability of embankments could be used to modify existing design recommendations.

Chapter 3. Climate Data Compilation

3.1 Introduction

This chapter provides an overview and temporal trend for historical and future climate. The first part of this chapter presents an overview as well as trends of climate variables over past 30 years (1981-2010). In addition, the results from trend analyses of future climate based on predictions of three general circulation models (GCMs) are also presented. This chapter concludes with the construction of design climates (DCs) for the stability analysis of embankments.

3.2 Historical Climate

In climate change impact assessment studies, baseline climate (BC) is used as a datum to show probable changes in future climate variables. This BC is developed using historical climate records, which in Canada are made available by the department of Environment and Climate Change. Environment and Climate Change Canada (previously known as Environment Canada) measures climate variables all across the country, and provides open access to this data on their website (Environment Canada 2011a). All the major climate variables can be directly downloaded for any weather station across Canada. The solar radiation data can be obtained from a separate dataset named Canadian Weather Energy and Engineering Datasets (CWEEDS). This dataset contains station data of 21 climate variables across the Country from 1953 to 2005 (Environment Canada 2011b).

In this study, the BC consists of 30 years of climate record (1981-2010) for the city of Toronto, Ontario. The climate variables were collected from the weather station of Environment Canada at Pearson International Airport (WMO ID: 71624). A plot of the climate variables of interest is shown in Figure 3.1. It can be observed that all the climate variables are available for the period 1981 to 2010. The net radiation was estimated from the collected solar radiation data using a method proposed by Allen et al. (1998), and is shown in Figure 3.1e.

The 30 years of precipitation shows an average annual value of 786 mm. As shown in Figure 3.1a, 40 mm and higher amount of precipitation was recorded in total 28 days over the 30 year period. The highest recorded daily precipitation was 71.6 mm in 1986. In the same year, the 40 mm and higher amount of precipitation was recorded in 5 days which is the maximum number of 40 mm and higher events in a year. Figure 3.1b shows that the average positive and negative mean temperature for the 30 years period are 12.8, and -5.9°C respectively. The historical highest and lowest mean temperature of 31.5, and -24.7°C were recorded in the year 2006 and 1993 respectively. The mean relative humidity showed a daily average value of 72% over the 30 years from 1981 to 2010 (Figure 3.1c). It can be seen in Figure 3.1c that the relative humidity is usually lower in the summer when the mean temperature is higher. The lowest mean relative humidity of 28% was recorded in the summer of 2009, while the highest value of 100% was observed in the winter of 1983. The wind speed followed the similar trend of mean relative humidity. It can be observed in Figure 3.1d that the daily mean wind speed is usually higher in the winter months. The average wind speed for 30 years climate is 10 km/hr., while the highest and lowest observed values are 37 and 0.5 km/hr. respectively. The net radiation data followed the temperature trend, and the observed average positive and negative values are 8, and -2 MJ/m^2/day respectively. The highest and lowest recorded NR values were 20 and -6 MJ/m^2/day respectively. Therefore, based on the 30 years of historical data it can be concluded that Toronto climate contains warmer summer with lower humidity and wind speed, and colder winter with higher humidity and wind speed.

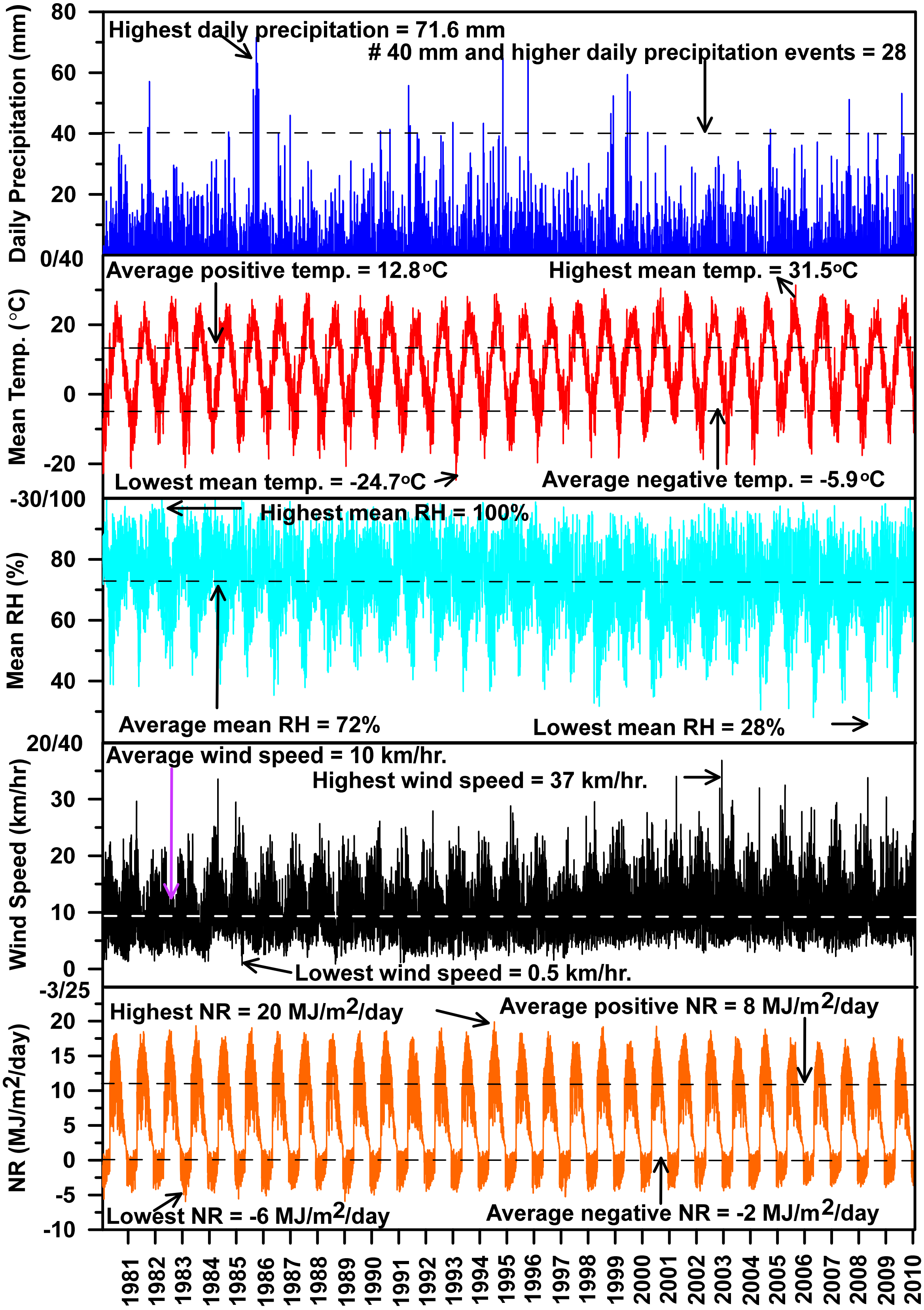

Figure 3.1 Historical climate data for Toronto (Environment Canada 2011a, 2011b)

3.2.1 Potential evaporation calculation

The potential evaporation (*PE*) is required to estimate the actual evaporation (*AE*) from the ground surface, and transpiration from the plants. It is also required for water balance studies and climate classification. The *PE* is usually estimated from various climate variables. The commonly required climate variables are temperature, relative humidity, wind speed, and net radiation, details of which have been provided previously in Figure 3.1. To select an appropriate method for *PE* estimation in local climatic conditions in Toronto, potential evaporation calculated using the Pereira and Pruitt (2004) method was compared with one calculated using the Penman (1948) method. A plot showing comparison of 26 years of cumulative potential evaporation for Toronto calculated using the Pereira and Pruitt (2004), and Penman (1948) methods is shown in Figure 3.2. It can be observed that the Pereira and Pruitt (2004) method underestimates the potential evaporation; however, the 26 years of cumulative error is only 5.4%. This underestimation could occur due to the inapplicability of this method in negative temperature. For further investigation, a comparison in monthly average *PE* was conducted which is shown in Figure 3.3. It can be seen that the Pereira and Pruitt (2004) method underestimates *PE* in the winter months, while it shows slight overestimation during summer. Overall, this method shows a satisfactory performance for the climate of Toronto. The main advantage of this method is that it only requires daily minimum, mean, and maximum temperature data. Because the historical as well as predicted future climate data for Toronto does not have all the required variables for Penman (1948) method, the Pereira and Pruitt (2004) was selected to calculate *PE* in this research.

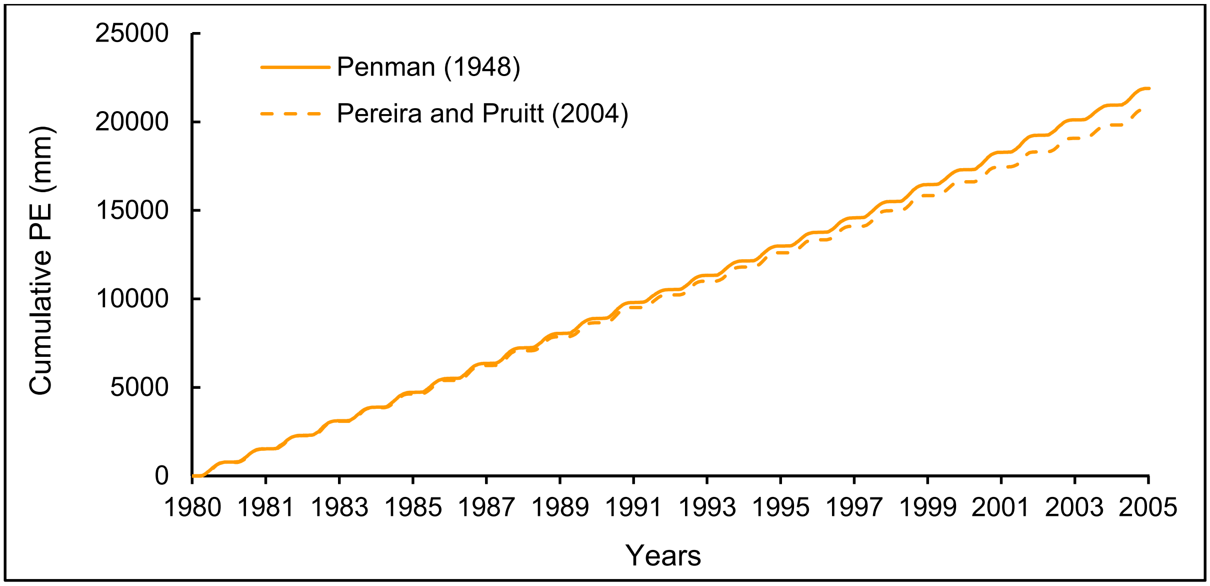

Figure 3.2 Comparison of cumulative PE calculated using Penman (1948) and Pereira and Pruitt (2004) methods

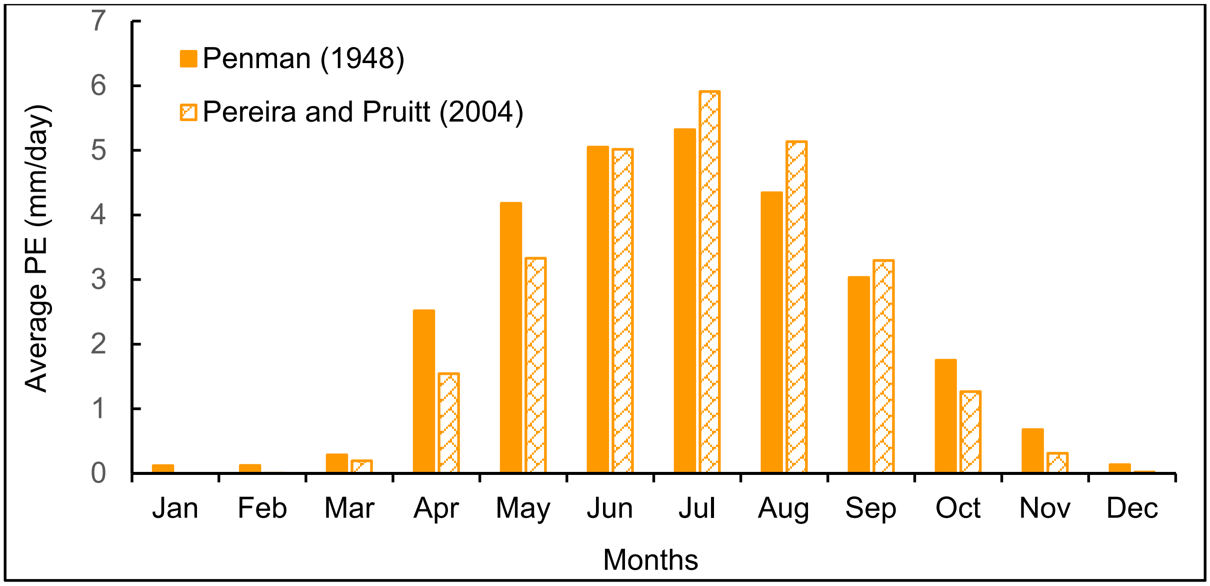

Figure 3.3 Comparison of monthly average PE calculated from Penman (1948) and Pereira and Pruitt (2004) methods

3.2.2 Climate classification

In geotechnical and geoenvironmental analyses and designs involving water balance at the ground surface, climate classification is frequently used. A commonly used climate classification method makes use of annual moisture index (I_m), which is estimated as a ratio of annual *P* and *PE* (Thornthwaite and Hare 1955). An I_m value of zero signifies that the annual *P* and *PE* are equal, and water balance condition at the ground surface is neutral. While the +100 and -100 I_m values indicate the wettest and driest possible conditions respectively.

The historical 30 years of I_m values for Toronto were calculated, and the results are plotted in Figure 3.4. On average, the climate for Toronto can be classified as being dry subhumid with an average I_m of -1.53. For the 8 of the 30 years considered, the climate classifies as "moist humid" and for 4 of the years, the climate classifies as "humid". The lowest I_m was computed for the year 2007 which falls within the "semi arid" range. The standard deviation of the I_m at this site was computed to be -17.81. The mean plus one standard deviation gives a moisture index of 16.25 (dry subhumid) while the mean minus one standard deviation gives -19.34 (moist humid).

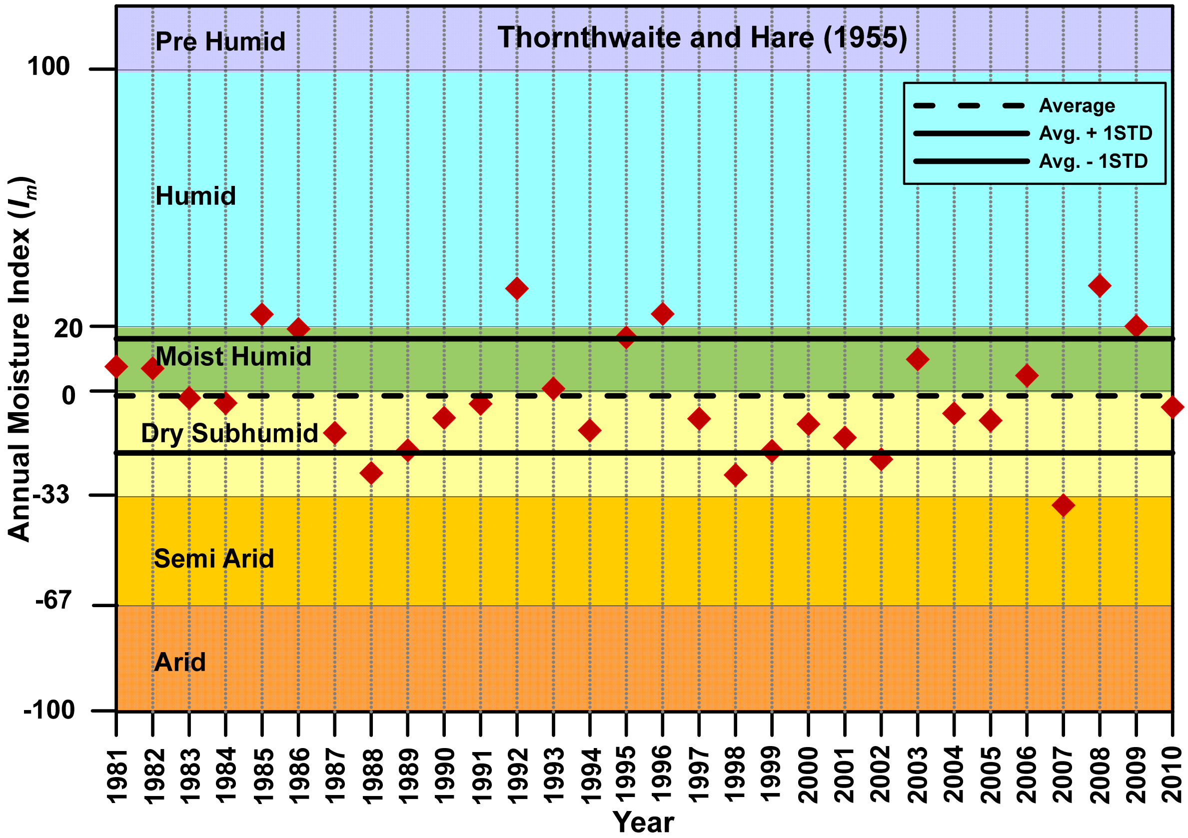

Figure 3.4 The I_m values for the baseline climate

The 30 years of moisture indices show that there are considerable differences in the ground surface water balance conditions from one year to another and therefore, it is important to investigate the details water balance by doing numerical simulations that embrace many years of weather records. As such, the 30 years of historical climate data for the period 1981 to 2010 was selected to formulate the upper boundary of the soil atmospheric model for the baseline period. It can be identified in Figure 3.4 that the year 2007, 1983, and 2008 as the dry, average, and wet year among the 30 years of BC.

3.2.3 Seasonal considerations

The partitioning of the annual climate could be meaningful if a considerable difference in the seasonal water movement exist (Fredlund et al. 2012). Toronto climate contains a warmer summer, and colder winter for several months when both the atmosphere and ground could remain frozen for longer time. Therefore, partitioning of the climate of Toronto into active and inactive periods simplifies the estimation of water balance. In the active period, the ground condition remains thawed, and water can enter the ground surface and flow. In the inactive period, both the atmosphere and ground are frozen. The precipitation accumulates at the ground surface in the form of the snow. It can also be assumed that in the inactive period little to no water enters the ground, and there is no flow in the upper soil layers. The inactive period starts with the date of freeze and ends with the date of thaw. The freezing and thawing dates can be found by analyzing the air temperature data.

The 30 years of mean air temperature data was analyzed to estimate freezing and thawing dates which are shown in Figure 3.5a and b respectively. It can be seen in Figure 3.5a that the freezing dates vary. However, majority of the dates are within the last week of November to first week of December. As such, an average freezing date of December 1 was selected. Thawing dates also show variation. The average of 30 years of thawing dates was found to be

April 6. Focusing on more recent years only (after 2000), the thawing dates are bound within the second week of April. As such, an average thawing date of April 1 was selected. The water year itself is then defined as the period from December 1 to November 30. In the water year the inactive season is from start of December to the end of March, and active season starts from April and ends in November. A portion of the active season is the growing season when the conditions for the vegetation to grow are favorable. For Toronto, it was found in the literature that the May to October is usually considered as growing season (Government of Canada 2013). A schematic plot showing the active, inactive, and growing seasons for Toronto is shown in Figure 3.6.

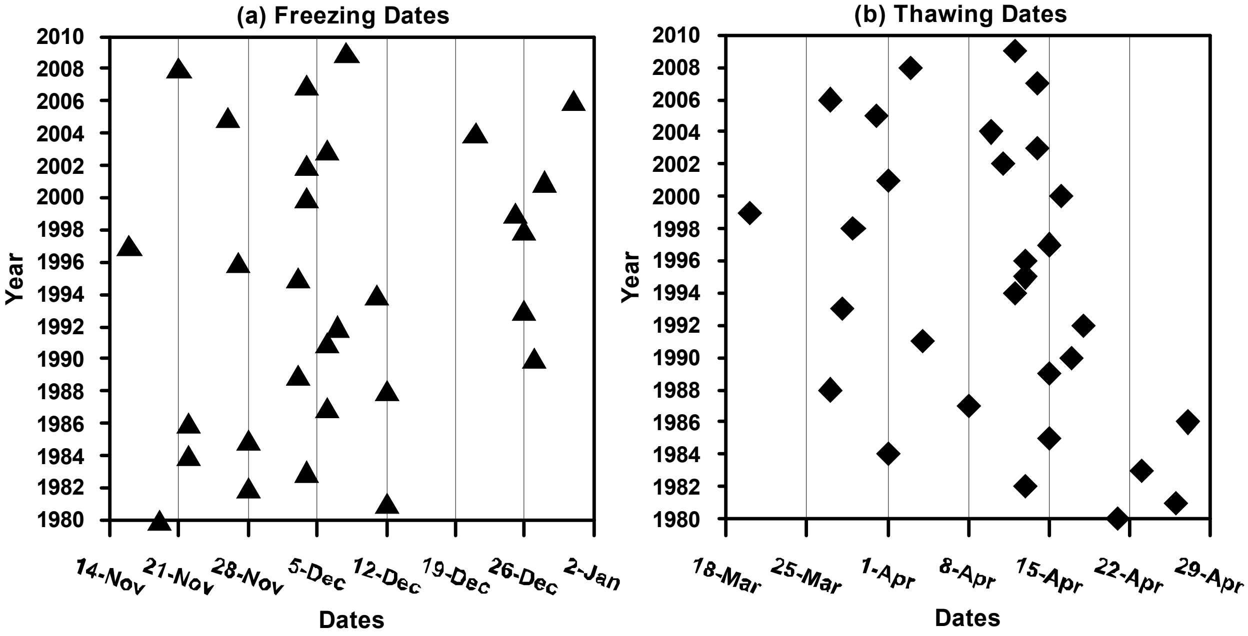

Figure 3.5 (a) Freezing, and (b) Thawing dates for past 30 years Toronto climate

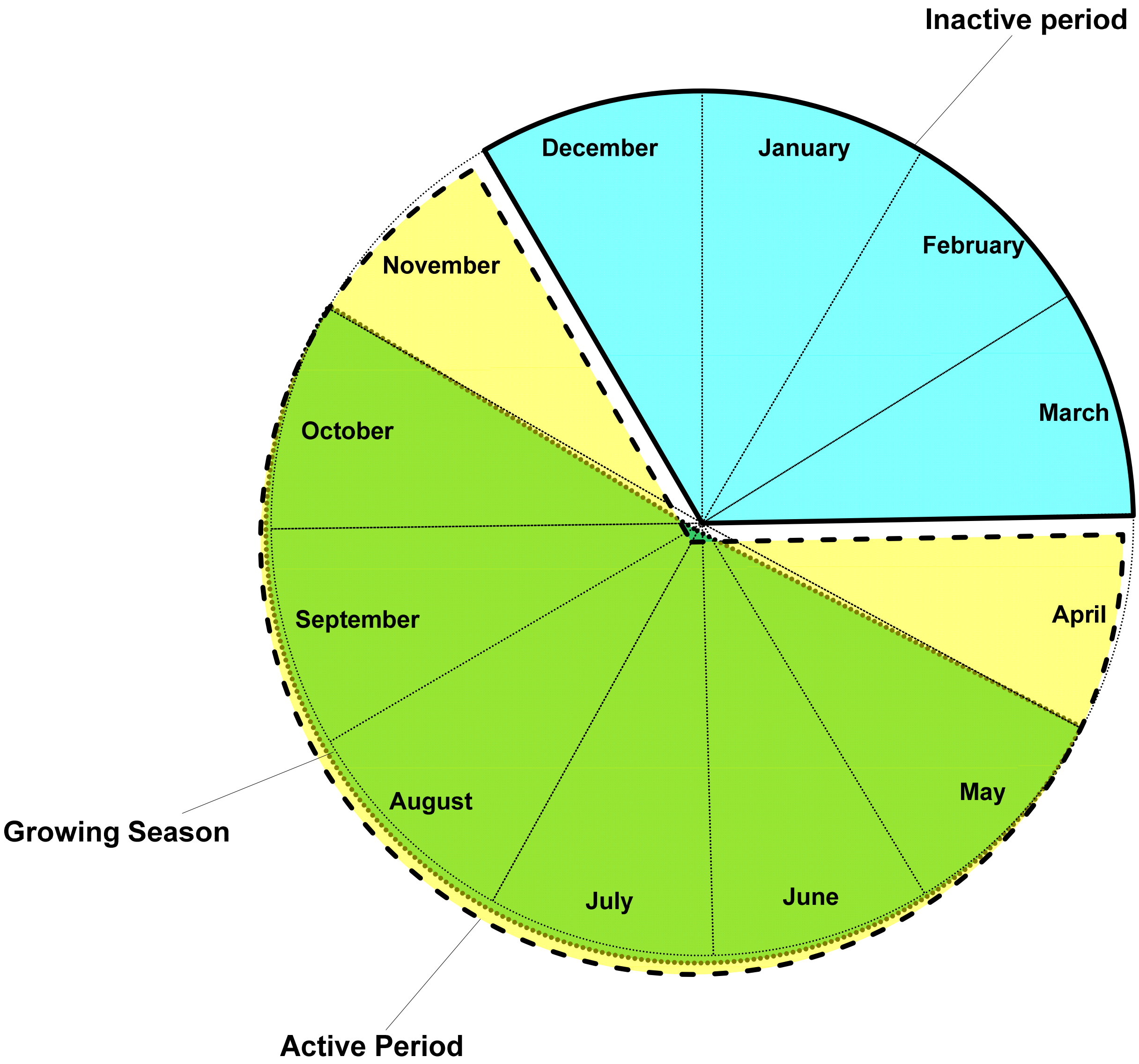

Figure 3.6 Partitioning of yearly climate of city of Toronto

Based on the partitioning of each year, the *P* and *PE* were calculated separately for the inactive and active periods. The results are presented in Figure 3.7. It can be observed that the average cumulative precipitation for 30 years during the inactive periods is 207 mm. The average total precipitation during active periods is 579 mm, giving rise to a total precipitation of 787 mm for the water year. It can be noticed that the average total precipitation for active periods of 8 months is much higher than the twice of amount of 4 months of inactive period. Therefore, it seems that, in average, the active periods experience more precipitation than inactive periods.

The average cumulative *PE* during the active periods is 797 mm, which is higher than the average precipitation of water year.

The seasonal consideration was employed to understand the water movement through the ground surface in the active and inactive seasons. Since the water movement through the ground surface in the inactive period is almost negligible, it could be advantageous to ignore the inactive period from the numerical simulations to cut unnecessary complexities and higher computation time. This approach has been used by others, e.g. Fredlund et al (2012) and Bashir et al. (2015), where only the active period was simulated to investigate water balance at the ground surface. For Toronto, the active period climate contains 244 days (April to November).

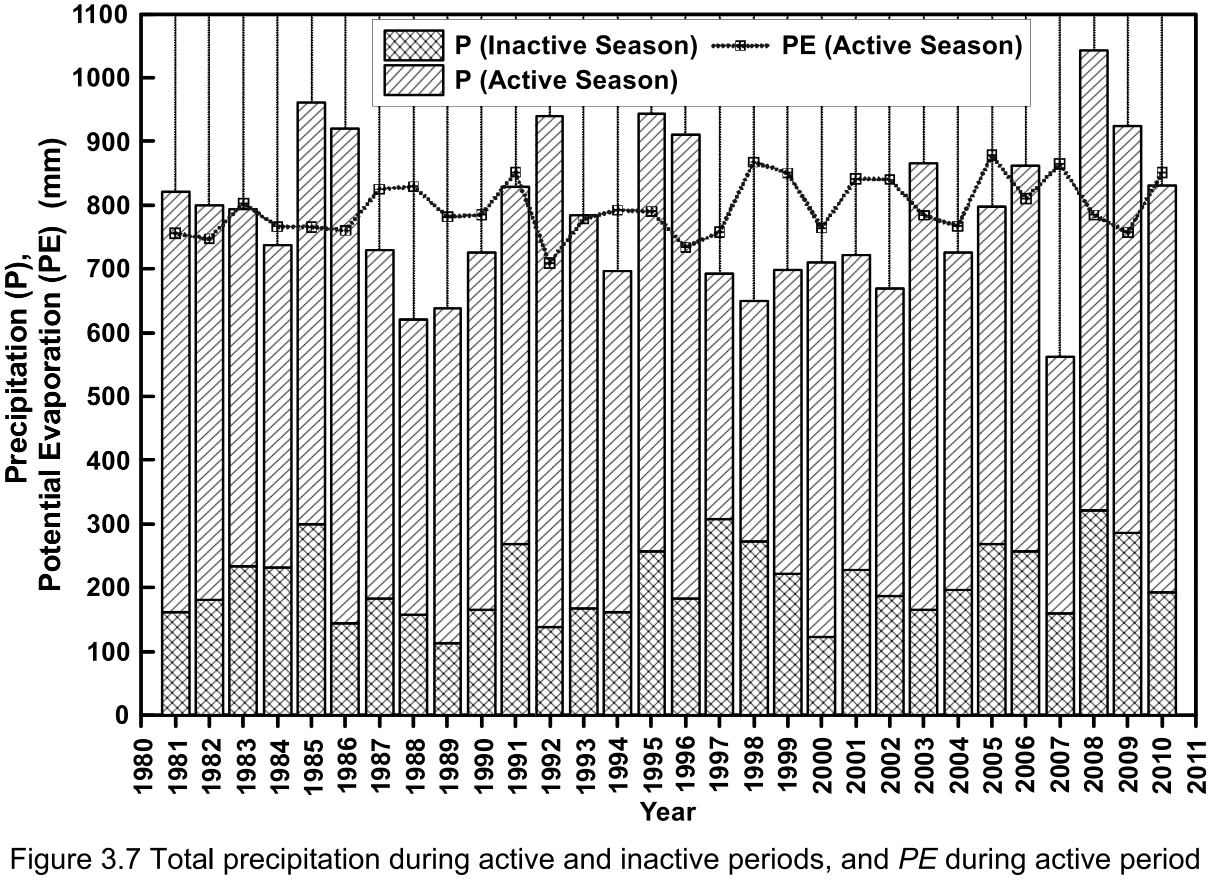

Figure 3.7 Total precipitation during active and inactive periods, and *PE* during active period

3.3 Future Climate

The future climate (FC) data for Toronto was selected from published sources in public domain. These sources are Ontario Climate Change Data Portal (CCDP), published by the Institute of Energy, Environment and Sustainable Communities (IEESC), university of Regina, and the Ontario Climate Change Projections (OCCP), published by the Laboratory of Mathematical Parallel System (LAMPS), York University.

3.3.1 Ontario Climate Change Data Portal (CCDP)

The IEESC has published FC data for ten climate variables in a grid size of 25×25 km (CCDP 2017). The climate data is available for five GCMs namely: CanESM2, HadGEM2-ES, GFDL-ESM2M, IPSL-CM5A-LA, and MPI-ESM-MR. Each of this GCM was run with the greenhouse gas concentration trajectory, representative concentration pathway (RCP) 8.5. A RCM named RegCM was used to downscale the climate projections under RCP8.5, and boundary conditions from the above mentioned five GCMs.

The precipitation, temperature, and wind speed data can be directly downloaded from the web portal (*www.ontarioccdp.ca*). The relative humidity needs to estimate from the published specific humidity and surface air pressure data. The net radiation also needs to estimate from the published cloud fraction, and surface shortwave and longwave fluxes. As a first step, the quality of the predicted FC data was assessed. To do so, the back predicted (1986-2005) precipitation and temperature data were collected from a nearest grid in Toronto, and compared with climate normals of Environment Canada. Figure 3.8 and 3.9 show a comparison between monthly climate normals (1981-2010) (Environment Canada 2011c) and predictions made using the GCM, CanESM2 for precipitation and mean temperature. It can be seen that the predicted data fails to accurately predict either the precipitation trend or quantity. A similar observation can be made for temperature data in Figure 3.9. Similar results are observed for predictions from other GCMs, and therefore, the climate data of CCDP was not used in this study.

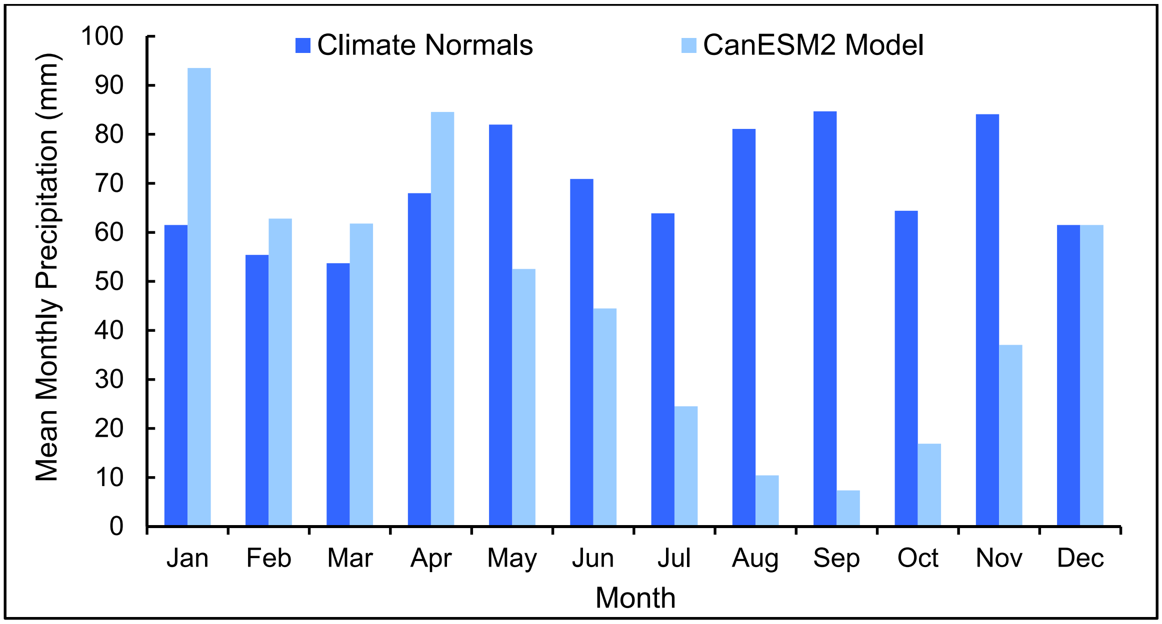

Figure 3.8 Comparison between climate normals and CCDP predicted precipitation data

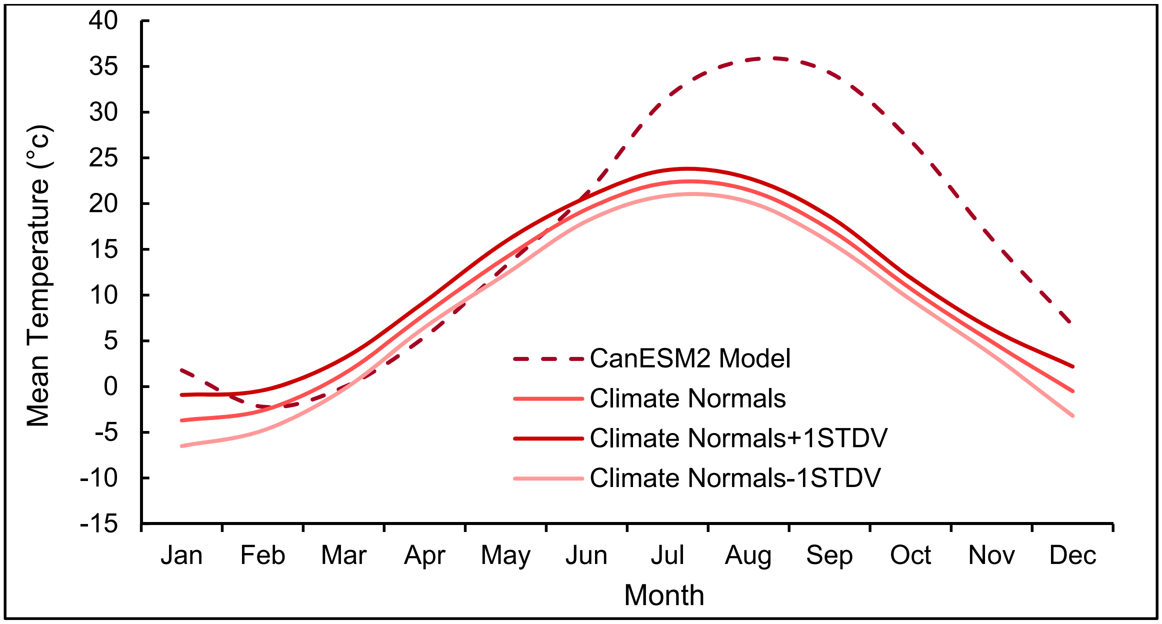

Figure 3.9 Comparison between climate normals and CCDP predicted temperature data

3.3.2 Ontario Climate Change Projections (OCCP)

The second future climate data source was OCCP, housed at LAMPS, York University. This dataset contains four climate variables namely: precipitation, Max., Avg., and Min. temperatures in 10×10 km grid resolution for 33 GCMs, and four RCPs (i.e., 2.6, 4.5, 6.0, and 8.5). This data covers the period from 1981-2100 (OCCP 2017), and can be freely downloaded from the OCCP webpage (*www.occp.lamps.yorku.ca*).

To check the performance of the predicted climate data, the back predicted (1981-2005) precipitation and mean temperature data from the GCM, CCSM4 were downloaded and compared with the climate normals of Environment Canada for the same period. Figure 3.10 and 3.11 show the plots for precipitation and temperature respectively. It can be observed that both the precipitation and temperature data show a good agreement with the climate normals. The better performance of this data source is partially due to use of a statistical downscaling method, which applies bias-correction over the predicted climate with respect to the measured local climate data (Deng 2016a).

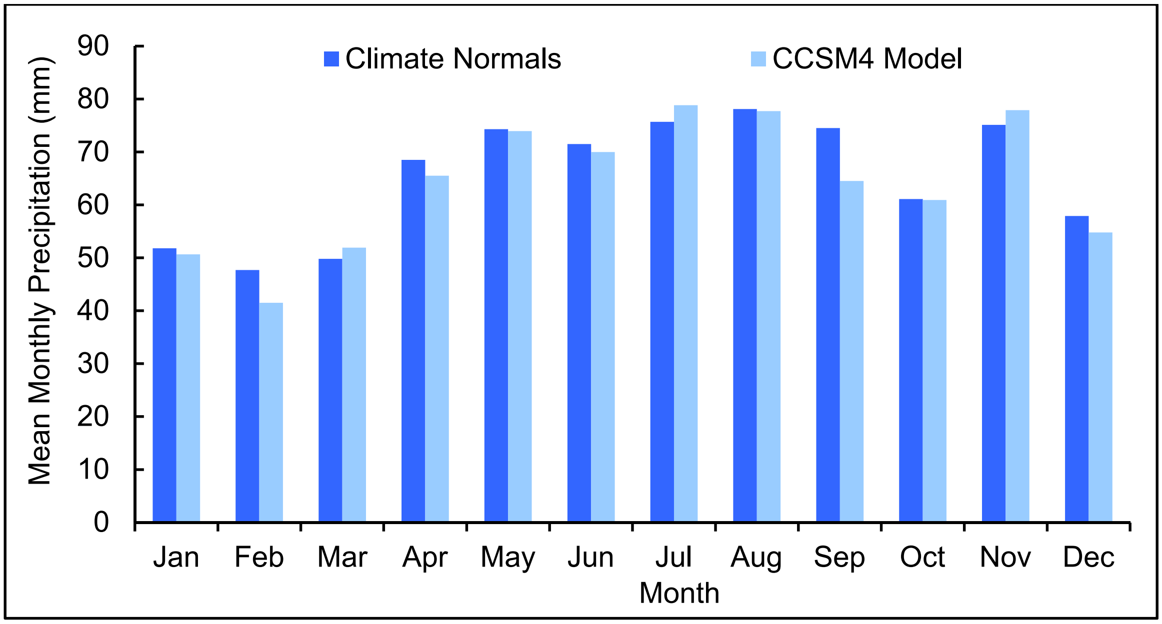

Figure 3.10 Comparison between climate normals and OCCP predicted precipitation data

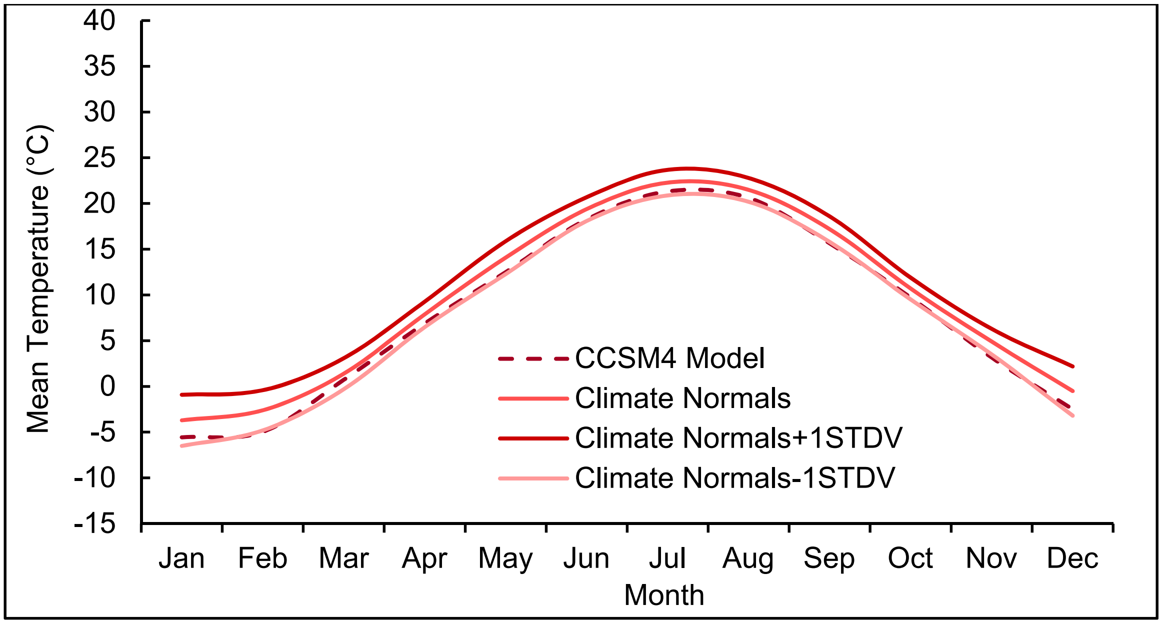

Figure 3.11 Comparison between climate normals and CCDP predicted temperature data

3.3.3 Selected Future Climate Datasets

The predicted climate data from OCCP database developed by LAMPS showed satisfactory performance when compared to historical climate, and was therefore selected for this research. LAMPS has analyzed the performances of each of the 33 general circulation models, and found that the CCSM4, GFDL-ESM2M, and NorESM1-M models show better performances for Toronto over others (Deng 2016b). The back predicted precipitation and temperature data of these three models were collected and compared with climate normals of Environment Canada. It was observed that like CCSM4 model, the GFDL-ESM2M and NorESM1-M models also show good agreement with climate normals. Pertinent details of the selected three GCMs are shown in Table 3.1. It can be seen that the NorESM1-M model has all the seven components, whereas CCSM4 has five, and GFDL-ESM2M has six components respectively. Each of these models have enough maturity, necessary resolution, and the validation. Therefore, these three GCMs with four pathways (i.e., RCP2.6, RCP4.5, RCP6.0, and RCP8.5) were finally selected.

Table 3.1 Overview of selected general circulation models (Flato et al. 2013)

Model^1 Vintage^2	Institution, Country	Main Components	Atmosphere Resolution	Scenarios Acquired
CCSM4^1 2010^2	US National Centre for Atmospheric Research, USA	atmosphere, aerosol, land surface, ocean, sea ice	0.9° × 125°	RCP 2.6, 4.5, 6.0, 8.5
GFDL-ESM2M^1 2011^2	NOAA Geophysical Fluid Dynamics Laboratory, USA	atmosphere, aerosol, land surface, ocean, ocean biogeochemistry, sea ice	2.5° longitude, 2° latitude	RCP 2.6, 4.5, 6.0, 8.5
NorESM1-M^1 2012^2	Norwegian Climate Centre, Norway	atmosphere, aerosol, atmos. chemistry, land surface, ocean, ocean biogeochemistry, sea ice	1.9° latitude, 2.5° longitude	RCP 2.6, 4.5, 6.0, 8.5

In this study, the baseline and future climates were subdivided into thirty-year periods, and each of these thirty-year climates were designated as a climate ensemble. For example, the 30 years (1981-2010) of historical climate was designated as climate ensemble number 1. The Future 90 years (2011-2100) of climate data from the three GCMs with four RCPs forms total 36 climate ensembles, where each ensemble refers to a GCM, RCP and a 30-year time period. A flow chart showing the baseline and future climate ensembles is presented in Figure 3.12. The future climate ensembles were named according to the RCPs and GCMs. For example, the 90 years of future climate of RCP2.6 of the CCSM4, GFDL-ESM2M, and NorESM1-M GCMs form the climate ensemble numbers 2, 3, 4; 5, 6, 7; and 8, 9, 10 respectively. The future climates with other RCPs were named in the same way.

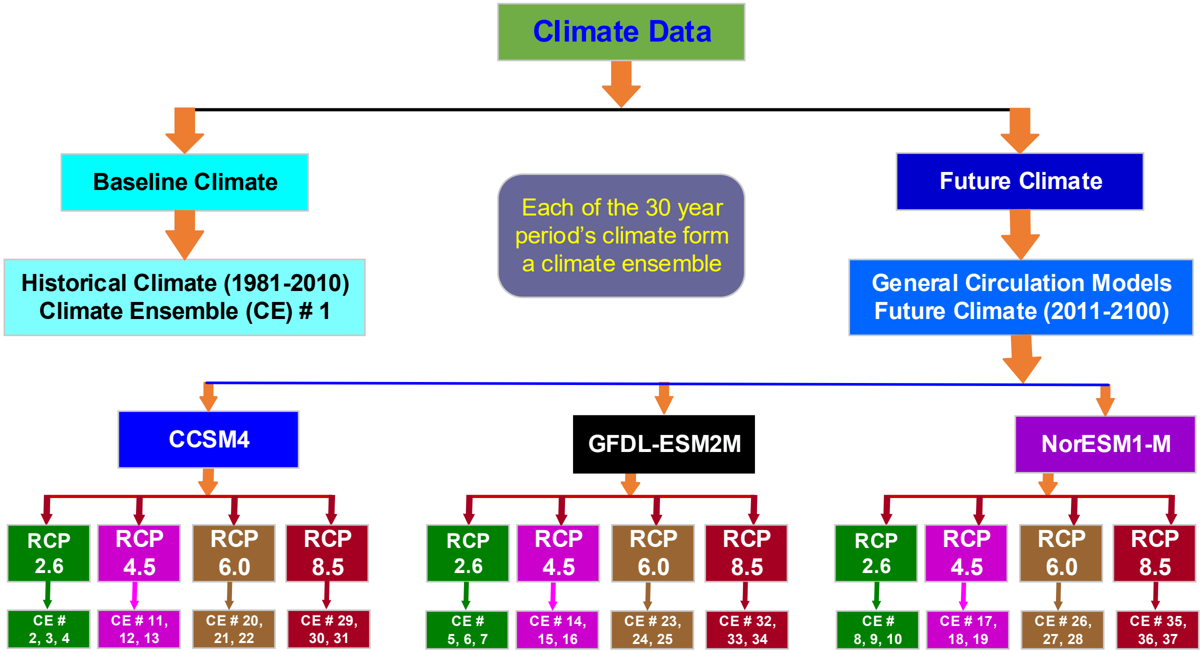

Figure 3.12 Flow chart showing baseline and future climate ensembles

3.3.4 Review of future climate predictions

The selected future climate dataset, OCCP only contains precipitation and temperature variables, and therefore, these two climate variables were selected for trend analysis. The *PE* was calculated from the temperature data using the Pereira and Pruitt (2004) method, and also was considered for trend analysis. The results for the first set of analyses are presented by comparing the box and whisker plots of total annual precipitation (Figure 3.13), mean annual temperature (Figure 3.14), and total annual *PE* (Figure 3.15). Each of the box and whisker plots presents results for one climate ensemble that contains 30 years of daily data. The bottom and top of the box represent the first and third quartiles, and the band inside the box represent the median. The ends of the whiskers show the maximum and minimum of all the data. It can be seen in Figure 3.13 that the annual precipitation does not show any consistent trend between the climate ensembles. The baseline climate ensemble (#1) shows a maximum, average, and minimum annual precipitation values of 1043, 787, and 562 mm respectively. On the other hand, the future 36 climate ensembles in together (#2-37) show a maximum, average, and minimum annual precipitation of 1333, 813, and 477 mm respectively. Therefore, the 36 future climate ensembles in total show percentage changes in maximum, average, and minimum annual precipitation of around +28, +3, and -15 respectively. On average, the future climate does not show significant change in annual precipitation, but the maximum and minimum annual precipitation show a potential increase and decrease respectively. Therefore, it is expected that the future Toronto climate could experience more wet and dry years while in average annual precipitation could remain almost similar.

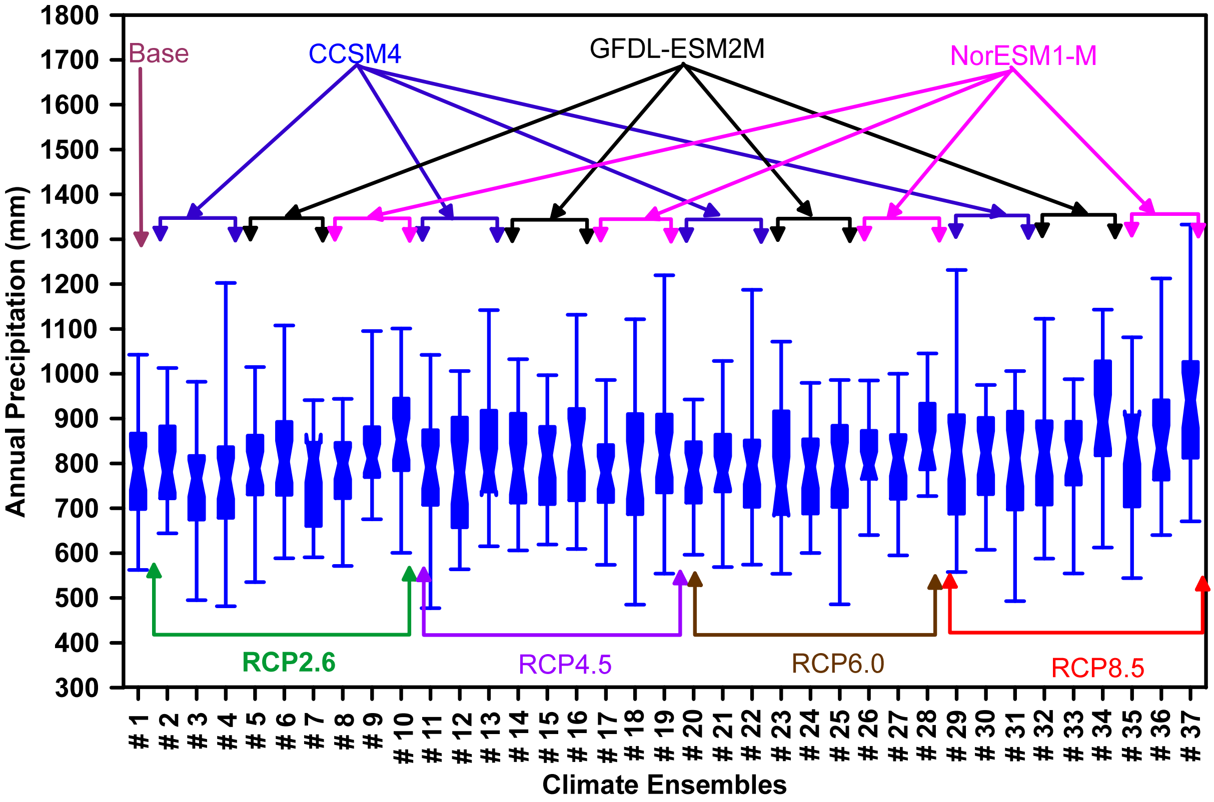

Figure 3.13 Box and whisker plot of annual precipitation for the 37 climate ensembles

The highest increase in the maximum, and average annual precipitation is 28%, and 19% for the climate ensembles # 37. The highest increase in the minimum annual precipitation is 29% for the climate ensemble # 28. While the highest decrease in maximum, average, and minimum annual precipitation is around 10%, 3%, and 15% for the climate ensembles # 7, # 3, and # 11 respectively. The highest difference between the maximum and minimum annual precipitation within a single climate ensemble is 674 mm for the climate ensemble # 29.

The average annual temperature for the 37 climate ensembles is plotted in Figure 3.14. It can be seen that the future temperature predictions show a consistent increasing trend with time from the 2020s to 2080s. It also shows increasing trend from the lower 2.6 to higher 8.5 RCPs. The baseline climate ensemble (# 1) shows a maximum, average, and minimum mean annual temperatures of 10.1, 8.2, and 6.6°C respectively. While the future 36 climate ensembles (# 2-37) show a significant rise in all of these values, and the predicted values are around 16, 10, and 7°C respectively. Therefore, it is clear that on average the future climate could be warmer, and the intensity of the warmer year could increase.

The highest increase in the future maximum, average, and minimum annual average temperature is observed for the climate ensemble 37, and the observed increase amounts are around 6.2, 5.9, and 5.5°C respectively. On the other hand, the lowest increase in the maximum, average, and minimum annual average temperature is around 0, 0.4, and 0.1°C for the ensembles # 20, # 23, and # 5 respectively. The highest difference between the maximum and minimum average annual temperature is 4.29 in the climate ensemble # 24.

Like temperature, potential evaporation also shows an increasing trend with time and RCPs (Figure 3.15). The maximum annual *PE* for the future climate is observed in the climate ensemble # 37, which is around 39% higher than the maximum value of baseline period. This increasing *PE* has potential to increase *AE*, and could counterbalance a fraction of the effects of increasing precipitation. However, the increasing *PE* in the dry years has potential to create soil moisture deficit which could create soil desiccation, and vegetation loss in embankments.

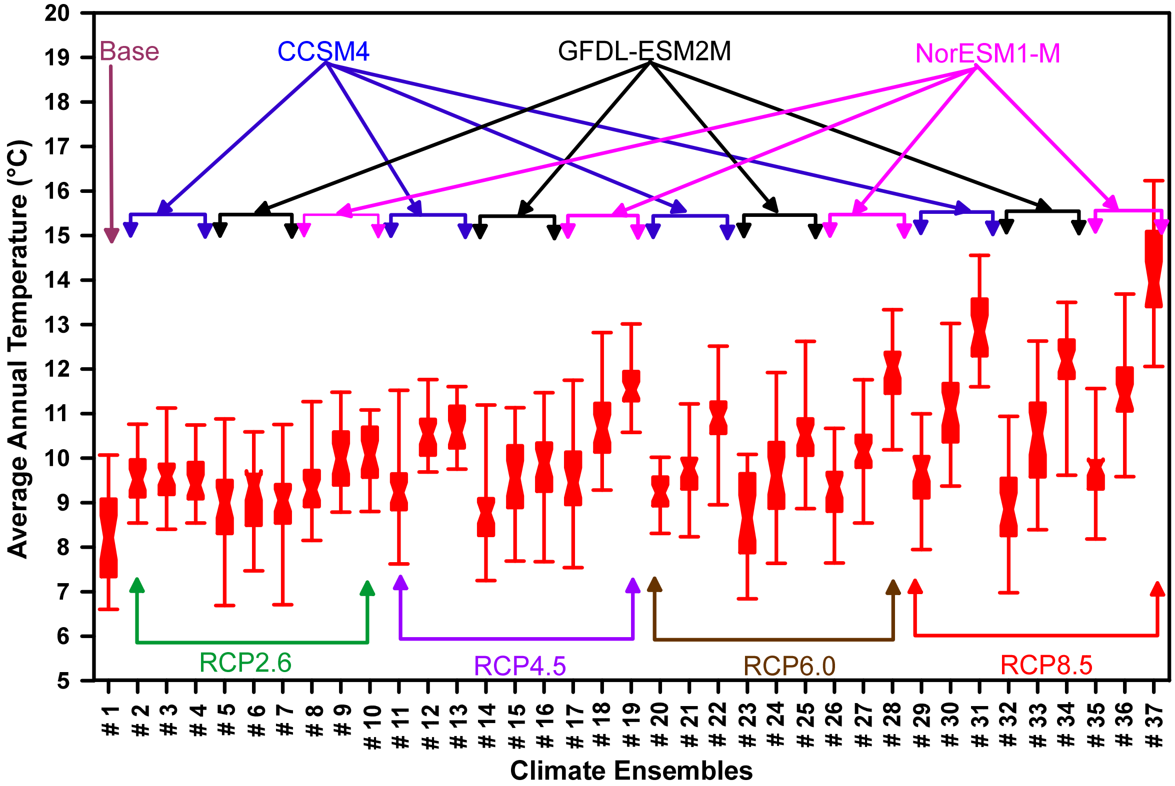

Figure 3.14 Box and whisker plot of average annual temp. for the 37 climate ensembles

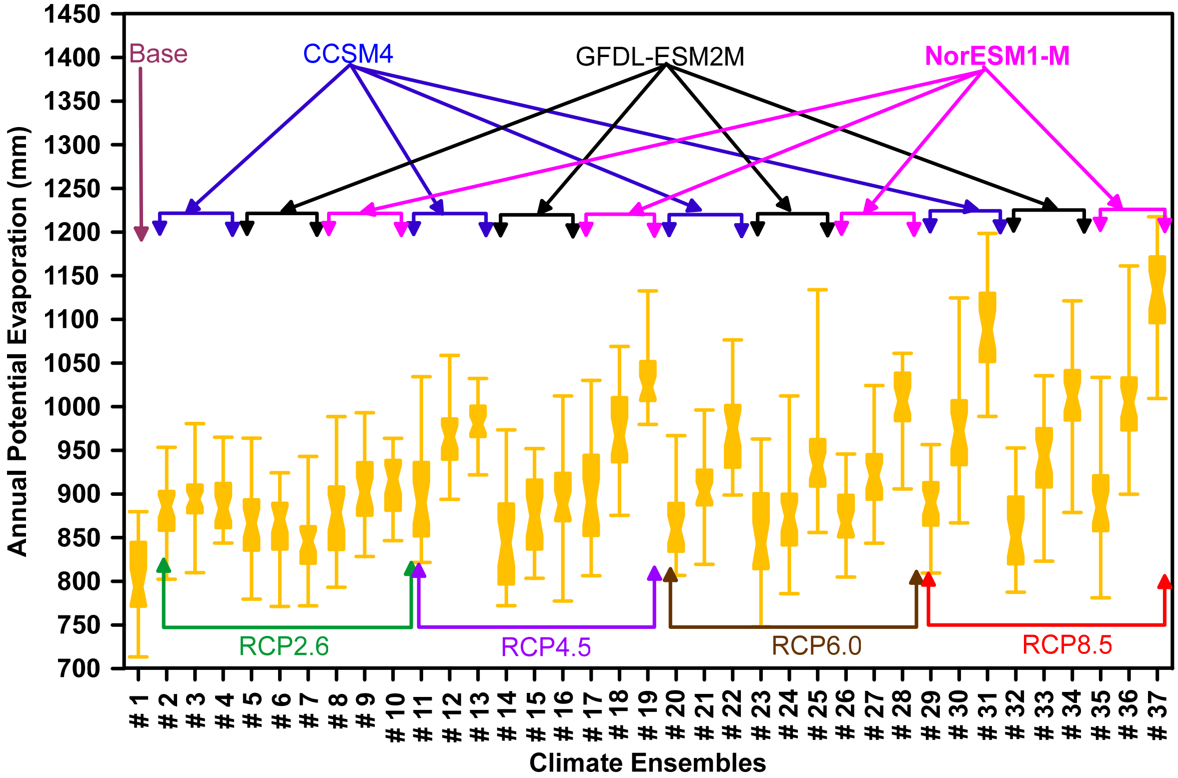

Figure 3.15 Box and whisker plot of annual *PE* for the 37 climate ensembles

The annual *P* and *PE* can be used to estimate water balance at the ground surface using I_m. The annual moisture indices were calculated for the 37 climate ensembles using the Thornthwaite and Hare (1955) method. The results are plotted in Figure 3.16. It is observed that the moisture indices for the future climate fall in the similar range as of baseline climate from the semi-arid to humid. In general, the moisture index for most of the years falls within the dry subhumid range, and therefore, the future Toronto climate also could be classified as dry subhumid. However, there are ensembles that show considerable deviations in the highest and lowest moisture indices in comparison to the baseline values. For example, the highest value of ensemble # 23 is 14% higher than the highest I_m value of the baseline climate, and the lowest value of ensemble # 31 is 66% lower than the lowest I_m value of the baseline climate. The higher differences in the I_m values of future climate could potentially affect the ground surface water balance.

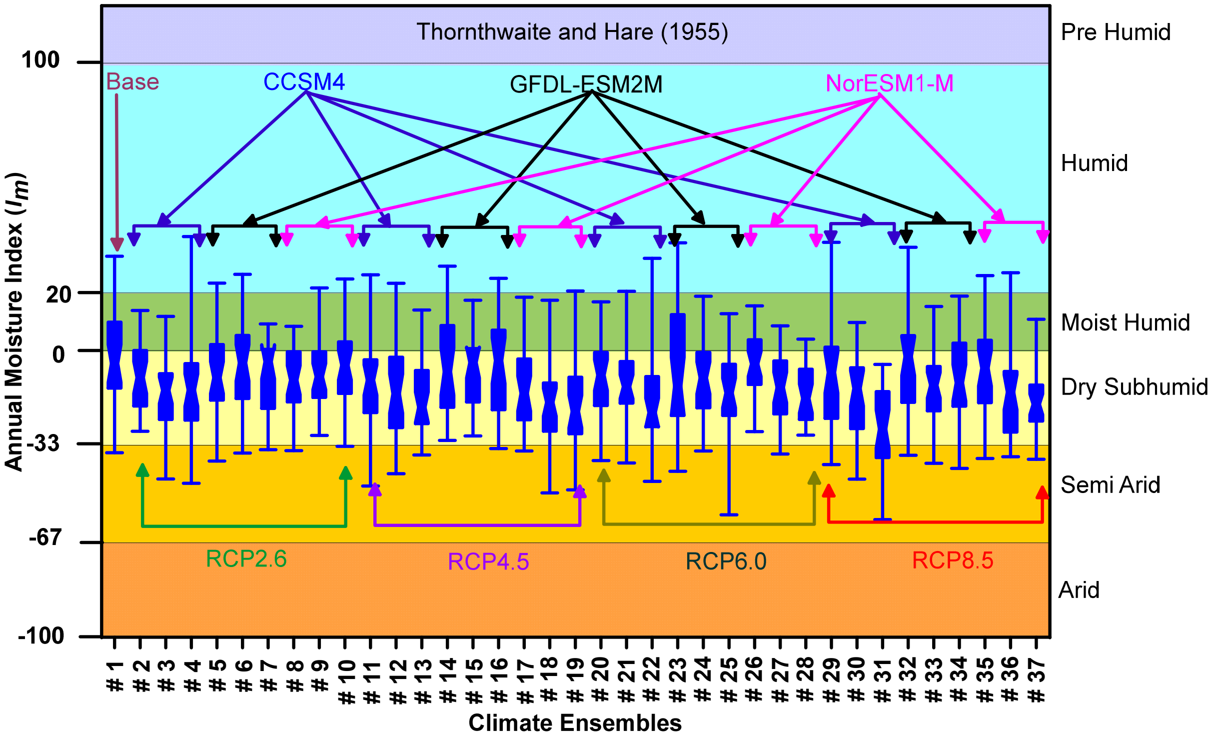

Figure 3.16 Yearly variation of the annual moisture index for the 37 climate ensembles

3.3.5 Predicted probable changes in climate variables

The trends of annual precipitation, potential evaporation, and average temperature have been presented in the previous section. To further investigate the temporal changes in the climate variables, the changes in *P*, *PE*, and mean temperature were calculated. Three time frames were considered to analyze the temporal variability of the future climate variables: (i) water year, starts from the date of freezing and ends to the day before the next date of freezing, (ii) active period, starts from the date of thawing and ends to the date of freezing, and (iii) inactive period, starts from the date of freezing and ends to the date of thawing. The changes in future climate variables over the water year, active, and inactive periods were calculated for the three time periods: 2020s, 2050s, and 2080s. The changes in *P* and *PE* were determined by calculating the percentage increase or decrease in future cumulative quantities with respect to the baseline amounts. The changes in temperature were calculated by subtracting the mean temperature of baseline climate from the future climate. The results are presented in 36 plots in Appendix A. A summary of these results for the precipitation, potential evaporation, and temperature are presented in Figures 3.17, 3.18, and 3.19 respectively.

The temporal changes in cumulative precipitation over water year, active, and inactive periods are shown in Figure 3.17. It can be seen that the majority of the future climate ensembles predict an increase in precipitation over the water year. However, this increasing trend is not uniform over the year. The inactive period shows significant increase in precipitation for almost all the climate ensembles, while a combination of increase and decrease is observed in the active period. On average, the cumulative precipitation over water year shows an increasing prediction with times from 2020s to 2080s. It also shows an increasing trend from lower to higher RCPs (i.e., RCP2.6 to RCP8.5).

Over the water year, total eight climate ensembles show negative (decreasing) trend within [0, -3 %]. However, the magnitude of these negative changes is relatively small (Figure 3.17a). Therefore, it is reasonable to believe that there is likely to be an increasing trend in cumulative precipitation over the water year with times. In general, the projected increase in annual precipitation would be within [0, 5 %] in the 2020s, [0, 8 %] in the 2050s, and [0, 19 %] in the 2080s.

For active period predictions, the CCSM4 model shows a continuous decreasing trend for all the RCPs varying within [0, -8 %]. Other two GCMs also show decreasing trend for several climate ensembles. It is interesting that less than half of the climate ensembles (15 out of 36) only show increasing trend in cumulative precipitation over active period varying within [0, 14 %]. Meanwhile, a significant increasing trend in precipitation is observed over the inactive period for almost all the climate ensembles, and the values are within [0, 31 %].

Based on the above observations, the future active periods are likely to be mildly wetter, while the inactive periods could potentially experience significantly high precipitation. From stability perspective of embankments, the mild increase in precipitation in active period may not create any detrimental effect, however, the increasing precipitation of inactive period could contribute to the volume of snowmelt water at the beginning of the active period, with the potential to impact the stability of embankments.

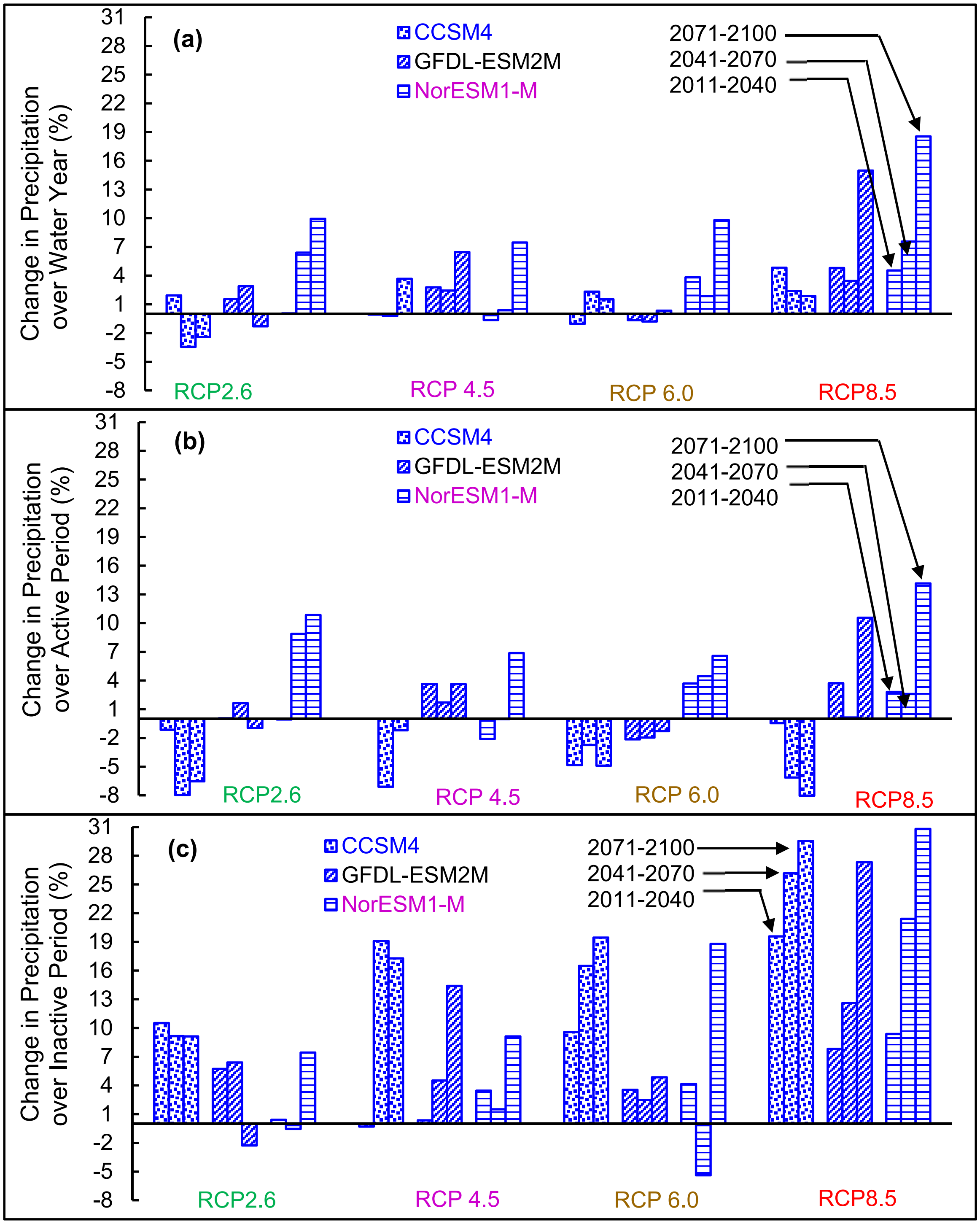

Figure 3.17 Projected percentage changes in annual precipitation over (a) water year, (b) active period, and (c) inactive period

The changes in mean temperature over the water year, active and inactive periods are shown in Figures 3.18a, b, and c respectively. The changes in mean temperature were calculated by subtracting the average value of BC from the FC. It can be observed that all the three GCMs show a consistent increasing trend with the RCPs and times. RCP2.6 shows the lowest increment while the highest change is observed in the RCP8.5. The temporal variation shows a gradual increasing trend from the 2020s to 2080s. However, the increase in average temperature is almost consistent over the year, and does not show any noticeable variations over the water year, active, and inactive periods. The ranges of variations are [0.5, 5.9 °C], [0.6, 6.2 °C], and [0, 5.3 °C] in the water year, active, and inactive periods respectively. Therefore, it can be concluded that the future temperature in Toronto would increase gradually with time, and the rate of increment is almost consistent over the year.

The percentage changes in *PE* were calculated for the active period only. Since the Pereira and Pruitt (2004) method is not applicable for the negative temperature in inactive period, the cumulative *PE* in active period, and water year are same. Moreover, the water movement at the ground surface during the inactive period can be assumed negligible, and it could be meaningful to ignore the inactive period from the numerical simulations. Therefore, the trend of *PE* in active period was only investigated, and the results are shown in Figure 3.19. It can be seen in Figure 3.19 that the *PE* follows the temperature trend, and gradually increases with times, and RCPs. However, the magnitudes of percentage changes in *PE* are considerably higher. The range of variation is [5, 40 %]. This high increase in *PE* could potentially influence the ground surface water balance, and pore pressures within embankments.

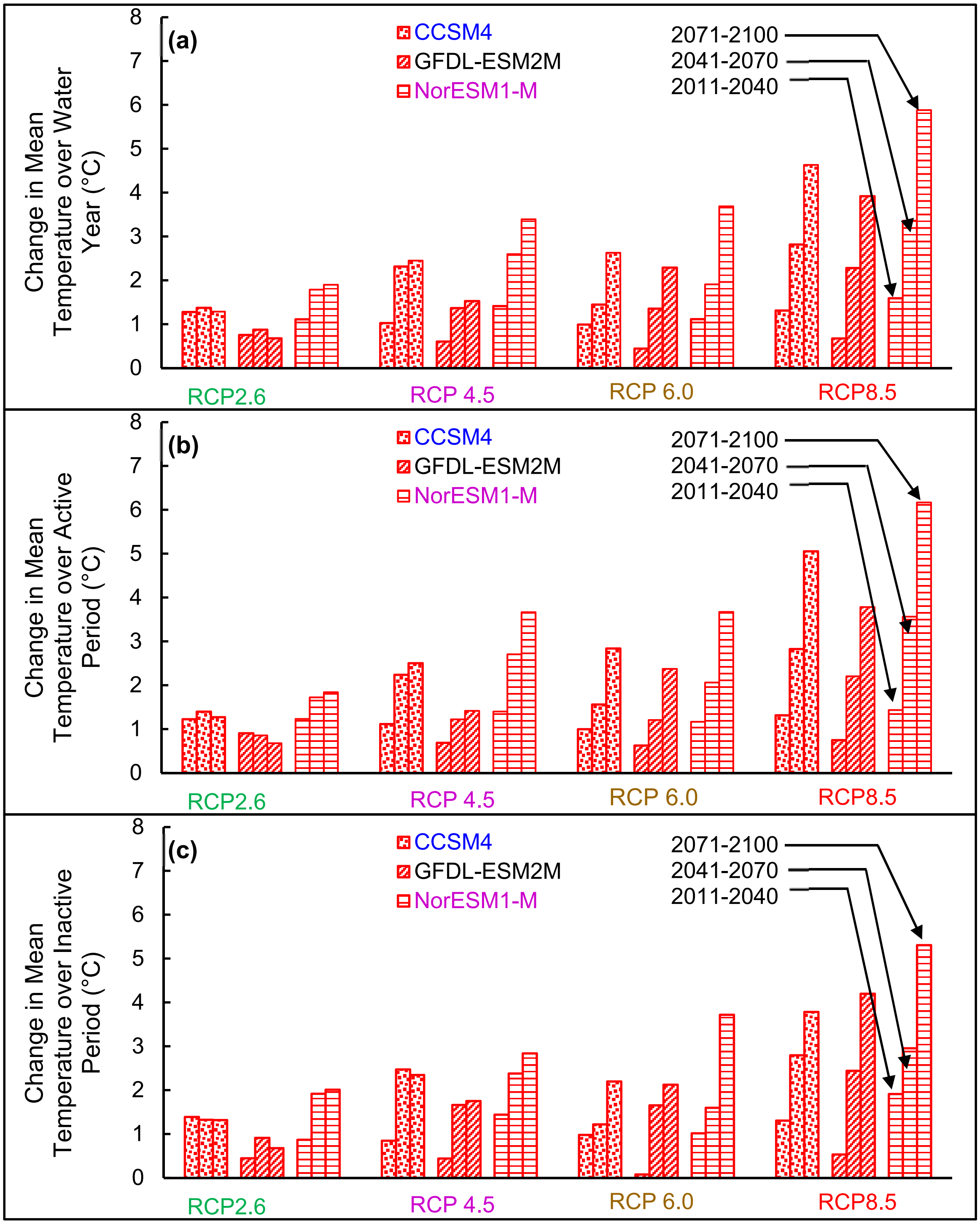

Figure 3.18 Projected changes in mean temperature over (a) water year, (b) active period, and (c) inactive period

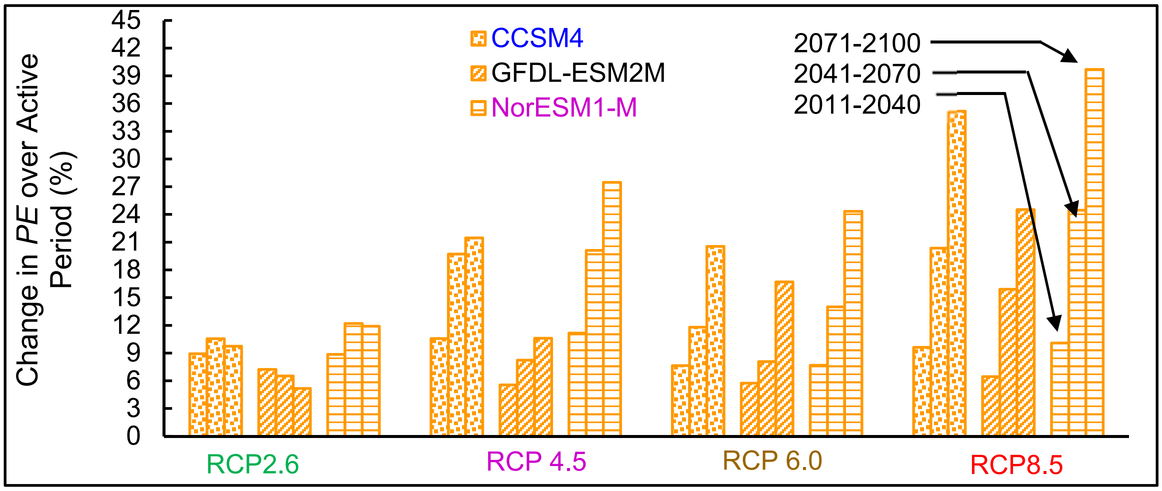

Figure 3.19 Projected percentage changes in *PE* over active period

3.4 Extreme Precipitation Events

Extreme precipitation events have frequently triggered embankment failures, and require special attention (Kim et al. 2012). Any change in the intensity, and frequency of extreme precipitation events affect the stability of embankments. Therefore, it is important to analyze the probable changes in extreme precipitation events for the future climate.

3.4.1 Studying extreme events with Climate Ensembles

Thirty years of historical daily precipitation data was analyzed to identify the extreme precipitation events. It is observed that total 28 precipitation events are 40 mm and higher, 14 of these are 50 mm and higher, 4 of these are 60 mm and higher, and 1 of these is 70 mm and higher (Figure 3.1a). On average, the 40 mm and higher precipitation events occurred almost in every year for the period comprising 1981-2010. Therefore, 40 mm events can be defined as 1 year return period storm, and were considered as extreme precipitation event in this research.

The numbers of 40 mm and higher precipitation events were estimated for each of the 36 future climate ensembles. The results were reported as change from the baseline value of 28 events over 30-year period. The detailed results are presented in Appendix A. A summary of the results is shown in Figure 3.20. It can be seen in Figure 3.20a that there is an obvious increasing pattern in the numbers of extreme precipitation events over the water year. Even though a few future climate ensembles (8 out of 36) have a decreasing trend, the average number of decrease in extreme precipitation event is around 4. Therefore, it can be considered that the future climate is likely to experience frequent extreme precipitation events. Among 36 future climate ensembles, 28 show an increasing trend with an average number of extreme event of 10. However, the highest number of increase in extreme precipitation event is 32 for the climate ensemble # 37, which would employ an increase of 114%.

To further analyze the projected increasing trend of extreme precipitation events over the active and inactive periods, the changes in extreme precipitation events over the active and inactive periods were calculated. The results are presented in Appendix A in detail. A summary of the results is shown in Figure 3.20b, and Figure 3.20c for the active and inactive periods respectively. It can be observed in Figure 3.20b that in the active period, 29 climate ensembles predict increasing trend in extreme precipitation events with an average number of extreme events of around 7, while 22 climate ensembles show increasing trend in the inactive periods with an average number of extreme events of 3. In Figure 3.17, it has been observed that the increase in precipitation in inactive period is higher than the active seasons, but Figure 3.20 shows that the active seasons are likely to experience more frequent extreme precipitation events compare with the inactive seasons. These shifts in extreme precipitation patterns could have significant impact in the water balance, pore pressures, and eventually the stability of embankments. Therefore, it is important to study the impacts of these increasing extreme precipitation events on the stability of embankments.

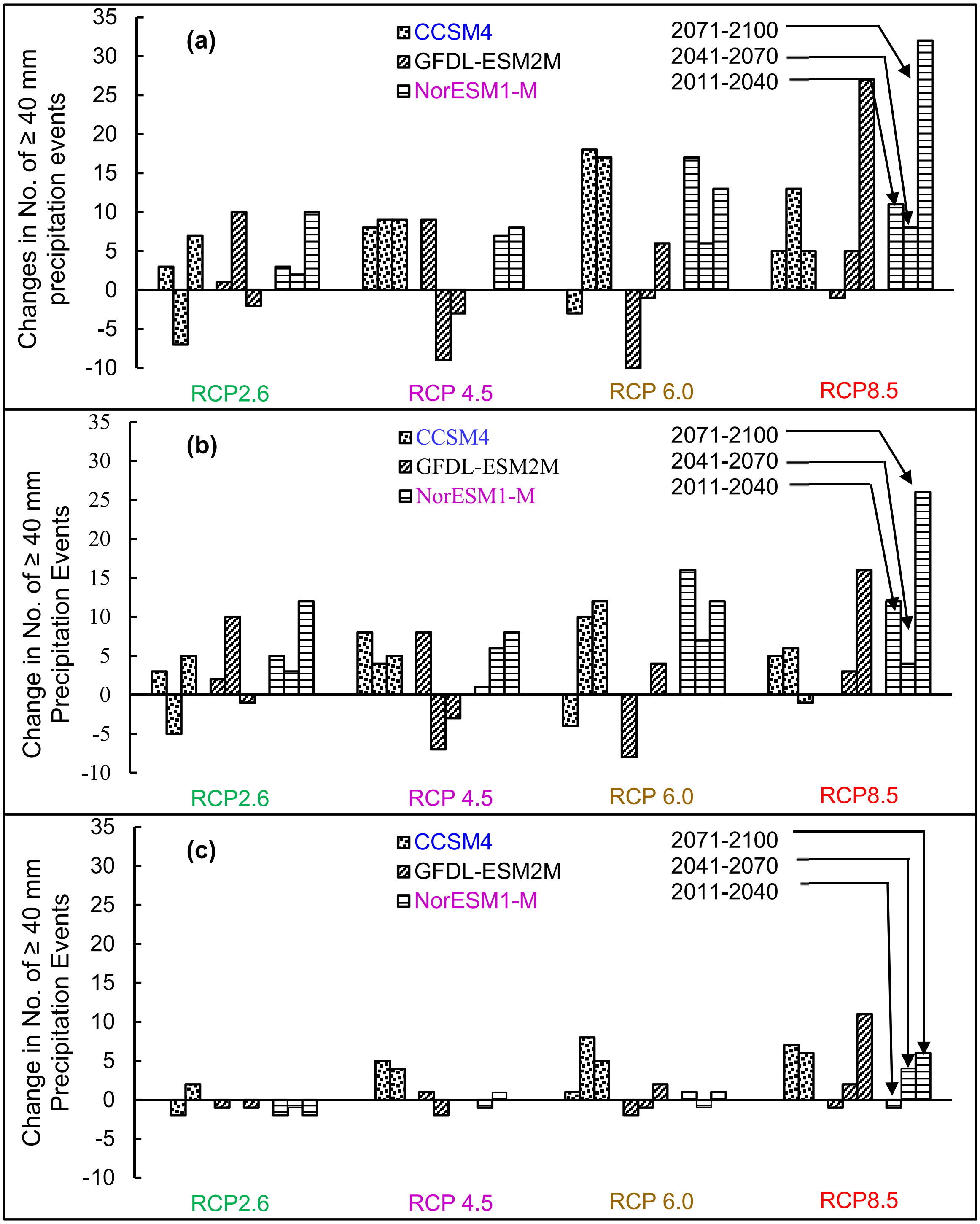

Figure 3.20 Changes in number of extreme precipitation events (≥ 40 mm) over (a) water year, (b) active period, and (c) inactive period

3.4.2 Studying extreme events with IDF curves

The effect of extreme precipitation events on infrastructures (hydrological, geotechnical, etc.) is frequently studied using intensity duration and frequency (IDF) curves (e.g., Robinson et al. 2017, Vahedifard et al. 2017). The impact of future climate change on embankments also has been studied using IDF curves (e.g., Robinson et al. 2017). The changes in extreme events can be easily understood by comparing the future IDF curves with the baseline IDF curves. If potential changes are observed, then the future IDF curves can be applied to determine the impact of future extreme events, and the results can be compared with the results of the baseline IDF curves.

Two potential sources of future IDF curves for Ontario are the Ontario climate change data portal (CCDP 2017), and the IDF curve lookup of the Ministry of Transportation Ontario (MTO 2017). The CCDP contains IDF curves for one baseline and three future periods for Ontario at a 25 km × 25 km resolution. Total 9 different percentiles of precipitation were considered. The climate data was generated using a RCM named PRECIS. The boundary condition was derived using a GCM called HadCM3 under the emission scenario A1B of special report on emission scenario (SRES) (Wang et al. 2014). On the other hand, the IDF curve lookup of MTO used station data from the Environment Canada, and the national oceanic and atmospheric administration (NOAA), and developed IDF curves for Ontario for the baseline and future periods by spatial and temporal interpolations (MTO 2017).

The performance of the two sources IDF curves were investigated by comparing the 90 and 50 percentiles IDF curves of CCDP with the IDF curves of MTO for the 2080s. The results are presented in Figure 3.21. It can be seen in Figure 3.21 that for both percentiles IDF curves of CCDP show higher estimation for most of the return periods and durations. However, for the storms of lower return periods (i.e., 2-year) the IDF curves of CCDP show slightly lower estimation for the lower durations (i.e., 5-30 minutes). Apart from the 2-yr return period IDF curve, IDF curves of MTO are within the upper and lower bound of IDF curves of CCDP. Therefore, the IDF curves of CCDP were selected in this study to use.

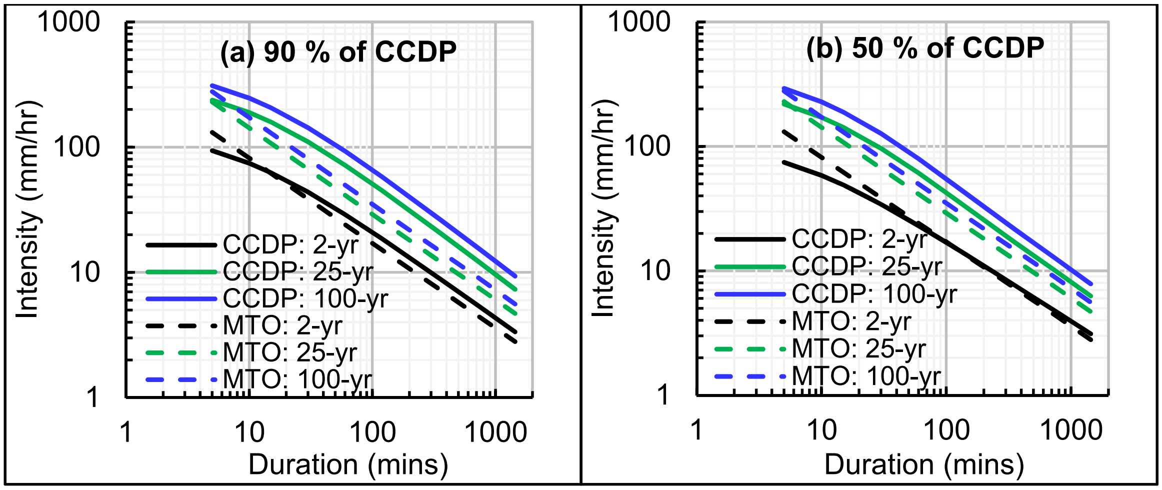

Figure 3.21 Comparison between IDF curves of CCDP and MTO

The IDF curves of CCDP for the baseline and three future periods for the city of Toronto are shown in Figure 3.22. It can be seen in Figure 3.22 that the future IDF curves show a clear deviation from the baseline curves. For example, the intensity of the 100-yr. storm of duration of 100 minutes for the baseline climate is around 30 mm/hr., however, the intensity for the three future periods is around 60 mm/hr. which is double the value for baseline period. Similar observations can be made for other durations and return periods. It is interesting to note that the future IDF curves do not show any significant difference between 2020s, 2050s, and 2080s. Therefore, based on prediction of CCDP, it can be concluded that the frequency and intensity of extreme events would increase up to 2020s, and then become stabilize.

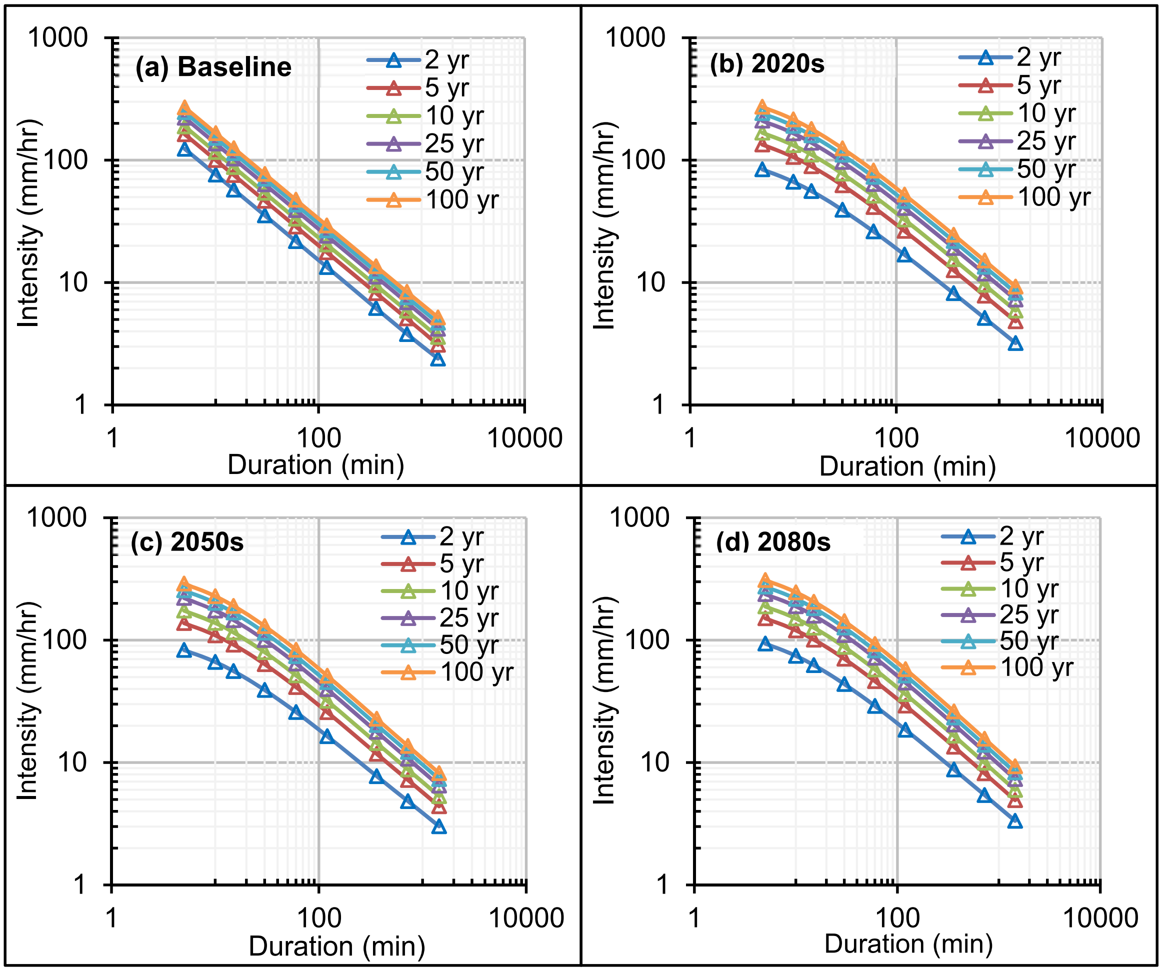

Figure 3.22 Projected IDF curves for the city of Toronto (a) Baseline, (b) 2020s, (c) 2050s, and (d) 2080s (Wang et al. 2014)

3.5 Construction of Design Climates

Based on three sets of trend analyses a considerable change is likely to occur in the future climate of Toronto. Because these changes could affect the stability of existing embankments, it is important to select an appropriate design climate that will allow for proper modifications to embankment design specifications.

The selected design climate should be able to predict the lowest factor of safety possible in the slope stability analysis of a soil embankment. The factor of safety is a function of pore pressures distribution which is directly affected by climate. A wetter climate in general can create pore pressures distribution which results in lower FOS. Therefore, the design climate should contain the possible wettest condition. In this study, the first set of design climates (DC1) was selected to study the effects of changes in daily climate variables over long period of time (i.e., 30 years). Three climate ensembles were selected: ensemble #1, BC as datum; ensemble #23, FC with highest I_m (Figure 3.16); and ensemble # 37, FC with highest annual precipitation (Figure 3.13). Higher I_m indicates more availability of meteoric water and less evaporative demand at the ground surface. Although the I_m values of ensemble # 37 are not high due to higher evaporative demand, it is expected that the higher amount of precipitation will affect the stability of embankments.

In most instances the historical data is available at daily resolution and so is the future climate (FC) data. However, the actual intensity of the event can vary form a few minutes to hours. The resolution of the precipitation data for the Design Climate 1 (DC1) is daily. To address the effects of temporal resolution of precipitation, the historical extreme precipitation events were compared with the IDF curves, and more realistic resolutions were selected. This procedure of higher resolution design climate construction has been applied in similar types of studies, and satisfactory performance was obtained (e.g., SRK Consulting Inc. 2010).

The historical records of daily precipitation with the number of extreme events are shown in Figure 3.23a, and the depth duration frequency (DDF) curves for the same period are shown in Figure 3.23b. For ease in comparison, the IDF curves were converted to the DDF curves. Now, if the 50 mm storms are selected it can be seen in Figure 3.23a that 14 such storms were recorded in past 30 years, which gives a return period slightly higher than 2 yr. Next, if the DDF curve of 2 year return period is selected from the Figure 3.23b, it can be observed that the 12 and 24 hour storms are 46, and 57 mm respectively. The historical record shows that the 50 mm storm has a return period higher than 2, therefore, storms of 2 year return period should be lower than 50 mm which agrees with 12-hour duration. Therefore, it could be meaningful to distribute the daily precipitation over 12 hours to accurately address the effects of resolution of precipitation data. Similar results are observed for other extreme events, and 12-hour duration was selected for regular precipitation. To test the effects of higher intensity precipitation events, additional resolutions of 1 and 2 hours were selected. Comparison to the DDF curves show that the 2 hr. event represents 10-25 year return periods, while 1 hr. represents 50-100 year return periods.

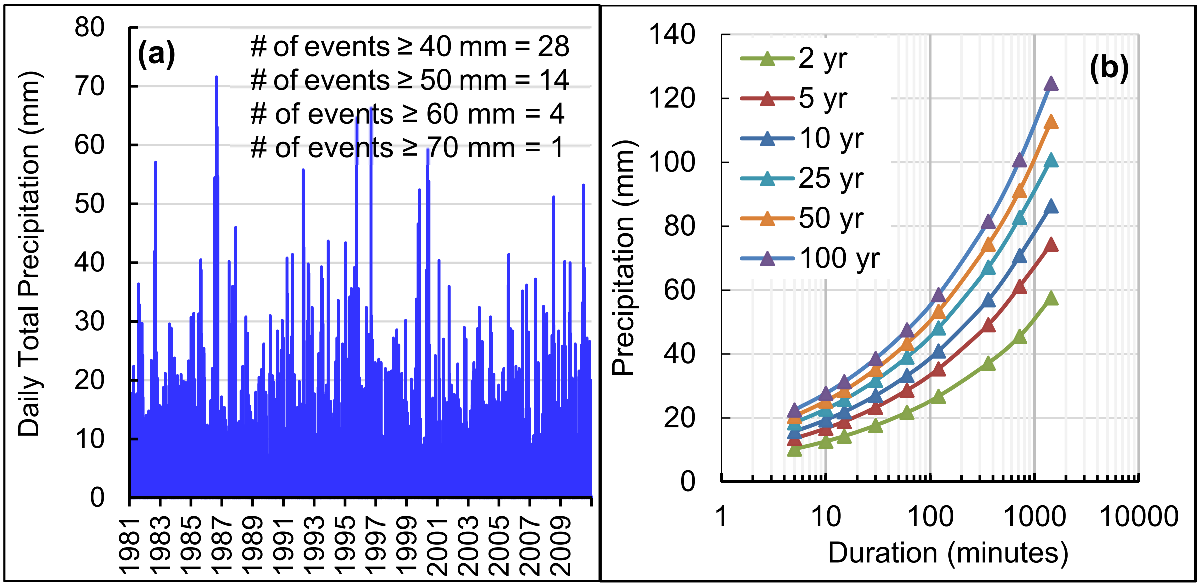

Figure 3.23 (a) Daily cumulative precipitation with extreme events for the baseline climate (b) depth duration frequency curves for the baseline climate

The second Design Climate dataset was selected to study the effects of future extreme events. Two sets of IDF curves were selected for the baseline and future climates (Figure 3.22). Since the future climate does not show considerable changes in the extreme events from the 2020s to 2080s, only the IDF curves of 2020s were selected. Each IDF curve contained 6 different return periods, and 9 different durations. All the 6 return periods were selected for this study; however, only one duration was considered. It is observed that the effects of intensity and duration of storms are controlled by the hydraulic properties of fill materials of embankments, and therefore, only the critical duration was considered. Details about the relationship between the hydraulic properties of fill materials and intensity and duration of storms is presented in Chapter 5, along with the selection procedure of the critical duration.

Chapter 4. Design Parameters of the Soil Embankment

4.1 Embankment Geometry

A design profile of a highway embankment was created based on previous MTO studies, and Ontario Provincial Standard Specification (OPSS) of design and construction of highway embankment. The design embankment profile is shown in Figure 4.1. Due to the symmetry of the highway embankment profile, only one half of the embankment is shown in Figure 4.1 (cut along the center line). By modelling only one half of the symmetrical embankment, the numerical modelling computational time is significantly reduced. The crest of the highway embankment is 7 m high, and is 25 m wide with 22 m of pavement and 3 m of unpaved shoulder. Following OPSS of highway embankment design, an embankment slope of 2H:1V was selected, resulting in a 14 m wide slope. Similar studies have shown that the distance between the toe of the embankment and the edge boundary of the embankment profile should be at least 3 times the height of the slope to avoid the effects of the vertical boundary conditions in the results of numerical simulations (e.g., Rahardjo et al. 2010, 2013). Therefore, there is 26 m of ground surface past the toe of the slope in the embankment profile (Figure 4.1) resulting in a width of 65 m for the complete profile.

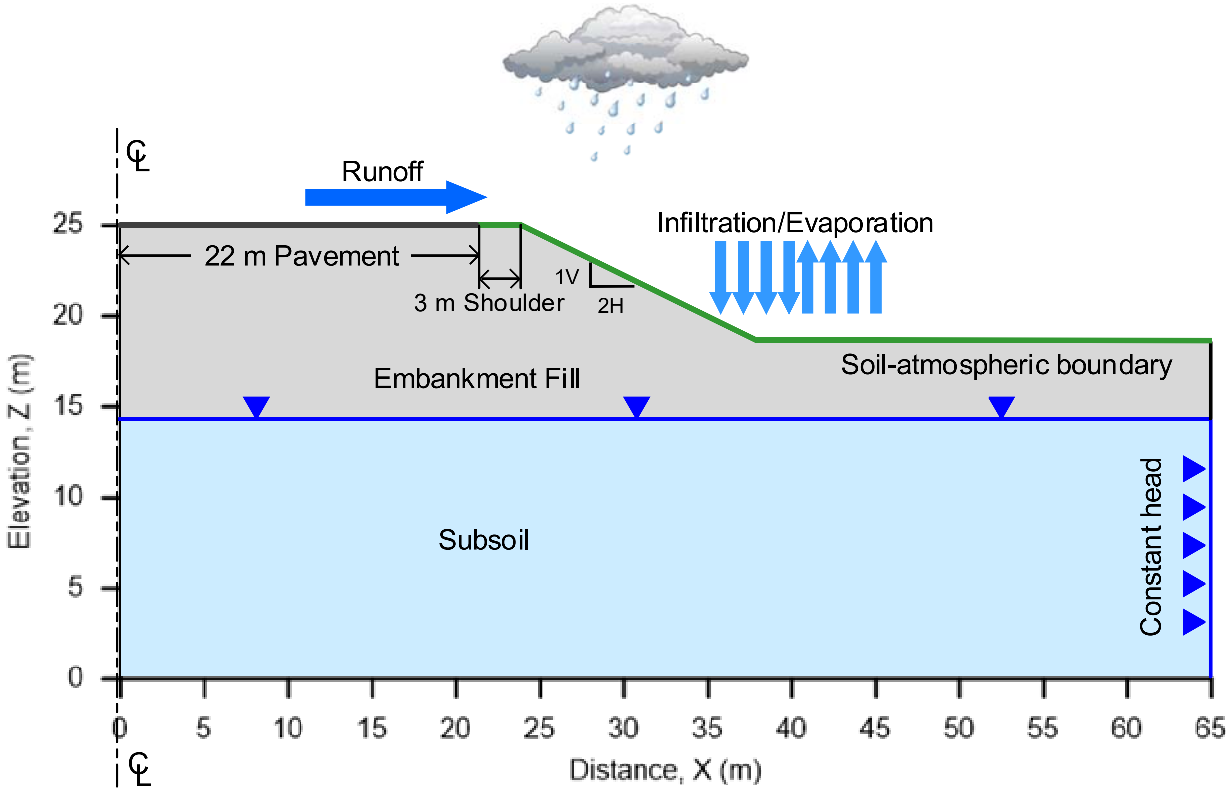

Figure 4.1 Design profile of the highway embankment

A foundation investigation and design report (Golder Associates 2015) of MTO was selected for the highway embankment section to review design parameters. A review of the fill materials indicated that there were three groupings of fill materials that were named as: gravel and sand, sand and silt, and clayey silt (Golder Associates 2015). The strength properties of the three different fill materials are quite similar, although the grain size distributions showed large variation. Based on the grain size information the three fill materials; gravel and sand, sand and silt, and clayey silt were classified using United State Department of Agriculture (USDA) textural classification system as loamy sand, sandy loam, and silt loam respectively.

The review of the subsoil materials indicated that subsoil mostly contains medium to low permeable till (Golder Associates 2015). The strength properties of the tills were similar. It was also found that the groundwater table is at the ground surface, and the subsoil is saturated. The hydraulic property of saturated soil is constant, and therefore, a simplified subsoil setting can be considered for the highway embankment. As such, a simplified subsoil containing a single soil was selected. From the grain size data, it was found that the tills mostly fall in the silt loam range in the USDA classification system. Therefore, the subsoil material was named as silt loam.

4.2 Soil Properties

In order to model the impact of climate change on the stability of a soil embankment, the soils hydraulic and strength properties must first be known. The following sections describe the methodology of selecting the soil properties for this study.

4.2.1 Estimation of hydraulic properties

Soils hydraulic properties can be measured, either in the laboratory or in the field. These measurements are time consuming and costly. Therefore, it is common to estimate hydraulic properties from readily available soil information. Many methods for estimating the soil hydraulic properties have been developed over the years which are commonly known as pedotransfer functions (PTFs) (e.g. Gupta and Larson 1979, Rawls et al. 1982, 1983, Rajkai and Várallyay 1989, Vereecken et al. 1989, Tomasella and Hodnett 1998, Wösten et al. 1999, Schaap et al. 2001). Most of the PTFs are empirical in nature and require different input variables (Schaap et al. 2001). The performance of these PTFs has been investigated, and it has been reported that these methods can be quite effective in estimating the soil hydraulic properties (e.g., Alvarez-Acosta et al. 2012).

In total, eight different PTFs for estimating hydraulic properties of the fill materials for this research were used. Details of the selected PTFs are presented in Table 4.1. It can be seen in Table 4.1 that each of the PTFs has different input data requirements, and is capable of estimating parameters for the van Genuchten SWCC model.

Table 4.1 Details of the selected eight PTFs

#	PTF	SWCC model	Soil properties used in PTF				
			Sand %	Silt %	Clay %	OC[1] %	DD[2] g cm^{-3}
1	Gupta and Larson 1979	WH[3] -> VG	+	+	+	+	+
2	Rawls et al. 1982	WH -> VG	+	+	+	+	+
3	Rawls et al. 1983	WH -> VG	+	+	+	+	+
4	Rajkai and Varallyay 1992	WH -> VG	+		+	+	+
5	Vereecken et al.1989	VG[4]	+	+	+	+	+
6	Tomasella and Hodnett 1998	WH -> VG		+	+	+	
7	Wosten et al. 1999	VG	+	+	+		
8	Schaap et al. 2001	VG	+	+	+		

[1] OC – Organic Content
[2] DD – Dry Density
[3] WH – water content at fixed capillary pressure
[4] van Genuchten model

The calculated VG parameters for the three fill materials using the eight different PTFs are shown in Figure 4.2. The variation between the different estimates are also presented in this figure in terms of the mean (μ) value and standard deviations (σ). In addition, these predictions are compared with the mean and standard deviation values of the loamy sand, sandy loam, and silt loam textural classes from Carsel and Parrish (1988) in the same figure. Carsel and Parrish (1988) reported a catalog containing mean and standard deviation values of VG parameters for 12 different USDA textural classes.

It is seen in Figure 4.2 that there is a wide range of predictions for the four van Genuchten parameters (θ_r, θ_s, n, α) across all eight methods. Yet, in the majority of cases the predictions are within ± σ range. The predictions also show a good agreement with the ranges reported by Carsel and Parrish (1988). The ranges of the predicted values of the three fill materials showed that the loamy sand has the highest hydraulic conductivity and silt loam the lowest. Based on these results, two fill materials for the soil embankment were selected for numerical modeling in this research, loamy sand (hereinafter named sand) and silt loam (hereinafter named silt). The properties of sandy loam fall in between sand and silt, and sandy loam was not considered for numerical modeling.

The mean of the predicted eight values of the VG parameters was selected to construct SWCC of the sand and silt fills. It should be noted that the predicted eight values and standard deviations in Figure 4.2 provide a possible range of VG parameters from different PTFs which can be used to conduct parametric studies to investigate the effects of different hydraulic properties.

The subsoil of the highway embankment was assumed homogeneous. The VG parameters of the subsoil material (silt loam) were taken from the catalog of Carsel and Parrish (1988). The same source was also used for the saturated hydraulic conductivity of the fill materials (sand and silt). Using their respective VG parameters, SWCCs were constructed for the fill material: sand and silt, and for the subsoil material: silt loam using van Genuchten (1980) model. The unsaturated hydraulic conductivity functions were estimated using Mualem (1976) model. The plots of the SWCCs and hydraulic conductivity functions are shown in Figure 4.3 and Figure 4.4 respectively. It can be seen in these figures that the sand has the highest drainage properties, while silt has the lowest. Properties of silt loam fall somewhere in the middle.

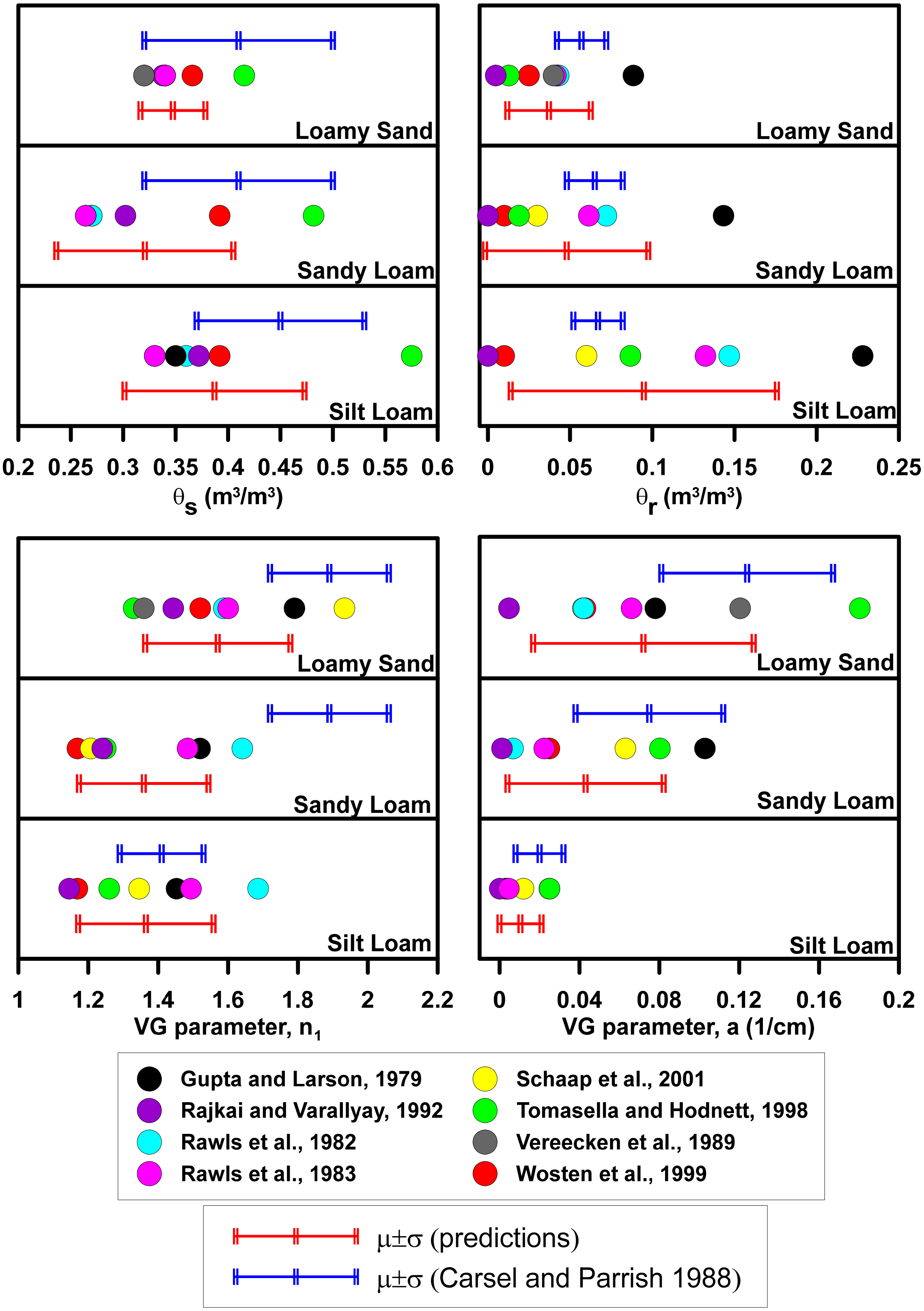

Figure 4.2 Predicted soil hydraulic properties of the fill materials

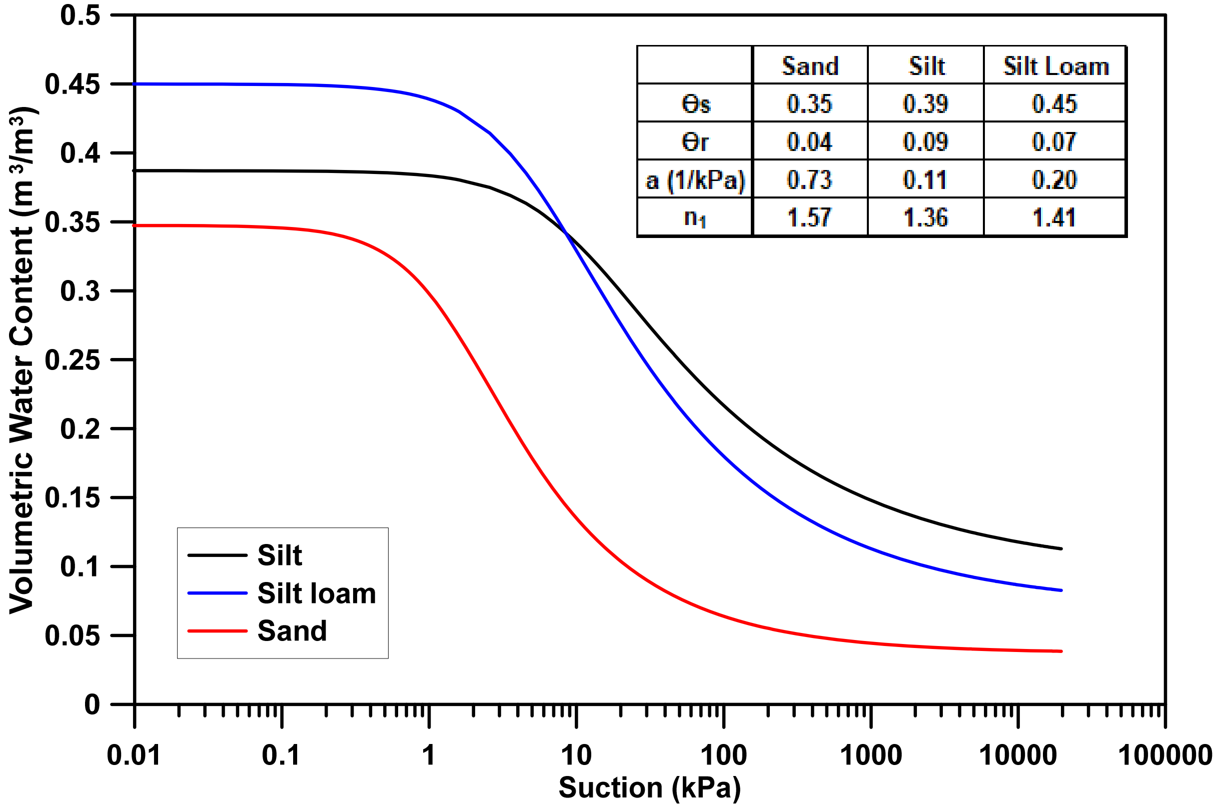

Figure 4.3 Soil water characteristic curves (model: van Genuchten 1980)

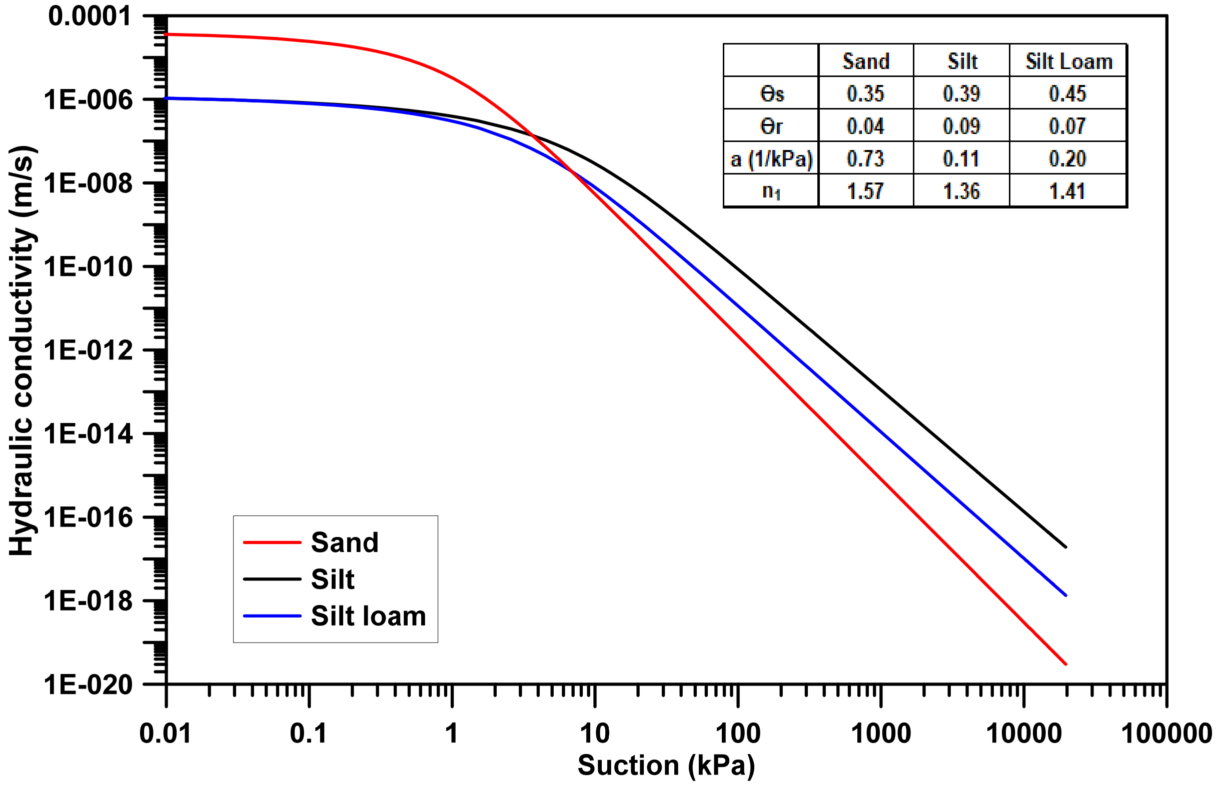

Figure 4.4 Hydraulic conductivity functions (model: Mualem 1976)

4.2.2 Strength properties

The strength properties of the subsoil and fills of embankments were chosen based on the values used in the foundation investigation and design report of MTO (Golder Associates 2015). It was found that the subsoils have friction angles ranging from 24 to 36 degrees. In this study, an average friction angle of 32° was selected for the subsoil silt loam material. The strength properties of fill materials are quite similar, and found varying from 30 to 34 degrees. As such, an average friction angle of 32 was selected to use. It was also found that both fill materials and the subsoil were modelled with zero effective cohesion, and therefore cohesion was ignored in this study. The unit weight, effective cohesion, and effective friction angle of the soils are summarized in Table 4.2.

Table 4.2 Selected effective strength properties of the fill and subsoil materials

Material name	Unit Weight γ (kN/m^3)	Effective Cohesion c' (kPa)	Effective Friction Angle ϕ' (deg.)
Sand	19	0	32
Silt	21	0	32
Silt loam	21	0	32

Chapter 5. Numerical Model Methodology and Development

5.1 Hydrological Modeling

5.1.1 Selection of hydrological software

A review of commonly used hydrological modeling software was presented in Section 2.6. It was found that two software could be used in this research: HYDRUS-2D and VADOSE/W. The performance of these software for this study was investigated by simulating a hypothetical homogeneous embankment with 30 years of climate for the city of Toronto as the top boundary. The calculated water balances at the ground surface from the two software are shown in Figure 5.1. It can be observed that the calculated cumulative water fluxes from both this software are in excellent agreement with each other. It should be noted that although results were similar for these software, the run times for the two software were very different. Over several repeated simulations, it was found that run times for VADOSE/W were significantly higher than those for HYDRUS-2D. Considering that a large number of simulations with 30 years of climate were required for this research as such HYDRUS-2D was selected as the hydrological modeling software for the design climate 1 (DC1).

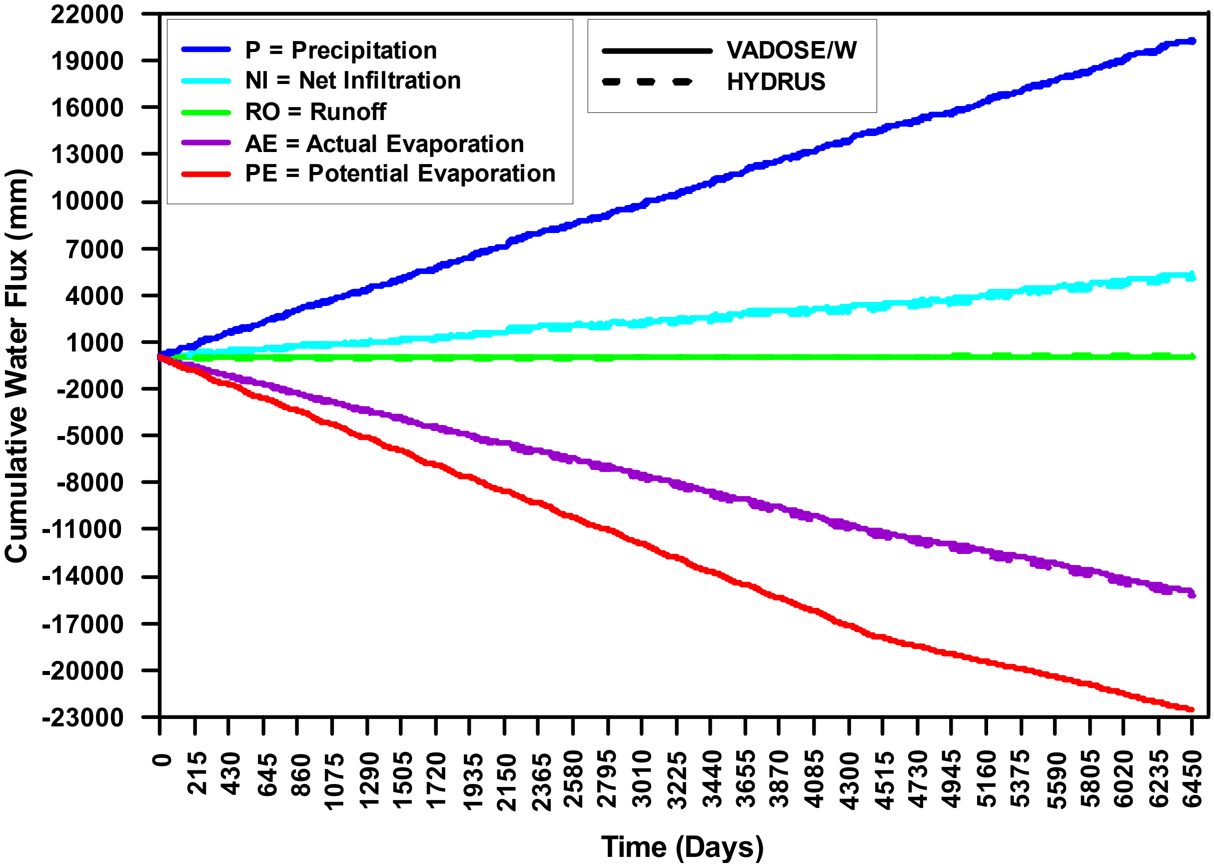

Figure 5.1 Ground surface moisture balance for 30 years of city of Toronto climate computed using VADOSE/W and HYDRUS

On the other hand, design climate 2 (DC2) contains two sets of IDF curves with duration 1 and 24 hours. The simulation times in numerical models for these IDF curves were equal to its durations. Therefore, over the whole simulation times precipitation comes continuously in a constant rate, and a large amount of water enters into the system. While the evaporation rate during continuous precipitation is negligible, and can be ignored when studying with IDF curves (e.g., Robinson et al. 2017). As such, for DC2 the soil-atmospheric boundary was not required to use, and can be modeled using a flux boundary condition. The SEEP/W is the seepage module of the GeoStudio package, and can be used in simulating saturated unsaturated water flow. Moreover, since both the SEEP/W and SLOPE/W are parts of the same software suite GeoStudio, they allow easy coupling and continuous factor of safety calculation facility for all simulation time steps. Therefore, SEEP/W was selected to conduct hydrological modeling for DC2.

5.1.2 Design Climate 1 – Hydrological Model

The first set of hydrological models was developed for DC1 using HYDRUS-2D. A design profile of the initial model is shown in Figure 4.1. The finite element (FE) mesh, boundary conditions, and three PWP recording sections of the HYDRUS-2D model are shown in Figure 5.2. The mesh comprised of 13868 2D elements. A global mesh size of 1 m was used for the whole domain. The density of the surface elements along the soil-atmospheric boundary was refined to 0.1 m to capture the near ground surface transient localized pore-water pressures changes. The pavement at the crest of the embankment was modeled as a no flow boundary. A no flow boundary was also assigned at the left side and bottom of the embankment. At right hand boundary groundwater table was assumed to be a depth of 4 m from the surface of the embankment and section above water table was assumed to be a no flow boundary.

A soil-atmospheric boundary comprising of daily precipitation and potential evaporation records was applied at the soil-atmospheric interface. The runoff from the pavement was distributed over the soil embankment using appropriate method described in the following section. Three sections were selected at the middle, top half, and bottom half of the slope to investigate the temporal variations of the PWPs. The initial condition of the hydrological model was generated by running an initial model for 30 years of historical climate of city of Toronto starting from a static groundwater table at 4 m. The last time step of this initial model was used as initial condition for models that were run using DC1. Three hydrological models were simulated for the three selected climate ensembles, and each of the embankment (Sand & Silt). Only the active period (1 April to 30 November) of the water year was considered for the simulation, which amounts to a total of 7320 days for the 30 years of city of Toronto climate.

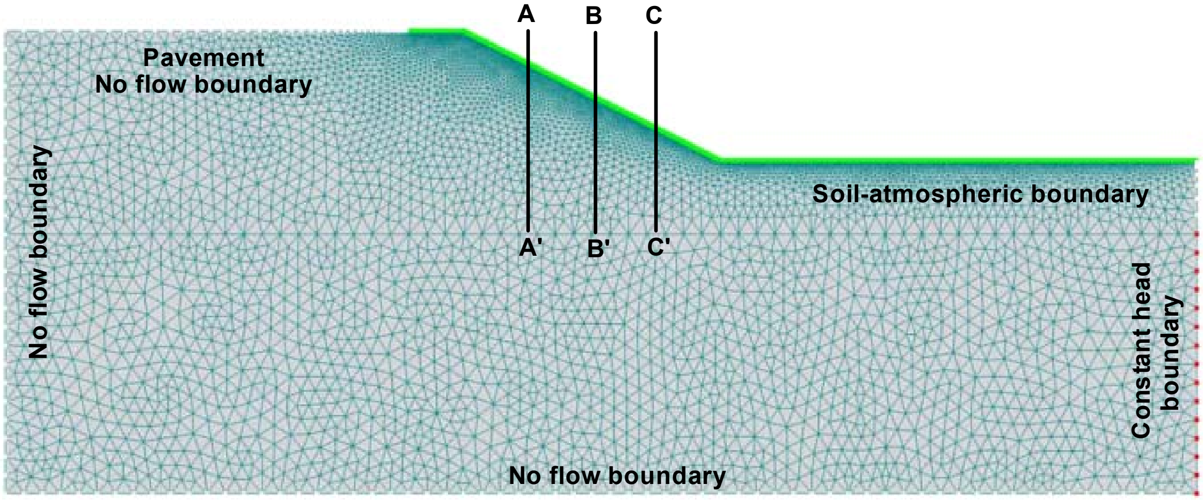

Figure 5.2 FE mesh, boundary conditions, and three PWP recording sections of the HYDRUS-2D model

5.1.3 Design Climate 2 – Hydrological Model

The second set of design climate contained short-term (1 hour to 24 hour) precipitation events, and therefore, special attention was required to obtain accurate estimation of PWPs, from a temporal and spatial perspective. The same design profile as shown in Figure 4.1 was used to develop the hydrological models using SEEP/W. A finite element mesh containing 3955 nodes, and a combination of 3812 quadrilateral and triangular elements was used to discretize the embankment (Figure 5.3). A 1 m global mesh was applied to the whole domain with 0.1 m refinement along the flux boundary at the ground surface. A no flow boundary condition was applied at the pavement, left side, and bottom of the embankment. At right hand side the groundwater table was assumed at 4 m below the embankment surface, and section above the groundwater table was considered as no flow. A flux boundary comprising precipitation records was applied at the soil-atmospheric interface. Nonponding boundary condition was applied in order to prevent excessive accumulation of rainfall on the slope surface. As mentioned earlier, for these simulations large quantities of water flux was applied in a period of 1 to 24 hour, and considering that the maximum evaporation over a 24 hr. period is only a few mm, evaporation was not considered. This approach is similar to one that has been used by Robinson et al. (2017). Three PWP recording sections at the middle, top half, and bottom half of the slope were used to record the temporal variations of PWPs. A wet initial condition was selected from the thirty years of initial model since the wet antecedent condition has a higher probability of creating critical condition for the short term slope stability analysis (Pk and Beddoe 2016). This hydrological model was simulated for the short term (1 to 24 hour) design storms of six return periods, and two types of embankments (Sand & Silt).

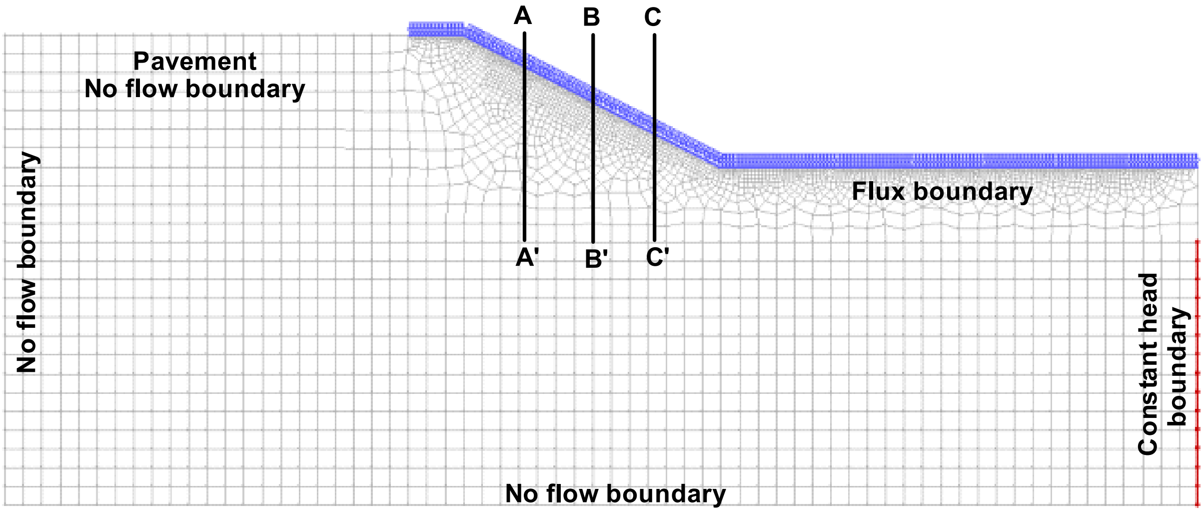

Figure 5.3 FE mesh, boundary conditions, and three PWPs recording sections of the SEEP/W model

5.2 Geotechnical Modeling

5.2.1 Selection of Geotechnical Software

In order to evaluate the effects of climate change on the stability of soil embankments a slope stability software was required. One of the most important criteria for the software selection was its ability to take into consideration the unsaturated shear strength of the soil and estimate factor of safety for unsaturated conditions. This was essential because the climate variables are expected to have a direct influence on soil suction and associated shear strength. The limit equilibrium software, SLOPE/W takes into consideration the unsaturated shear strength of the soil and can estimate factor of safety for unsaturated conditions. It offers two ways to model unsaturated shear strength: 1 – use of Fredlund et al. (1978) model with constant ϕ^b parameter, 2 – use of Vanapalli et al. (1996) model with volumetric water content function. In addition, SLOPE/W integrates seamlessly with SEEP/W, and also has the capability to import pore pressures calculated using the HYDRUS-2D. Therefore, SLOPE/W was selected as the slope stability software for assessing the stability of the soil embankment for the both sets of design climates.

5.2.2 Slope stability model development

Slope stability analyses of both design climates and embankments were performed using SLOPE/W. The slope stability models require the PWPs calculated in the hydrological models as input, and calculate the stability of the embankments using effective shear strength parameters. The PWPs calculated in the hydrological models were transferred using similar grid technique. Therefore, exactly same embankment profile as shown in Figure 4.1, was used for the slope stability model. The strength of the fill and subsoil materials was modelled using the Mohr-Coulomb model. The effective shear strength parameters used to develop the Mohr-Coulomb models are shown in Table 4.1. The suction strength of the unsaturated soil was estimated using the Vanapalli et al. (1996) model. The calculated saturated and unsaturated shear strengths were used to calculate the stability of embankments using the Morgenstern-Price method. This method considers both the force and moment equilibriums of static, and widely used in the slope stability analysis (Fredlund and Krahn 1977).

5.3 Coupling of Hydrological and Geotechnical models

The SEEP/W and SLOPE/W are the two modules of a software suite called GeoStudio (Geo-Slope International Ltd. 2017) . These two modules can be easily coupled, by assigning the hydrological models of the embankment in SEEP/W as the parent models of the slope stability models in SLOPE/W. This insures that not only the geometry of the two models is the same but also that the pore pressures at any time from the hydrological model output are automatically available in SLOPE/W. This coupling ensures the continuous calculation of factor of safety of slopes for each time step for which pore pressure distribution is available from the parent analysis in SEEP/W.

HYDRUS-2D and SLOPE/W cannot be coupled in the same manner as described above. The PWPs at a particular time step can be easily extracted from the HYDRUS-2D using the graphical user interface (GUI). This extracted PWPs can then be exported in to the slope model using the spatial function of SLOPE/W. This procedure needs to be repeated for all the times steps for which slope stability assessments need to be made. The procedure can be quite time consuming. For example, if slope stability assessments need to be done for every day of the climate dataset over a 30 years of period, 7320 such extractions would have to be made and same number of slope models would need to be made. Therefore, it is important to identify the critical time step when the factor of safety of slopes would be at its lowest value. To accomplish this, temporal relationship between the boundary fluxes (*BF*s), cumulative storage and factor of safety of slopes was studied. Cumulative storage refers to the total amount of water in the domain. At any time step, it is estimated by adding or subtracting the net *BF* from the cumulative storage from the previous time step. A positive net *BF* indicates that the system gains water while a negative net *BF* means water leaves the system. A plot of cumulative net *BF* and cumulative storage with times is shown in Figure 5.4a. In Figure 5.4a, it can be observed that the cumulative storage follows the trend of cumulative net *BF*. It increases when the net *BF* is positive, and decreases when the net *BF* is negative. Figure 5.4b shows cumulative storage versus factor of safety plot. It can be seen in Figure 5.4b that the factor of safety of slopes inversely related with the cumulative storage of the system. It increases when the cumulative storage decreases with the negative net *BF*, and opposite results can be observed when the cumulative storage increases with positive net *BF*. Therefore, based on the inverse relationship between the cumulative storage and slopes FOS, the critical time step can be selected from the highest cumulative storage point.

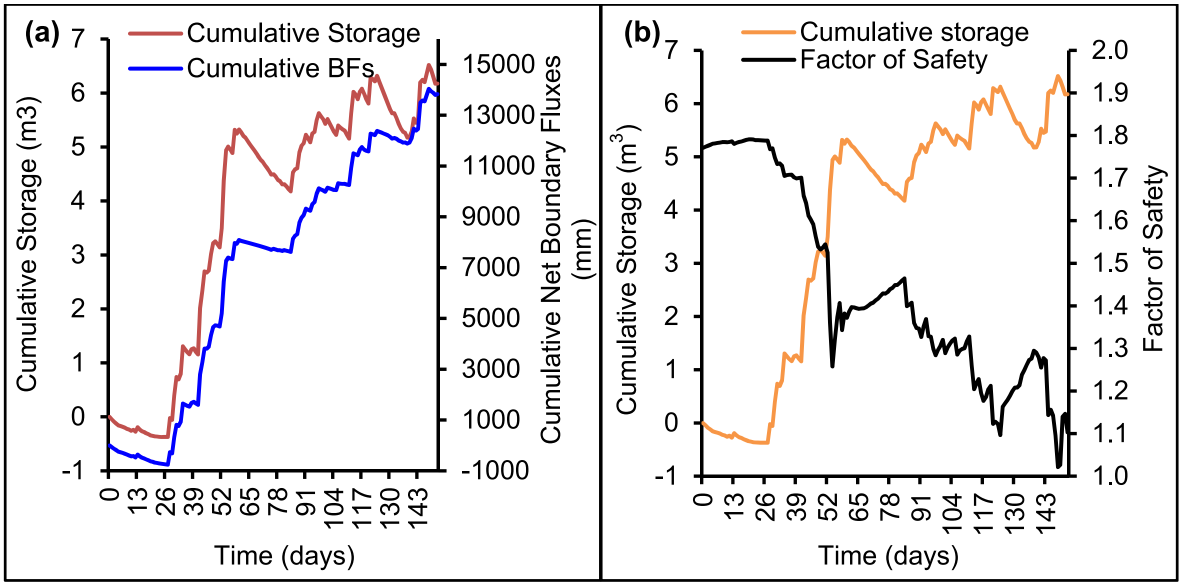

Figure 5.4 Coupling hydrological and slope stability models (a) Cumulative net boundary fluxes versus cumulative storage (b) cumulative storage versus factor of safety

5.4 Modeling the Effect of Pavement on the Embankment Surface

Pavement surface is usually considered impermeable, and therefore a no flow boundary condition can be used to model the pavement in numerical models. The accumulated water at the paved surface can be modeled as runoff, and can be distributed over the permeable portion of the embankments adjacent to the impermeable pavement. This is essential for accurate assessment of water balance at the ground surface. This technique of simulating impervious materials in hydrological models has been successfully applied (e.g., Coutinho et al. 2016). The intensity of the rainfall imposed on the soil embankments (I_{SE}) is increased in comparison to the actual rainfall intensity (I_{rain}), and can be derived from the ratio of total length of embankment (*TLE*) and total length of soil embankment (*TLSE*) as follows:

$$I_{SE} = I_{rain} \frac{TLE}{TLSE} \tag{5.1}$$

In this study, the effect of including pavement within the model embankment was investigated by simulating a hypothetical homogeneous sand embankment for historical 30 years Toronto climate. The embankment was simulated for two boundary conditions: with pavement, and without pavement. The 30 years water balance at the ground surface for these two boundary conditions is plotted in Figure 5.5. In this figure, it can be seen that the cumulative values of *NI* and *AE* are significantly different for same *P* and *PE* values. It can also be observed that no *RO* was generated for the permeable part of the embankment. The results indicate that higher quantity of water makes its way into the domain (larger *NI*) if the pavement is simulated. This is counter intuitive as one would expect that model with no pavement has larger permeable surface and hence should result in larger *NI* values. Larger *NI* value for pavement simulation can be explained in terms of precipitation intensity. When pavement is simulated, *RO* from the pavements results in higher precipitation intensity over the permeable section of the embankment. This implies that in a given time period there is more water availability but same evaporative demand (*PE*) resulting in lower *AE* and higher *NI* values. These results illustrate the importance of simulating pavement in an embankment, and possible errors if we neglect pavement effects in embankments.

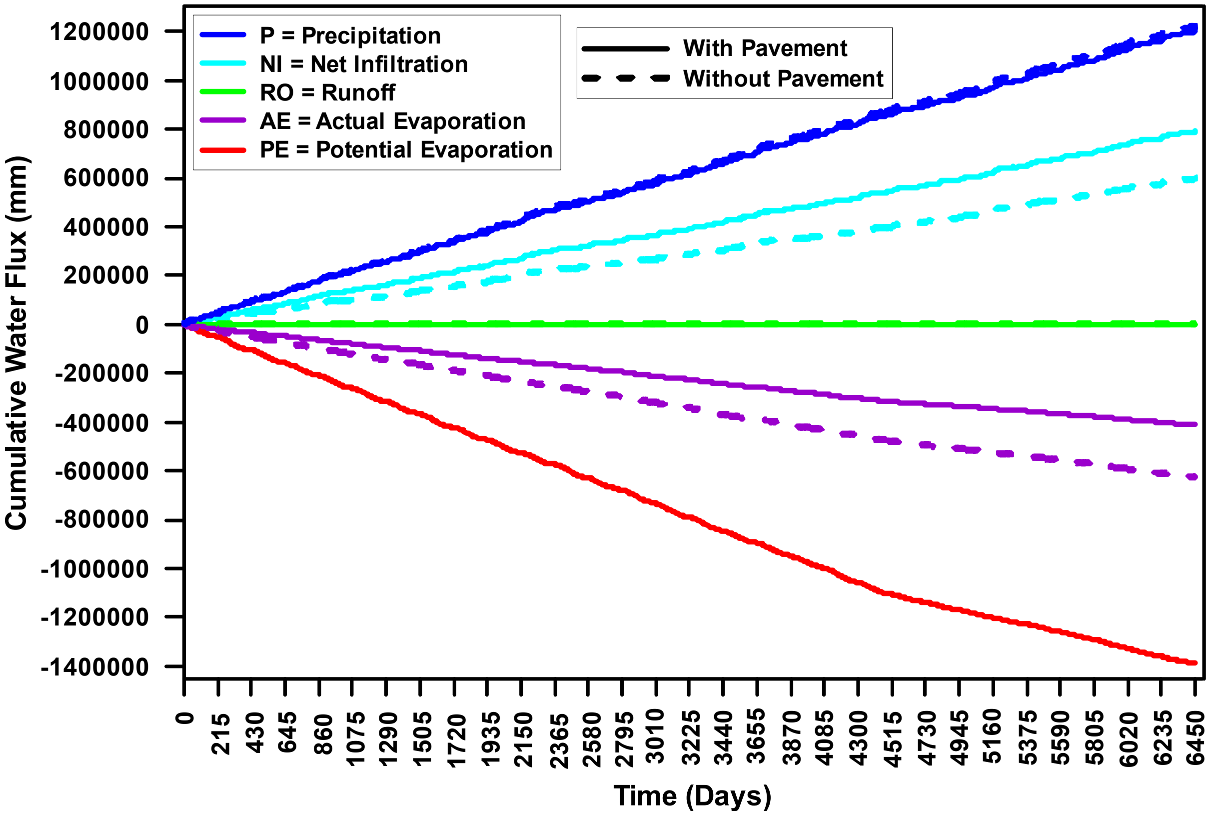

Figure 5.5 Ground surface moisture balance for 30 years of city of Toronto climate with and without pavement within the embankment

Chapter 6. Results and Discussions

6.1 Introduction

Two types of fill materials, and two sets of design climates were selected to investigate the effects of climate change on the stability of soil embankments. The fill materials selected for the embankment were sand and silt, and are therefore called the sand embankment and silt embankment respectively. Corresponding to the two different design climates, the results are presented into two separate sections. Each of the section contains two subsections one for each embankment type. Two design climates and two embankment types together form total four combinations. A flow chart showing all the combinations is presented in Figure 6.1.

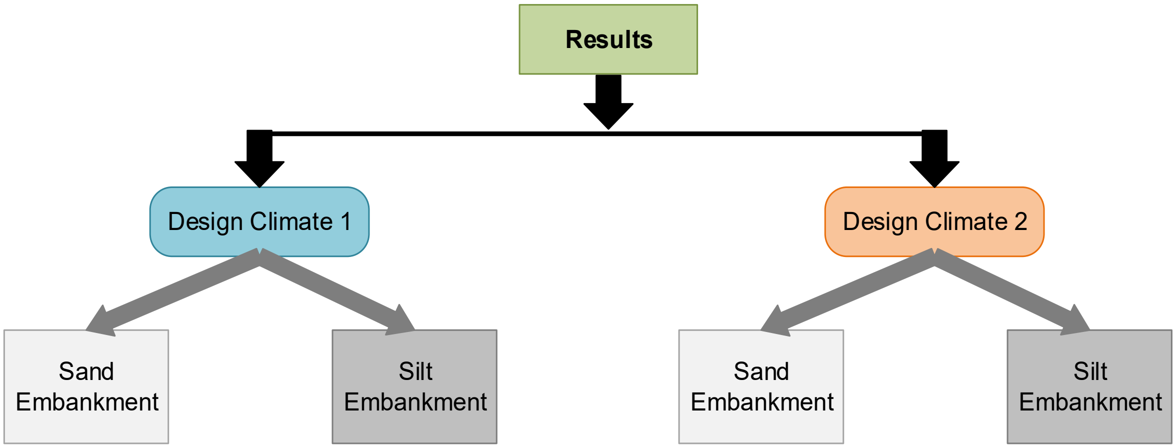

Figure 6.1 Flow chart of the results presented in this chapter

6.1.1 Numerical model simulations for Design Climate 1

In the first set of numerical model simulations run for Design Climate 1 (DC1), there were two soil types, 3 climate ensembles, and 3 temporal resolutions of precipitation resulting in a total of 18 simulations (Table 6.1).

Table 6.1 Numerical simulations run for Design Climate 1

No.	Embankment Fill	Climate Scenario	Temporal Resolution of Precipitation (hr.)
1	Sand	Baseline	12
2	Sand	Baseline	2
3	Sand	Baseline	1
4	Sand	Future 1	12
5	Sand	Future 1	2
6	Sand	Future 1	1
7	Sand	Future 2	12
8	Sand	Future 2	2
9	Sand	Future 2	1
10	Silt	Baseline	12
11	Silt	Baseline	2
12	Silt	Baseline	1
13	Silt	Future 1	12
14	Silt	Future 1	2
15	Silt	Future 1	1
16	Silt	Future 2	12
17	Silt	Future 2	2
18	Silt	Future 2	1

DC1 contains 1 baseline and 2 future climate ensembles (CE # 1, 23, 37 in Figure 3.12). The first future climate ensemble (FC1) was selected based on analysis of I_m (CE # 23 in Figure 3.16), and the second future climate ensemble (FC2) was selected based on analysis of annual precipitation (CE # 37 in Figure 3.13). Each of the climate ensemble contains *P* and *PE* data for a 30-year period. To address the effects of temporal resolution of precipitation, the daily precipitation was distributed over the 12, 2, and 1 hr. periods by comparing the historical extreme precipitation records with the IDF curves (Figure 3.23). It was found that the 12, 2, and 1 hr. resolutions of precipitation represents regular, 10-25, and 50-100 year return periods of extreme precipitation events respectively.

6.1.2 Numerical model simulations for Design Climate 2

The second set of design climate (DC2) contains two sets of IDF curves, each with six return periods (2, 5, 10, 25, 50, and 100 yr.). One set of IDF curves is for the baseline climate (BC), and the other for the future climate (FC). The critical duration of the IDF curves was selected based on the hydraulic properties of the fill materials. It was observed that the high permeable sand embankment was susceptible to short and intense precipitation events, while the prolonged precipitation events made the low permeable silt embankment vulnerable. Therefore, a duration of 1-hour was selected for the sand embankment, and 24-hour for the silt embankment. In total, two climate scenarios, for two embankments, each with six return periods result in a total of 24 simulations for DC2 (Table 6.2).

Table 6.2 Numerical simulations run for Design Climate 2

No.	Embankment Fill	Climate Scenario	Return Period (yr.)	Duration (hr.)
1	Sand	Baseline	2	1
2	Sand	Baseline	5	1
3	Sand	Baseline	10	1
4	Sand	Baseline	25	1
5	Sand	Baseline	50	1
6	Sand	Baseline	100	1
7	Sand	Future	2	1
8	Sand	Future	5	1
9	Sand	Future	10	1
10	Sand	Future	25	1
11	Sand	Future	50	1
12	Sand	Future	100	1
13	Silt	Baseline	2	24
14	Silt	Baseline	5	24
15	Silt	Baseline	10	24
16	Silt	Baseline	25	24
17	Silt	Baseline	50	24
18	Silt	Baseline	100	24
19	Silt	Future	2	24
20	Silt	Future	5	24
21	Silt	Future	10	24
22	Silt	Future	25	24
23	Silt	Future	50	24
24	Silt	Future	100	24

6.2 Design Climate 1

The three climate ensembles in DC1 were applied to the sand and silt embankments and numerical modeling simulations were run to calculate the embankments stability for each ensemble. The results are presented in the following sections for the sand and silt embankments respectively.

6.2.1 Sand embankment

The results of the sand embankment analyses are presented in three sections. The water balance results are presented at the beginning to first understand the water movement at the ground surface. The effects of changes in water balance on the PWPs of embankments are then presented. Finally, the stability results for the baseline and future climate ensembles are presented.

6.2.1.1 Water balance at the ground surface

The water balance at the ground surface can be useful in understanding water movement in embankments and associated factor of safety. To investigate climate change effects on water balance of embankments, the simulations run with regular precipitation of 12-hour resolution were selected. Interpretation of the 30 years of cumulative water balance can be cumbersome, and as such the wet, average, and dry years were selected to investigate the water balance in the wet, average, and dry climates.

The water balance for the wet, average, and dry years is shown in Figure 6.2a, b, and c respectively. It can be seen in Figure 6.2 that the cumulative *RO* is zero for all the three years. The highest intensity of the imposed precipitation is 12.5 mm/hr. which is much lower than the saturated hydraulic conductivity of sand (146 mm/hr.). Therefore, the precipitation intensity is less than the infiltration capacity of the soil and no *RO* is generated.

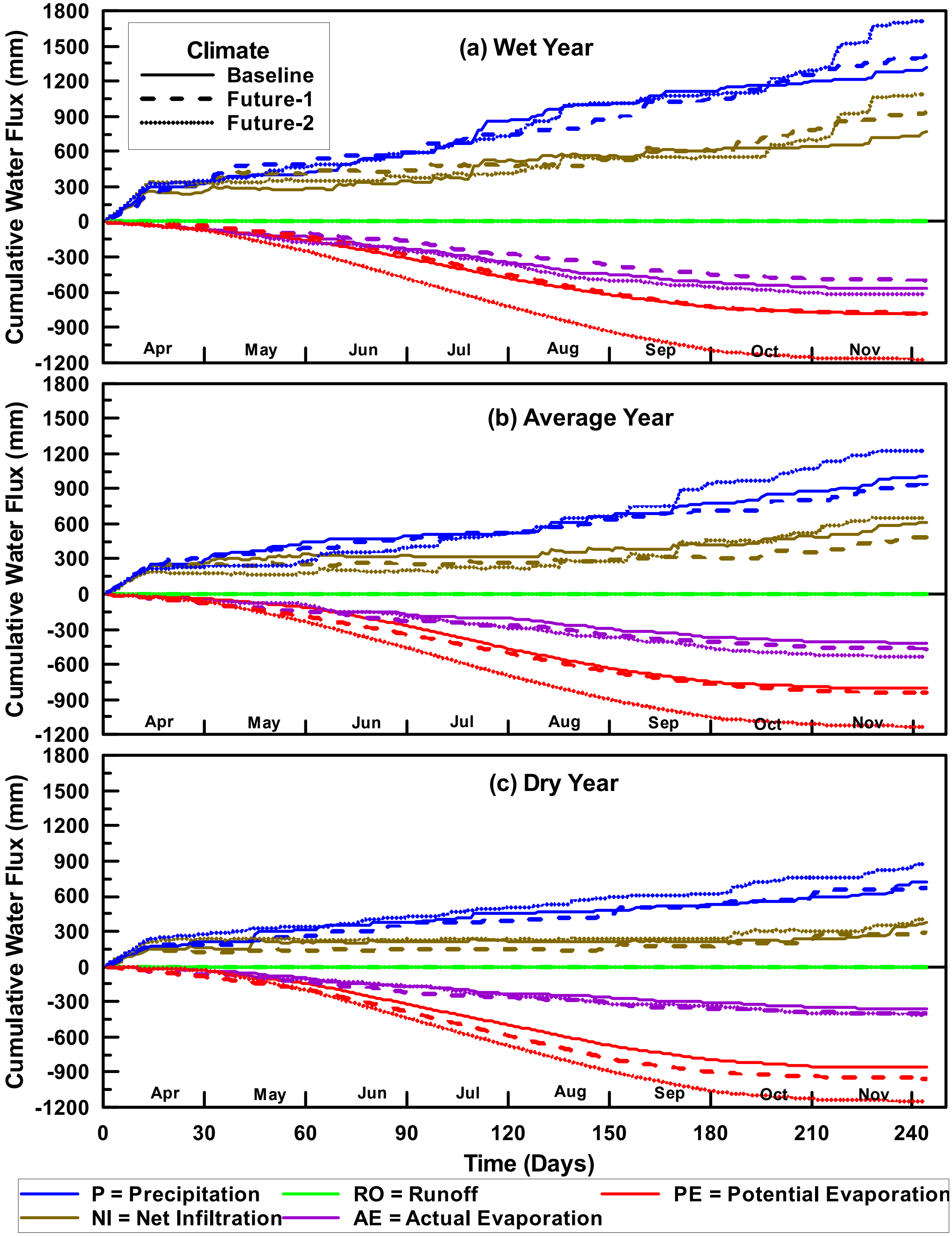

Figure 6.2 Water balance at the ground surface of the sand embankment in the (a) wet year, (b) average year, and (c) dry year

The cumulative precipitation for all the three climate ensembles is the highest for the wet year, followed by the average then dry years. Similarly, the difference in cumulative precipitation between the three ensembles is greatest in the wet year, with decreasing differences in the average year and dry year respectively. In contrast, potential evaporation does not follow the same pattern. The *PE* remains relatively constant in the wet, average and dry years. The highest cumulative *PE* is observed for the FC2, while the BC and FC1 follow similar results.

Net infiltration is the actual amount of water that changes the storage within the embankment, and has potential to affect the PWPs and stability of embankments. The amount of net infiltration primarily depends upon precipitation, *RO*, and *AE*. It can be observed in Figure 6.2 that the *RO* is zero for all simulations. The AE does not show any considerable difference between the climate ensembles even though the FC2 has much higher *PE*. The *AE* is a combined product of available soil moisture and *PE*. The low water retention, and high drainage characteristic of sand do not allow much water to remain near the ground surface for evaporation. Therefore, despite different *PE* values, the *AE* values for different climate ensembles remain similar. However, the *AE* does show variations between the wet, average, and dry years within a climate ensemble. For example, the cumulative *AE* for the FC2 in the wet, average, and dry years are 650 mm, 550 mm, and 400 mm respectively (Figure 6.2a-c). Similar observation can be made for the BC and FC1. Although the sand embankment can drain the infiltrated water quickly, the increased amount of precipitation and increased number of precipitation days in the wet year generate higher *AE*.

The cumulative net infiltration in the sand embankment follows the cumulative precipitation trend. It can be seen in Figure 6.2a that the cumulative *NI* in the wet year for the BC, FC1, and FC2 are 770, 932, and 1087 mm respectively. The FC1 and FC2 show an increase of 162 and 317 mm of *NI* respectively. These increases in *NI* during the wet years could affect the future stability of the sand embankment. In the average and dry years, the cumulative *NI* also follows the cumulative precipitation trend. The average year shown in Figure 6.2b shows that the cumulative *NI* for the BC, FC1, and FC2 are 614, 484, and 648 mm respectively. This means that there was a 130 mm decrease in *NI* for FC1. In contrast, FC2 shows a slight increase in NI. Similar observations can be made for the dry year also (Figure 6.2c). This indicates that in the future, the sand embankment could experience moisture deficit in the dry as well as average years. It also indicates that a significant increase in *NI* can be observed in a wet year. While both of these scenarios can have detrimental effects on the stability of embankments, this study focused on the wet year only to investigate the effects of temporal resolutions of precipitation.

6.2.1.2 Effects of temporal resolution of precipitation

The effects of the temporal resolutions of precipitation were investigated by distributing the daily precipitation over 12, 2, and 1 hours respectively. The water balance at the ground surface was calculated for each temporal resolution, and the results for the BC, FC1, and FC2 are presented in Figure 6.3. It was observed that the high permeable sand embankment does not generate any surface *RO* and thereby it is not included in Figure 6.3. The cumulative *AE* and *NI* also do not show considerable variation between the 12, 2, and 1 hr. precipitation events. The low retention, and high drainage characteristics of sand generate similar amounts of cumulative *AE*, and *NI*. However, the 12 hr. precipitation shows slightly higher estimation of *AE*, and lower estimation of *NI*. As the intensity of precipitation increases with higher resolutions, there is more availability of water in shorter period of time. However, the *PE* distribution does not change over the diurnal cycle resulting in lower estimation of *AE*. On the other hand, the distribution of the precipitation over the 12-hour period of time allows water to remain at least for 12 hours at the ground surface which increases the *AE*, and conversely decreases *NI*.

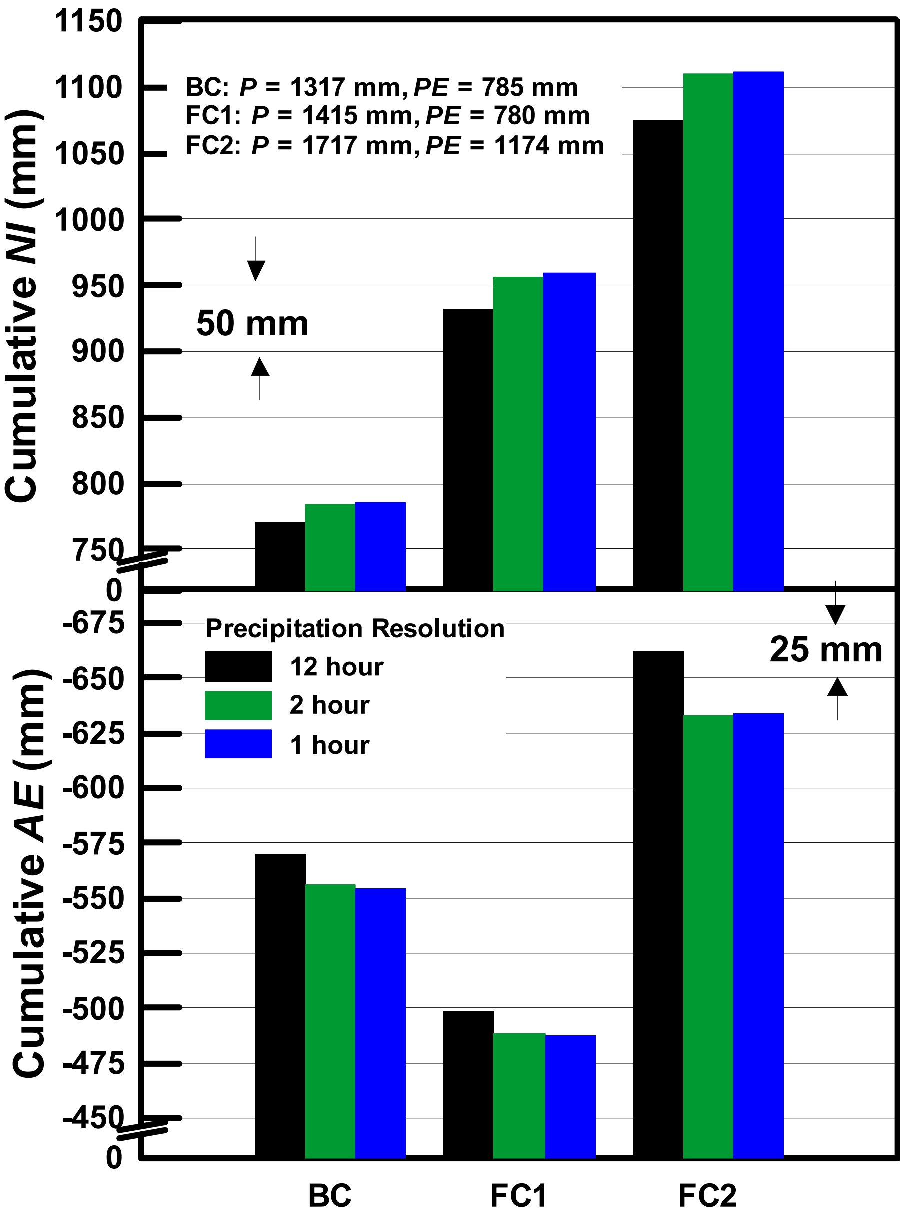

Figure 6.3 Cumulative *NI* and *AE* for the 12, 2, and 1 hour resolutions of precipitation

The temporal resolution of precipitation data does not show any considerable impact on water balance, and almost similar amount of water infiltrates for all the three resolutions. As such the total amount of water that enters into the embankment over the 1 hr. period of time is almost similar to the amount of water that enters over the 2 and 12 hr. period of times. Therefore, it is anticipated that the highest intense 1-hour precipitation has the highest potential to develop excess PWPs at the end of the precipitation events. For further investigations, the PWPs and stability of the sand embankment were calculated for the three temporal resolutions, and the results are presented in the following sections.

6.2.1.3 Pore-water pressures distribution

Three vertical sections of the soil embankment were chosen for detailed analysis of spatial PWP distribution. The sections are located in the sloping portion of the embankment and their exact location is shown in Figure 6.4a. In Chapter 5, It was shown (Figure 5.4) that the FOS of embankments is a function of the total amount of water that is stored within the embankment. Based on this relationship, the wettest day was identified from the 30 years of storage record. The PWPs in the embankment on the wettest day at the three sections are also shown in Figure 6.4. The PWPs in the embankment were found to show little variation beyond a depth of 2m, and as such the focus of Figure 6.4 is the top 2 m of the sand embankment. The overall PWPs profiles presented in Figure 6.4 are similar for all three sections of the embankment. However, what does change is the profiles when comparing the temporal resolutions at each vertical section. For example, in Figure 6.4b, the PWPs profile for the 12-hour precipitation shows that the BC, FC1 and FC2 are consistent at -2 kPa to -4 kPa. In comparison, the 2 hr. and 1 hr. profiles show lower depth of influence, but higher difference in PWPs ranging from 0 kPa to -9 kPa. Similar results are found in the vertical sections B-B' and C-C' (Figures 6.4c and 6.4d respectively). There are also differences in the PWP profiles when comparing BC to the FCs. It can be observed in Figure 6.4 that both FC ensembles show an increase in PWPs and depth of influence compared with the BC. This increase in PWPs from the BC to the FCs has the potential to affect the future stability of the sand embankment.

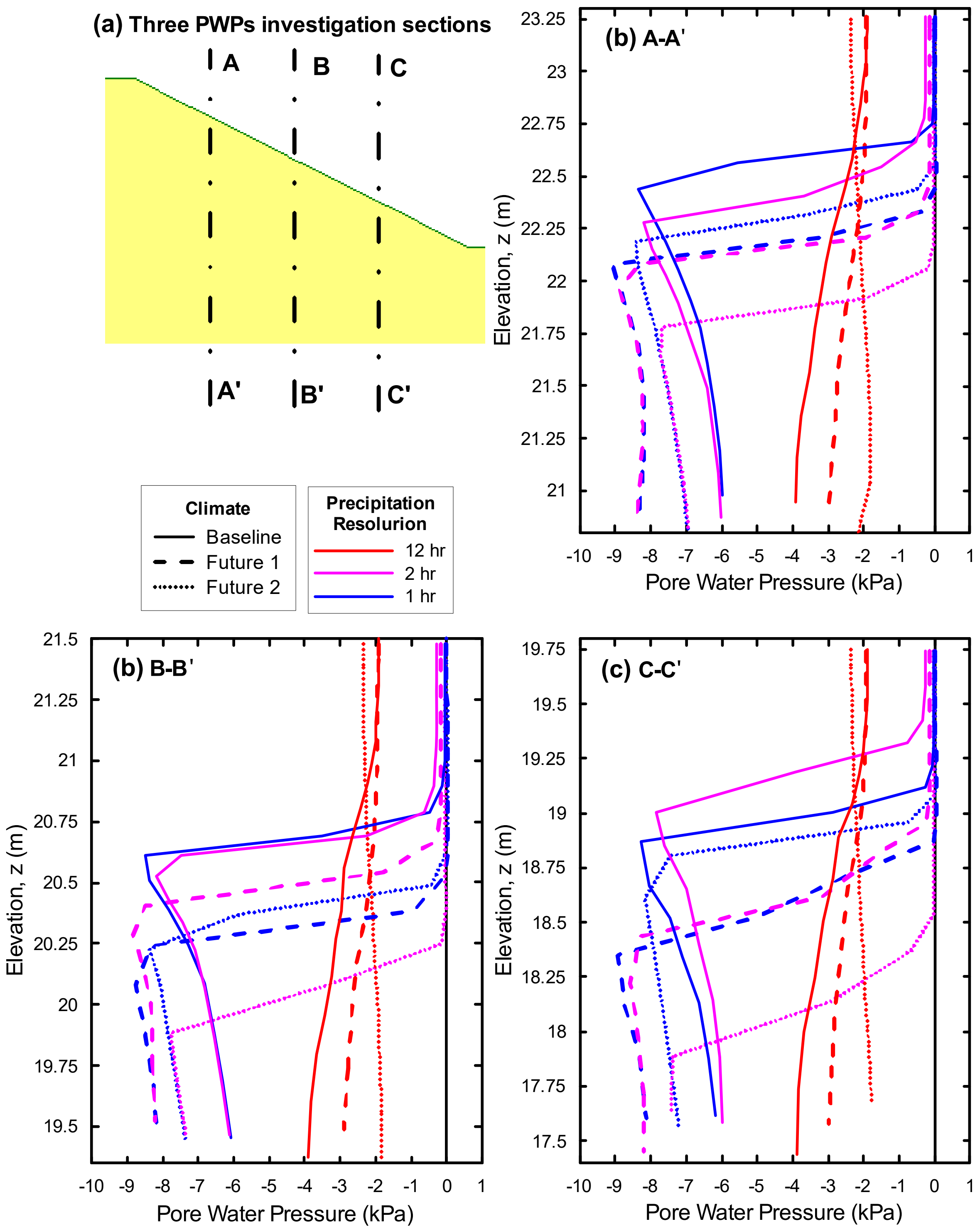

Figure 6.4 (a) Initial PWPs at three vertical sections, (b), (c), and (d) PWPs distributions for the three climate ensembles, and three temporal resolutions of precipitation at the top, middle, and bottom sections of the sand embankment

6.2.1.4 Factor of safety

Wettest day for three climate ensembles and three temporal resolutions of precipitation together form a total of nine scenarios for which embankment stability simulations were run (Table 6.1). The critical factor of safety for each of these simulations along with pore-water pressures distribution and critical slip surfaces are presented in Figure 6.5. The FOS plots for the 12, 2, and 1 hr. precipitation are presented in three columns, marked a, b, and c respectively. The three rows in Figure 6.5 represent three climate ensembles for the BC, FC1 and FC2. It can be seen in Figure 6.5 that the critical FOS decreases from the left to the right of the rows with the decrease in the resolutions of precipitation from 12 to 1 hour which agrees with the water balance and PWP distribution results presented in Figure 6.3 and 6.4 respectively. It also can be observed in Figure 6.5 that the critical slip surfaces for the low intense 12 hr. precipitation are deep, while the intense precipitation of 2 and 1 hour resolutions show more shallow critical slip surfaces. The FOS values are consistent with the observations in Figure 6.4, where surface saturation can be observed for higher precipitation intensity, resulting in shallower slip surfaces.

A comparison in the FOS between the baseline and future climates show that both of the FCs calculate lower FOS for all the three different precipitation resolutions. The lowest FOS for the BC is 1.27 for the 1-hour precipitation, while the lowest FOS for both of the FCs is 1.24 for the 1-hour precipitations. The low retention and high drainage characteristics of the sand material discourage generating excess PWPs, and therefore, the FOS values between the baseline and future climates are similar despite a wide variation of observed *NI* in Figure 6.2.

It should be noted that FC1 was selected based on the I_m method, whereas FC2 was selected as the scenario with the highest annual *P* and *PE* (which results in an I_m lower than FC1). The results in Figure 5.6 show that the FOS for the FC1 is higher than the FOS of FC2. Therefore, geotechnical engineers should exercise caution when using the annual moisture index approach, as it could result in over estimating the FOS of their sand embankment.

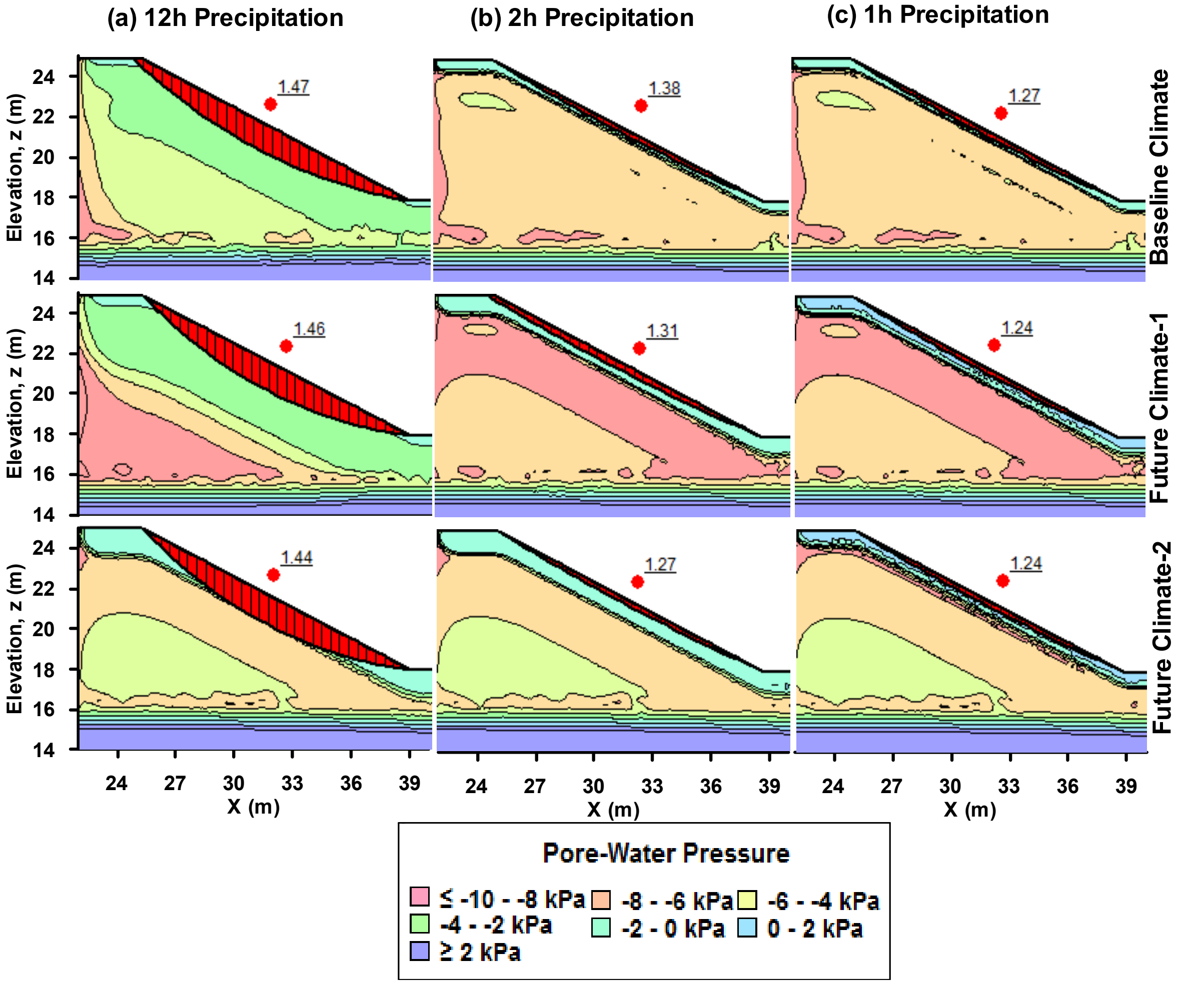

Figure 6.5 FOS plots with PWPs distributions of the sand embankment for the three climate ensembles, and three temporal resolutions of precipitation

6.2.2 Silt embankment

The stability of the silt embankment was also investigated using the same procedure outlined in the sand embankment section, and the results are presented sequentially in the following sections.

6.2.2.1 Water balance at the ground surface

The water balance at the ground surface of the silt embankment was calculated for the wet, average, and dry years using the design climate of 12-hour resolution data sets. The results f are presented in Figures 6.6a, 6.6b, and 6.6c for the wet, average, and dry years respectively. It can be seen in Figure 6.6 that the silt embankment generates *RO*, especially during the wet year in FC2. The saturated hydraulic conductivity of the silt material is 4.5 mm/hr. which is less than the highest precipitation intensity of 12.5 mm/hr. Therefore, the low permeable silt embankment generates *RO* for the regular precipitation of 12 hr. resolution. This is in contrast to the sand embankment where no *RO* was generated under the same *P* & *PE* inputs.

The higher retention and lower drainage characteristics of silt allowed more water to remain in soil layers near the ground surface for longer period of time, this results in higher *AE* when compared to the sand embankment. The *AE* of the silt embankment is highest in the wet year (Figure 6.6), followed by average then dry years. This might seem counter intuitive, as the evaporative demand (*PE*) for average and dry years is slightly higher than the wet year. However, it should be noted that *AE* not only depends upon the evaporative demand but also the availability of water in the near surface layers. As the in all instance, more water is available in wetter years (higher precipitation quantities), therefore *AE* is higher. This observation is consistent with the observations of Bashir et al. (2015). It should also be noted that in comparison to the sand embankment, the difference in *AE* between the BC and FC ensembles are higher for the silt embankment. This can be attributed to enhanced evaporation in silts due to higher retention and lower drainage characteristics in comparison to sands.

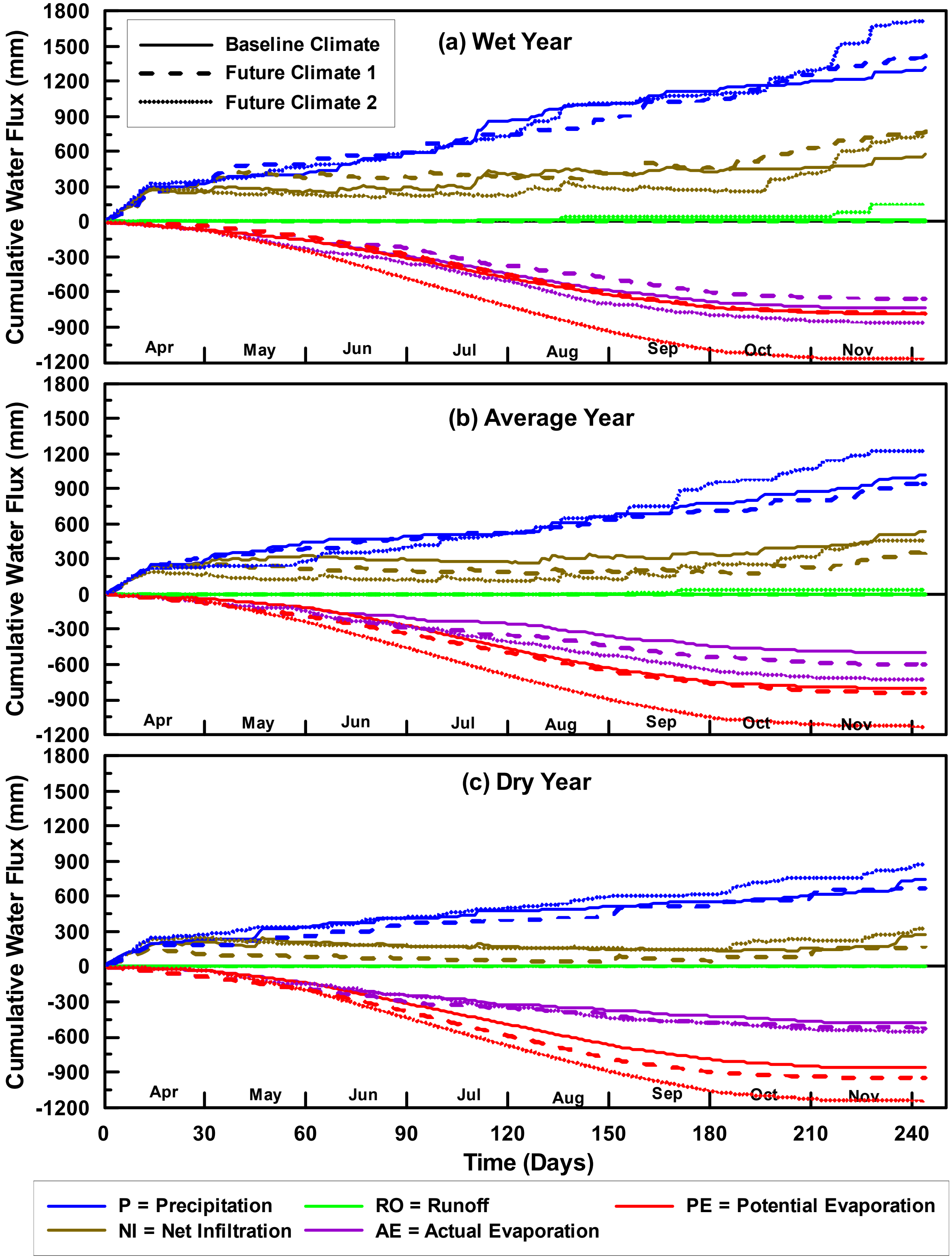

Figure 6.6 Water balance at the ground surface of the silt embankment for the three climate ensembles in the (a) wet year, (b) average year, and (c) dry year

As the silt embankment generates *RO* during intense precipitation events, the cumulative *NI* does not necessarily follow the cumulative precipitation pattern. For wet years water balance, the cumulative *NI* value for FC2 is slightly lower than the FC1 even though the FC2 has considerably higher cumulative precipitation (Figure 6.6a). The intense precipitation in FC2 generates 150 mm of cumulative *RO*, while the cumulative *RO* for FC1 and BC are negligible. Moreover, as also seen in Figure 6.6a, FC2 has higher cumulative *AE* than the BC and FC1 (861, 738, and 656 respectively). Therefore, lower *AE*, and negligible *RO* for FC1 results in slightly higher quantity of *NI*.

It also can be seen in Figure 6.6a that the both FC ensembles generate a significantly higher *NI* comparing with the BC. The cumulative *NI* at the end of the wet year for the BC, FC1, and FC2 are 573, 771, and 726 mm respectively. That means an increase of annual cumulative *NI* of 35% and 27% is observed for the FC1 and FC2 respectively. This increase in annual *NI* has significant potential to affect the future stability of the silt embankment.

Future Climate 2 generates *RO* and the highest *AE*, resulting in lowest *NI* for the average year climate (Figure 6.6b). The BC, which has no RO and the lowest *AE* results in highest *NI*. It can also be observed that for average year climatic conditions, the total cumulative *NI* for the BC, FC1, and FC2 are 530, 349, and 452 mm respectively. This leads one to conclude that for average climatic conditions, both future climatic ensembles show decreases in cumulative *NI*, indicating that the silt embankment could experience moisture deficits. This observation highlights the fact that quantity of water that enters the embankment is not simple a function of the total quantity of precipitation but also the precipitation intensity, and soil hydraulic properties.

In the dry year (Figure 6.6c), there is no *RO*, and *AE* values are almost similar between the baseline and future climate ensembles, and thereby the cumulative *NI* follows the cumulative precipitation trend. The observed cumulative *NI* at the end of the dry year are 275, 165, and 322 mm for the BC, FC1, and FC2 respectively.

The water balance at the ground surface shows that in FC ensembles, a significantly large amount of water could infiltrate into the silt embankment in the wet year. It should be noted that in the average year the embankment could experience moisture deficit, however in terms of slope stability larger *NI* values are more significance.

6.2.2.2 Effects of temporal resolution of precipitation

To study the effects of the temporal resolutions of precipitation, the daily precipitation was distributed over 12, 2, and 1 hr. periods, which increases the precipitation intensity. The water balance at the ground surface for the wet year was calculated for the three temporal resolutions of precipitation. The water balance results for the BC, FC1, and FC2 are presented in the Figure 6.7a, 6.7b, and 6.7c respectively. It can be seen in Figure 6.7 that the precipitation events occurring over a 12-hour period result in highest *AE* values followed by the 2, and 1-hour precipitation. However, the differences in *AE* between the 12, 2, and 1 hr. precipitation are not significant. The high retention and low drainage characteristics of the silt material holds water in upper soil layers for longer times, resulting in similar amount of *AE* for the three different precipitation intensities. However, the temporal resolutions of precipitation do show a significant impact on *RO* generation in the silt embankment. It can be observed in Figure 6.7 that the *RO* generation increases with increase in precipitation intensity resulting in corresponding decrease in *NI* values. Therefore, the *NI* is the highest for the 12-hour precipitation, and lowest for the 1-hour precipitation. The *NI* for the 2-hour precipitation falls between these two. For example, the cumulative *NIs* for the FC2 are 726, 470, and 300 mm for the 12, 2, and 1 hr. precipitation respectively. This constitutes to more than 50% reduction in the quantity of water entering the embankment when the precipitation is distributed over 1-

hour period as opposed to 12-hour period. Similar observation can be made for the BC and FC1.

The temporal resolutions of precipitation show a significant impact on the ground surface water balance of the silt embankment. The *NI* into the silt embankment is the highest for the 12-hour resolution followed by the 2 and 1 hour resolutions. Therefore, it can be considered that the precipitation of 12-hour resolution has the highest potential to affect the stability of the silt embankment, whereas the precipitation of 1-hour resolution has the lowest.

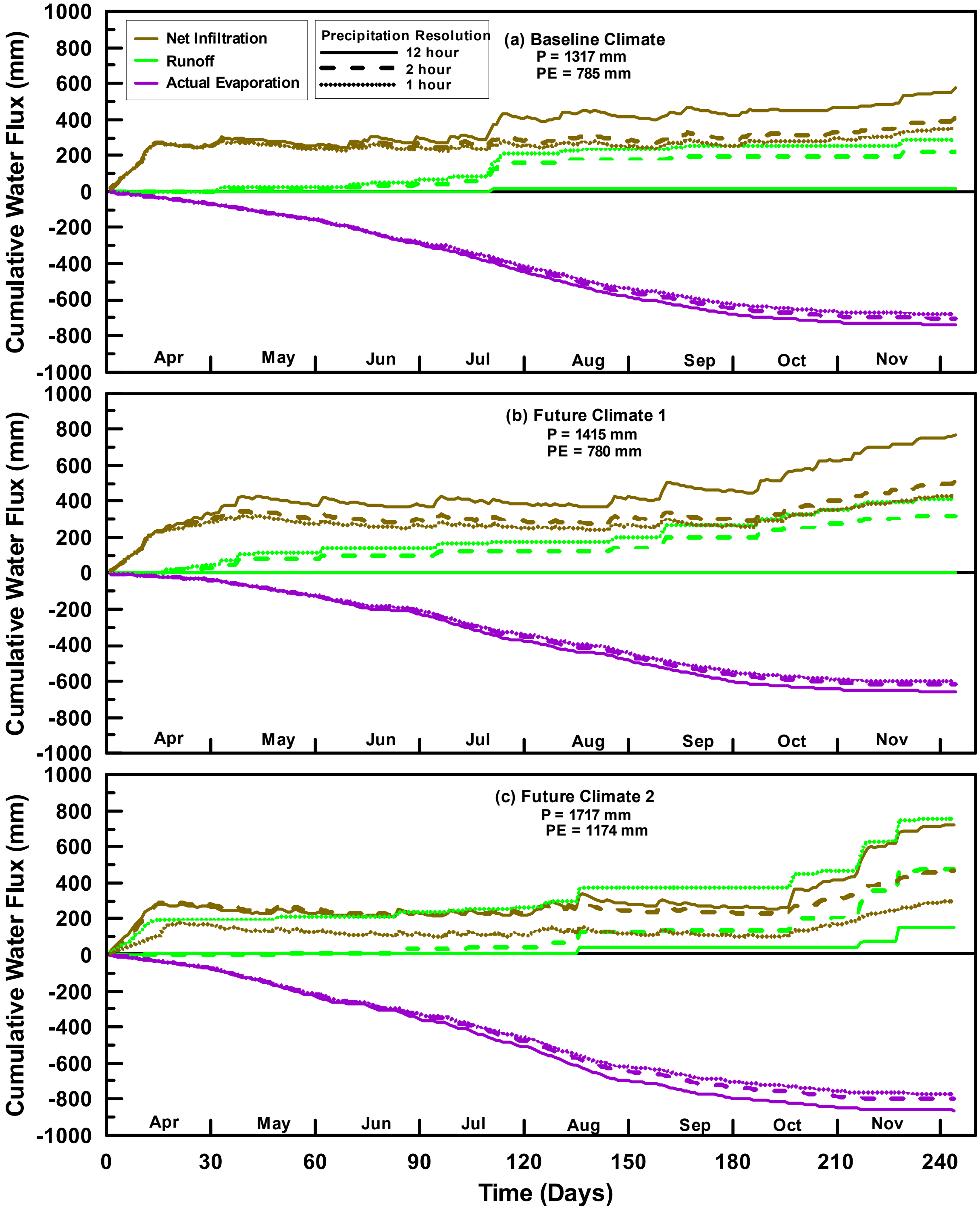

Figure 6.7 Water balances for the three temporal resolutions of precipitation in the (a) baseline climate, (b) Future climate 1, and (c) Future climate 2

6.2.2.3 Pore-water pressures distribution

For the wettest day of each simulation, the PWPs at three cross sections have been plotted in Figure 6.8. The locations of the three PWPs investigation sections are shown in Figure 6.8a (same location as the sand embankment analysis), and the calculated PWPs for the top 2 m are presented in Figure 6.8b, 6.8c, and 6.8d for the sections A-A', B-B', and C-C' respectively.

The comparison between the baseline and future climate ensembles shows that FC2 generates the highest PWPs followed by FC1 and the BC. An exception was observed in the depth of saturation for the 12-hour resolution of FC1. These trends of PWPs profiles are consistent in all three sections of the embankment. However, the PWPs do show variations when comparing them between sections. This is most significant for the precipitation of 12-hour resolution of FC2 (red dotted line). In profile A-A' (Figure 6.8b) the PWPs are approximately zero. As we move down the slope to profile B-B' (Figure 6.8c), then C-C' (Figure 6.8d) the PWPs gradually increase. This clearly emphasizes that the PWPs at the toe of the silt embankment are positive and are near positive at the crest of the slope. These excess PWPs have significant implications on the stability of the embankment.

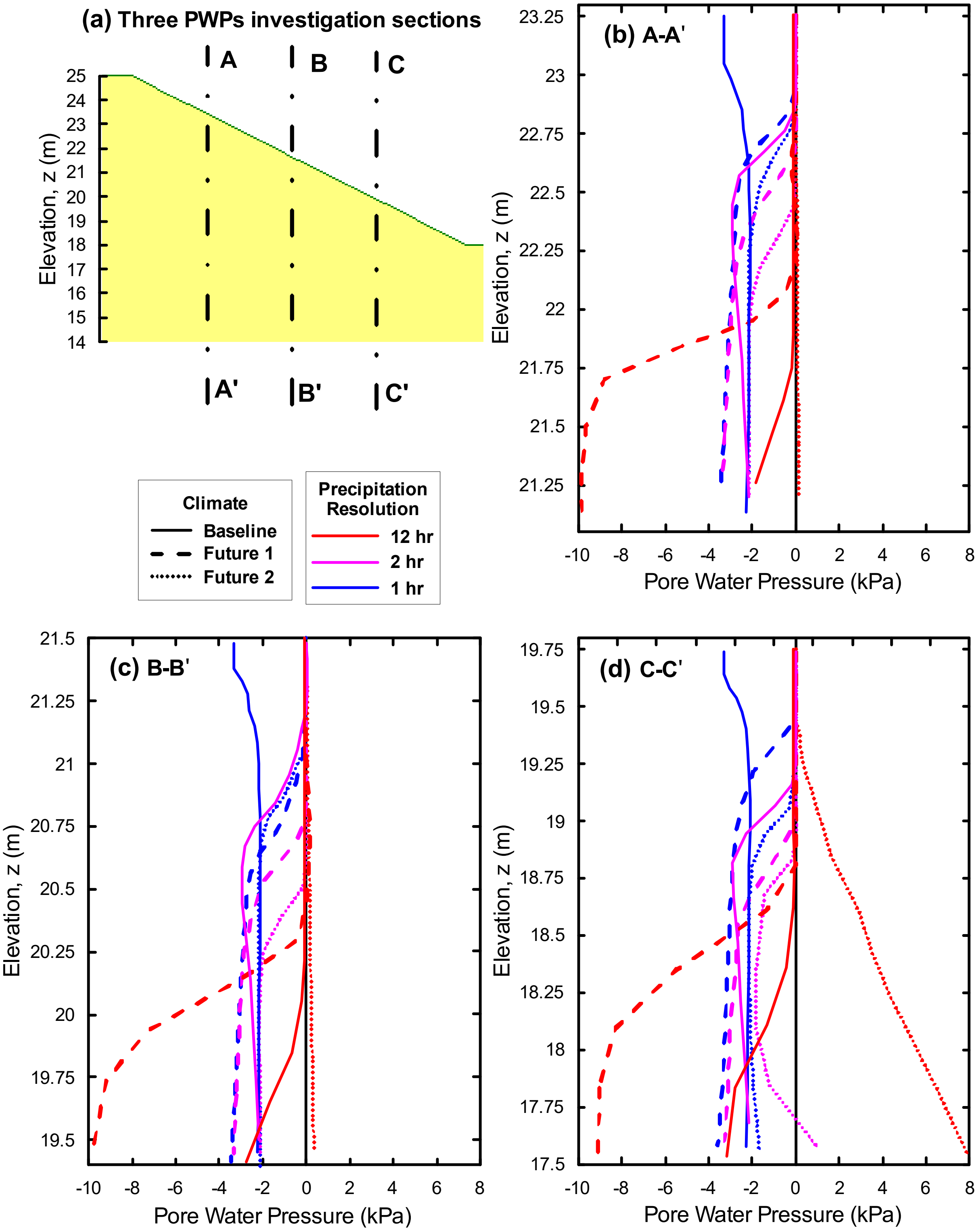

Figure 6.8 (a) Initial PWPs at three vertical sections, (b), (c), and (d) PWPs distributions for the three climate ensembles and three temporal resolutions of precipitation at the A-A′, B-B′, and C-C′ sections respectively

6.2.2.4 Factor of safety

The analysis of water balance at the ground surface, and pore-water pressures at three sections of the silt embankment illustrates that there is potential for significant impacts on the stability of the embankments due to climate change. Specifically, it was found that FC2 has the highest potential to affect the stability of the silt embankment due to generation of excess PWPs. It was also found that the prolonged precipitation events have a greater potential to affect the stability of the silt embankment than the short and intense events. Similar to the stability analysis of sand embankment, the factor of safety of wettest day was calculated for all the three climate ensembles and temporal resolutions of precipitation. The results for the nine simulations are presented in Figure 6.9. The FOS plots for the three temporal resolutions, 12, 2, and 1 hr. are presented in three columns a, b, and c respectively, and the plots for the baseline and future climate ensembles are presented in three different rows.

The FOS calculated for the low intense precipitation of 12-hour resolution (Figure 6.9) was 1.28 for the BC, while the FOS for 2, and 1-hrour resolutions increased to 1.29 and 1.48 respectively. Similar observations can be made for the two FC ensembles. Perhaps counter to first intuition, this shows that an increase in precipitation intensity actually decreases the FOS in a silt embankment, rather than increasing it. However, this observation is consistent with the findings from the water balance at the ground surface and pore water pressure analysis. The water balance at the ground surface indicated less water infiltration for higher precipitation intensities. Pore-water pressure profiles reflected the water balance findings, where it was observed that less water infiltration resulted in dryer profiles. Both of these observations support the FOS findings.

Comparison of FOS results between the future and baseline climate ensembles illustrate that FC2 has the lowest FOS followed by the FC1 and BC. The lowest observed FOS values for the 12-hour resolution of precipitation are 1.28, 1.24, and 1.15 for the BC, FC1, and FC2 respectively. Similar observations can be made for the 2 and 1 hour resolutions.

In addition to global failures, the silt embankment also showed surficial failures and fails for the 12 and 2 hour resolutions of FC2. These can be seen in Figure 6.9 (white line slip surfaces) that the surficial FOS for the 12 and 2 hour of precipitation resolution of the FC2 is 0.95 and 0.96 respectively. Therefore, it can be concluded that FC scenarios have the potential to trigger instabilities in silt embankments.

Similar to the sand embankment, the FC1 shows higher FOS than the FC2 although it has higher I_m. This is true for all the three precipitation resolutions. Again, this raises concern that the use of the I_m method of design climate construction could lead to the overestimation of the factor of safety of embankments.

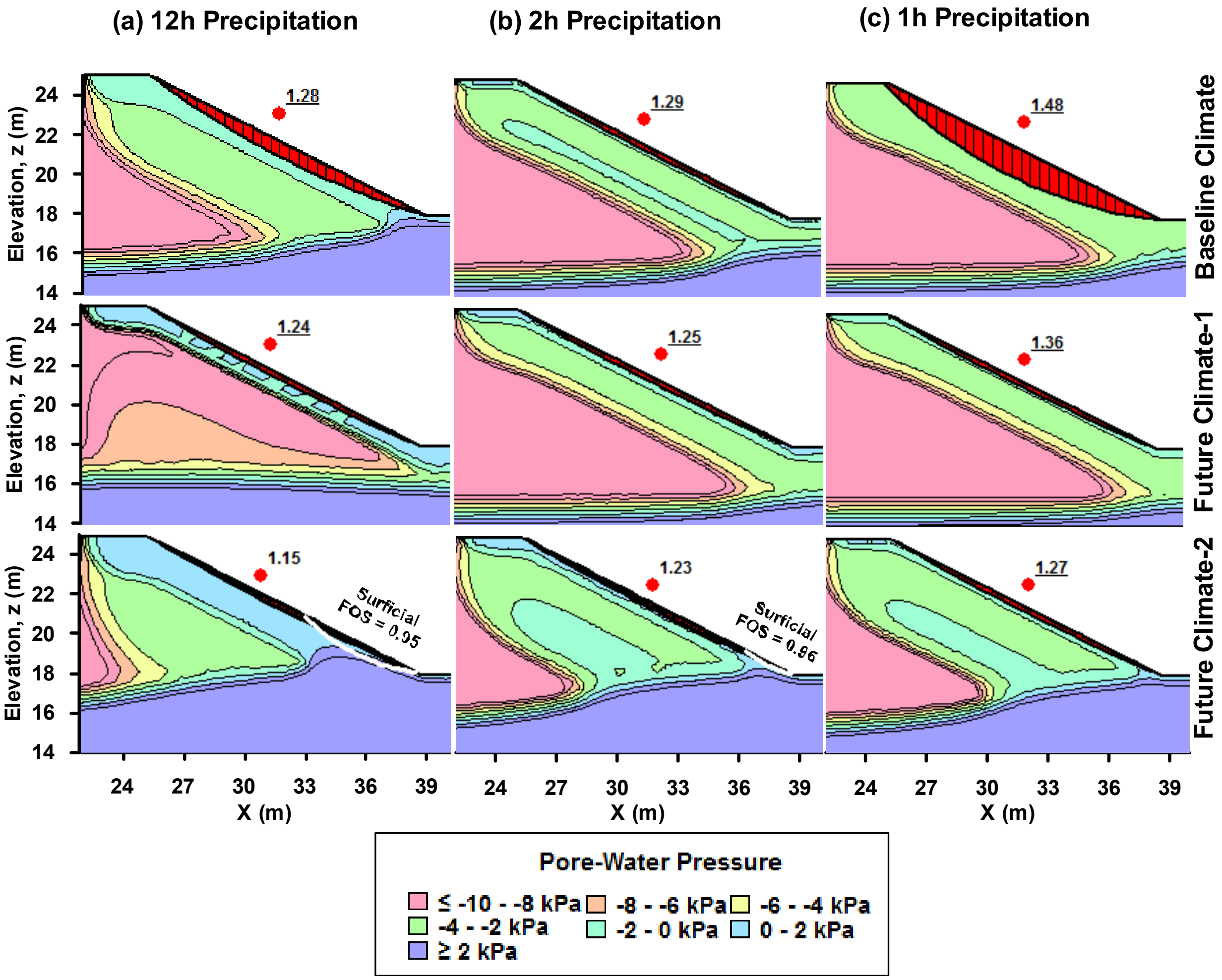

Figure 6.9 FOS plots with PWPs distributions of the silt embankment for three climate ensembles and temporal resolutions of precipitation

6.2.3 Overall findings from Design Climate 1

In the first set of design climate analyses, the stability of the sand and silt embankments were analyzed using 30 years of climate data of baseline and future climate ensembles. Both the regular, and extreme precipitation of 10 to 100 years of return periods were considered. It was observed that the future climate ensembles have potential to affect both the soil water distribution as well as stability of the sand and silt embankments. For the wet years, significantly higher amount of water could infiltrate into the embankments, while during an average year, the embankment could experience a moisture deficit. Both FC ensembles show lower factor of safety than the BC, yet none of the sand embankments had a factor of safety less than 1. The high drainable sand allows rapid pore pressure dissipation for the increasing *NI*, and therefore, the embankment remains stable. On the other hand, the silt embankment shows surficial failures for the FC, which eventually could create the failure of the whole embankment.

The effects of extreme precipitation events were studied by distributing the daily precipitation over the 2 and 1-hour time periods. The results show that the extreme precipitation events cause a decrease in factor of safety for the sand embankment, while it causes an increase in FOS for the silt embankment. The low permeable silt embankment generates higher amount of *RO* for the intense precipitation events, and therefore, less amount of water infiltrates into the embankment resulting in increased FOS. Therefore, it can be concluded that the high permeable sand embankment is susceptible for the short and intense precipitation, while the low permeable silt embankment shows vulnerability for the prolonged precipitation. It should also be noted that, although for silt embankment the over stability increases with precipitation intensities, however the large quantities of surface runoff generated could potentially lead to surface erosion problems.

The annual moisture index based design climate (FC1) shows higher estimation of FOS for both of the sand and silt embankments. Annual moisture index is based on cumulative *P* and *PE* values. There are 2 shortcomings of this approach. First, it is the *AE* that ultimately dictates the water balance not the *PE*, and it should be noted that soil hydraulic properties also play an important role in actual amount of water that can be lost by evaporation. Second, I_m does not take into account the temporal distribution of the *P* and *PE* over shorter time scales. For example, rising temperatures can contribute to increasing evaporative demand and on annual basis it would seem that some of the effects of increased precipitation are countered by the estimates increase in *PE* values. However, over a span of a day, the *PE* will still follow the daily diurnal cycle, but *AE* will also be dependent on the intensity of the precipitation and the fact that whether event happens in the peak evaporation hours or not. As a result, I_m cannot estimate actual water balance at the ground surface. The geotechnical engineers should exercise caution when using this approach, and understand that their results could be over estimating the FOS.

6.3 Design Climate 2

The analysis of future climate showed a significant increase in the frequency of extreme precipitation events. Therefore, the DC2 was considered to study the effects of the increasing extreme precipitation events on the stability of embankments. The DC2 contains intensity duration and frequency (IDF) curves for six different return periods (i.e., 2, 5, 10, 25, 50, and 100 year) for the baseline and future climates. The critical durations of the IDF curves were selected by taking into consideration the hydraulic properties of the fills of embankments. In the previous section (6.2: DC1), it has been observed that the sand embankments are more susceptible to short and intense precipitation events, while the silt embankments show more vulnerability to the prolonged precipitation events. As such, a duration of 1-hour was selected for the sand embankment, and 24-hour for the silt embankment. The results are presented separately for the sand and silt embankments in the subsequent sections.

6.3.1 Sand embankment

The stability of the sand embankment was investigated using one (1) hour storms for six different return periods. Similar to DC1 the results are presented in three different steps. The effects of evaporation were not taken into consideration, and therefore, the water balance at the ground surface contains only two components; *NI* and *RO*. To investigate the effects of short term extreme precipitation events on the constant head boundary at the right hand side, the constant head boundary flux is presented together with the water balance at the ground surface, and the results are reported as cumulative boundary fluxes. The changes in PWP are then presented followed by the temporal variations of the factor of safety of embankments.

6.3.1.1 Boundary fluxes

The fluxes at the ground surface and constant head boundary are presented in combine as boundary fluxes. Boundary fluxes indicate the amount of water that comes in or goes out of the system, and can be used to conduct mass balance analysis. The highest intensity of applied 1 hour storms was still less than K_{sat} of sand. It was observed that no *RO* was generated and all prescribed flux entered into the embankment. At the constant head boundary condition, it was found that a small amount of water left the system, which was defined as outflow (*OF*). A plot showing the comparisons of cumulative *NI* and *OF* between the baseline and future climates is shown in Figure 6.10a. It can be seen in this figure that the cumulative *NI* linearly increases over the 1 hr. period of time with the rate of applied precipitation. The cumulative *OF* (presented as negative value in Figure 6.10a) shows that the *OF* remains constant for all storms. This indicates that the water infiltrates into the embankment during the 1-hour storm event does not have sufficient time to reach the outflow boundary, and remains stored within the embankment at the end of the event.

A comparison between the baseline and future climates cumulative *NI* is shown in Figure 6.10b. It can be seen in Figure 6.10b that the cumulative *NI* for the BC of 2 year return period (BC-2) is 32 mm. While the FC of 2 year return period (FC-2) shows a cumulative *NI* of 43 mm, a 34% increase compare to the baseline. As the return period increases, so too does the change in cumulative *NI* between the baseline and future climates (Figure 6.10b). By the time when the return period has reached 100 years, the FC has a cumulative *NI* 80% greater than the BC.

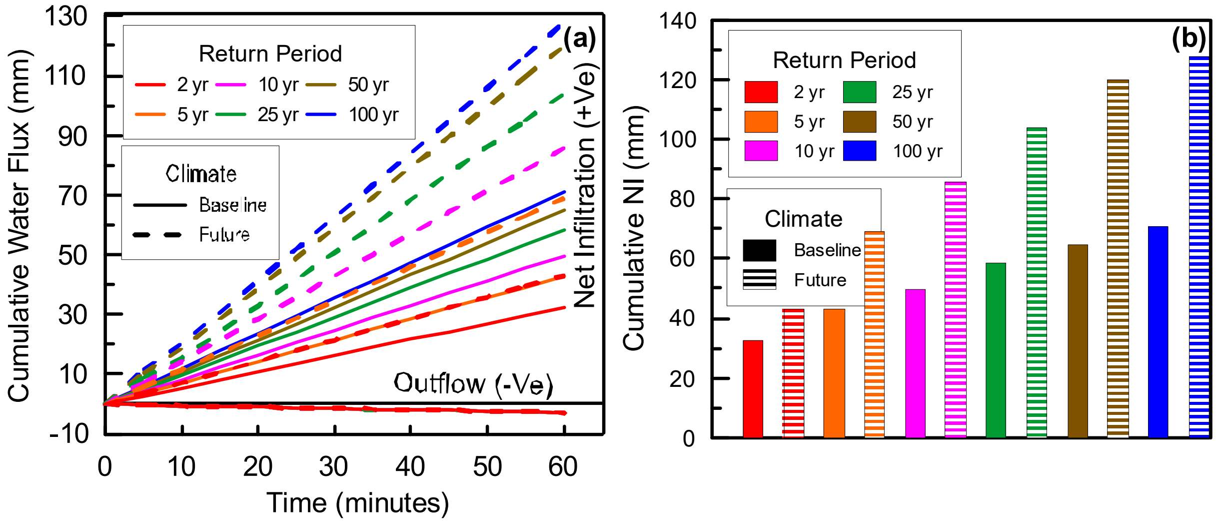

Figure 6.10 (a) Cumulative boundary fluxes of the sand embankment after 1 hour storms, and (b) Comparison in cumulative net infiltration

6.3.1.2 Pore-water pressures distribution

The increasing net infiltration associated with the future IDF curves has potential to affect the PWPs in the sand embankment. The PWPs were calculated at three vertical sections of the embankment. The locations of the three sections along with initial PWPs profiles are shown in Figure 6.11a. It can be seen in Figure 6.11a that the initial PWPs at each section was around -4 kPa at the ground surface. For the DC2, a wet initial condition from the 30 years of initial model was selected, which has almost a steady -4 kPa PWPs profiles. Figure 6.11a shown that the PWPs remain relatively unchanged with depth until the depth of 16m, after which they linearly increase to 0 kPa at the groundwater table at the depth of 15 m.

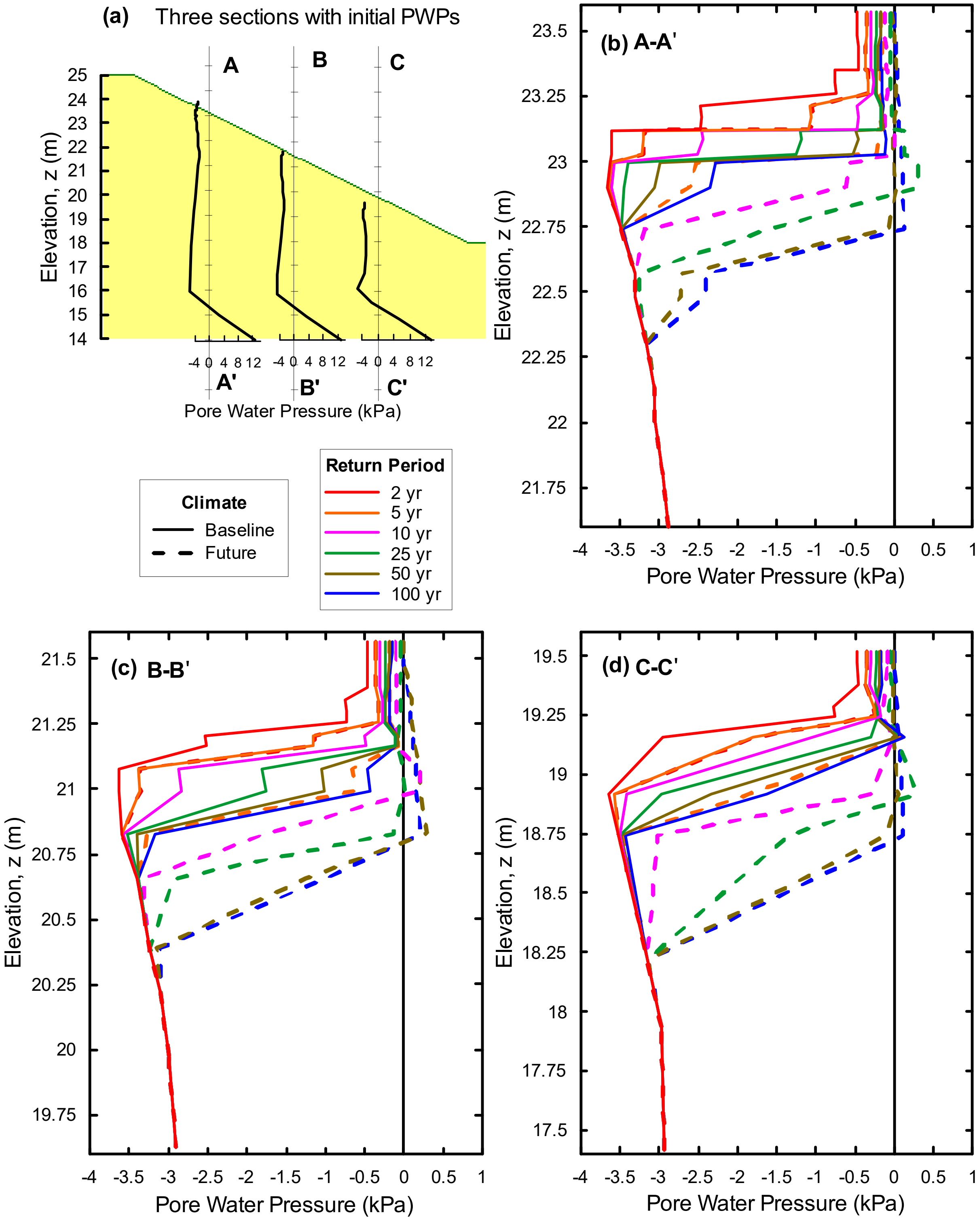

Figure 6.11 PWPs distribution of the sand embankment (a) initial conditions, and after one-hour storm at (b) top A-A′ section, (c) middle B-B′ section, and (d) bottom C-C′ section

The PWPs for the 1-hour storms of DC2 were calculated and plotted for the top 2 meters only, and are shown in Figure 6.11b-6.11d. The results from the DC1 indicated that most of the PWPs changes happen within 2 meters of the ground surface. It can be observed that the PWPs profiles at all three sections show similar behaviors for each storm. The 2 m vertical PWPs profiles have 3 distinct zones. Zone 1 is nearly saturated to saturated (-1 to 0 kPa). Zone 2 is a transition zone (decreases from -1 kPa to -4 kPa), and Zone 3 is the unsat zone. The depths of the nearly saturated and transition zones differ between the baseline and future climates and between different return periods. For example, at cross section A-A' (Figure 6.11b) the depth of near saturation for the BC of 100 year return period (BC-100) is 0.6 m (elevation of 23.6 m to 23.0 m), and its total depth of influence is 0.85 m (elevation 23.60 m to 22.75 m). In comparison, the FC of 100 year return period (FC-100) (dash blue line) shows a saturation depth of 0.9 m (elevation 23.6 m to 22.7 m) with a total depth of influence of 1.3 m (elevation 23.6 m to 22.3 m). An increased depth of saturation and overall zone of influence between the future and baseline climates is also present for all other return periods of storms at all other cross-sections. Moreover, future climate causes higher saturation than the baseline climate, and for the FC with return periods of 25-year and higher the near surface of the embankment is fully saturated or very close to full saturation. The change in PWP from near-saturation to saturated conditions can have significant implications on the stability of the slope, and are examined in depth in the following section.

6.3.1.3 Factor of safety

The factor of safeties of the sand embankment were calculated for all six return periods for the baseline and future climates. The FOS were calculated over five-minute intervals in the 1-hour storm period. The calculated FOS for each of the simulations are plotted in Figure 6.12. Review of this figure indicates that for BC-2 one can see that the FOS remains relatively constant at 1.47 over the duration of the storm. Therefore, it can be concluded that the storms of intensity

21.8 mm/hr. will not have any significant influence on the stability of the sand embankment. Similarly, it can also be observed that FOS for BC-5, and FC-2 remains constant at 1.47 for the first 55 minutes before slightly decreasing to 1.43. Therefore, it can also be concluded that storms unto 28.7 mm/hr. will have negligible influence on stability. However, as the storm intensity increases to 41.38 mm/hr., which is representative of future climate of 5 year return period, there is substantial decrease in FOS (Figure 6.12). The observed FOS for the FC-5 at the end of the 1 hr. event is 1.33, which is 0.1 lower than the BC-5. Similar observations can be mode for other return periods higher than 5. The lowest observed FOS for the sand embankment is 1.21 for the FC-100. Even though the sand embankment remained stable in the 1 hour storms, a considerable decrease in FOS was observed for the FC scenarios.

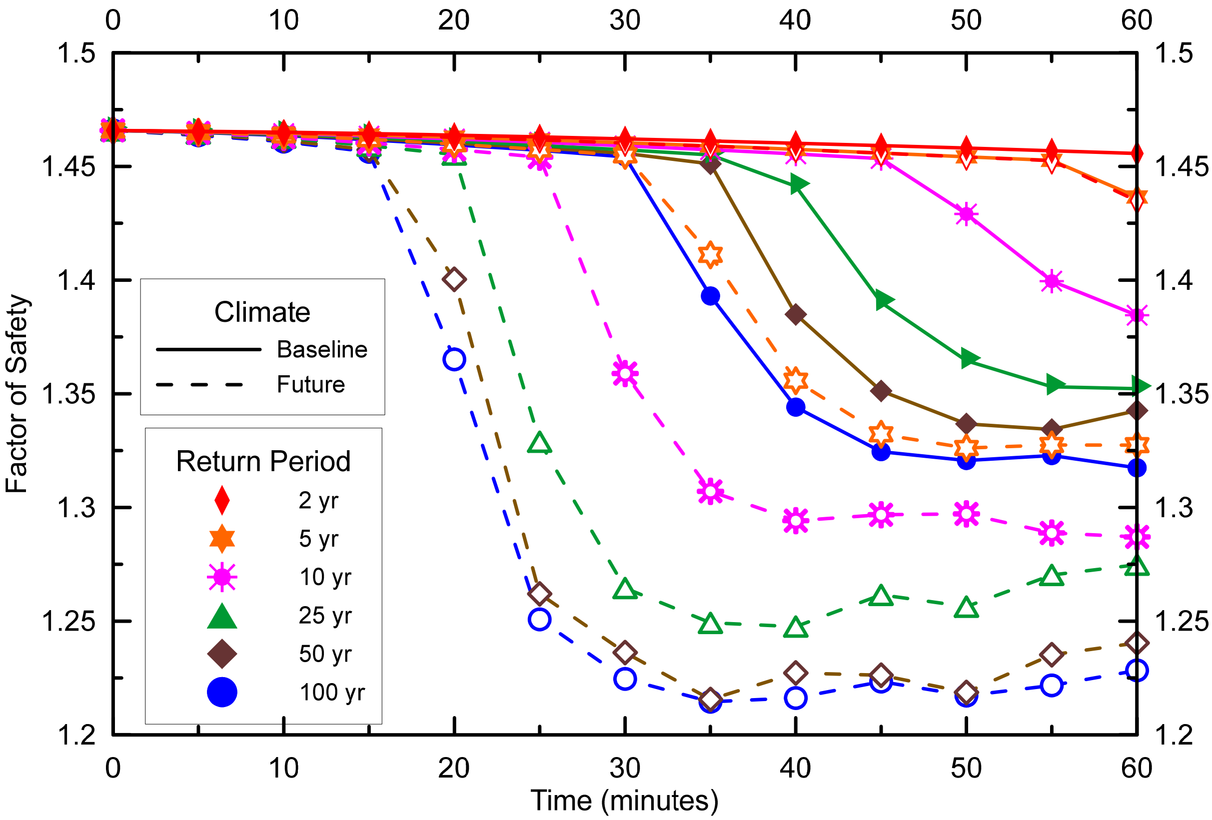

Figure 6.12 Temporal variations of FOS values of the sand embankment for the baseline and future storms of six return periods

6.3.2 Silt embankment

The same set of baseline and future IDF curves were used to investigate the stability of the silt embankment. However, a different critical duration for storms was selected. The selection was based on the observations in Section 6.2 that the silt embankments are more susceptible to prolonged precipitation events of lower intensity. Therefore, the longest available duration of the IDF curves, of 24 hr. was selected for the stability analysis of the silt embankment. The results are presented in the similar way as for sand embankment in the following sections.

6.3.2.1 Boundary fluxes

The cumulative boundary fluxes at the ground surface and constant head boundary were calculated. The results are plotted in Figures 6.13a to 6.13f for six different return periods. Modeling results from DC1 showed significant *RO* for higher precipitation intensity events. This trend was also observed in current simulations. The amount of *RO* increases with return periods from Figures 6.13a to 6.13f. Outflow was observed at constant head boundary and was higher than the quantities observed for sand, however this is due to the difference in simulation times. Sand simulations were run for 1-hour while these simulations were run for 24-hour period. The cumulative *NI* showed a degree of non-linearity when compared to sand. A portion of applied precipitation fluxes was reported as *RO* which reduced the *NI,* and changes the trend that was observed for the sand embankment.

It can be observed in Figure 6.13 that the precipitation increases with increase in return periods and higher precipitation are associated with future climate for same return period. For example, seen in the increase in cumulative precipitation for the 2 year return period of storms is 29 mm (from 86 mm to 115 mm). This value increases to 110 mm for the 25 year (Figure 6.13d) and 147 mm for the 100 year return period (Figure 6.13f). Although FC shows a significant increase in precipitation, the resulting *NI* does not follow the same trend. The increases in cumulative

NI after the 24-hour storms of the 2, 25, and 100 year return periods are 16 mm, 33 mm and 30 mm respectively. This decrease in *NI* is because as the precipitation intensity increases, more *RO* is generated. This higher amount of *RO* for FC has probability to create surface erosion problem of the embankment.

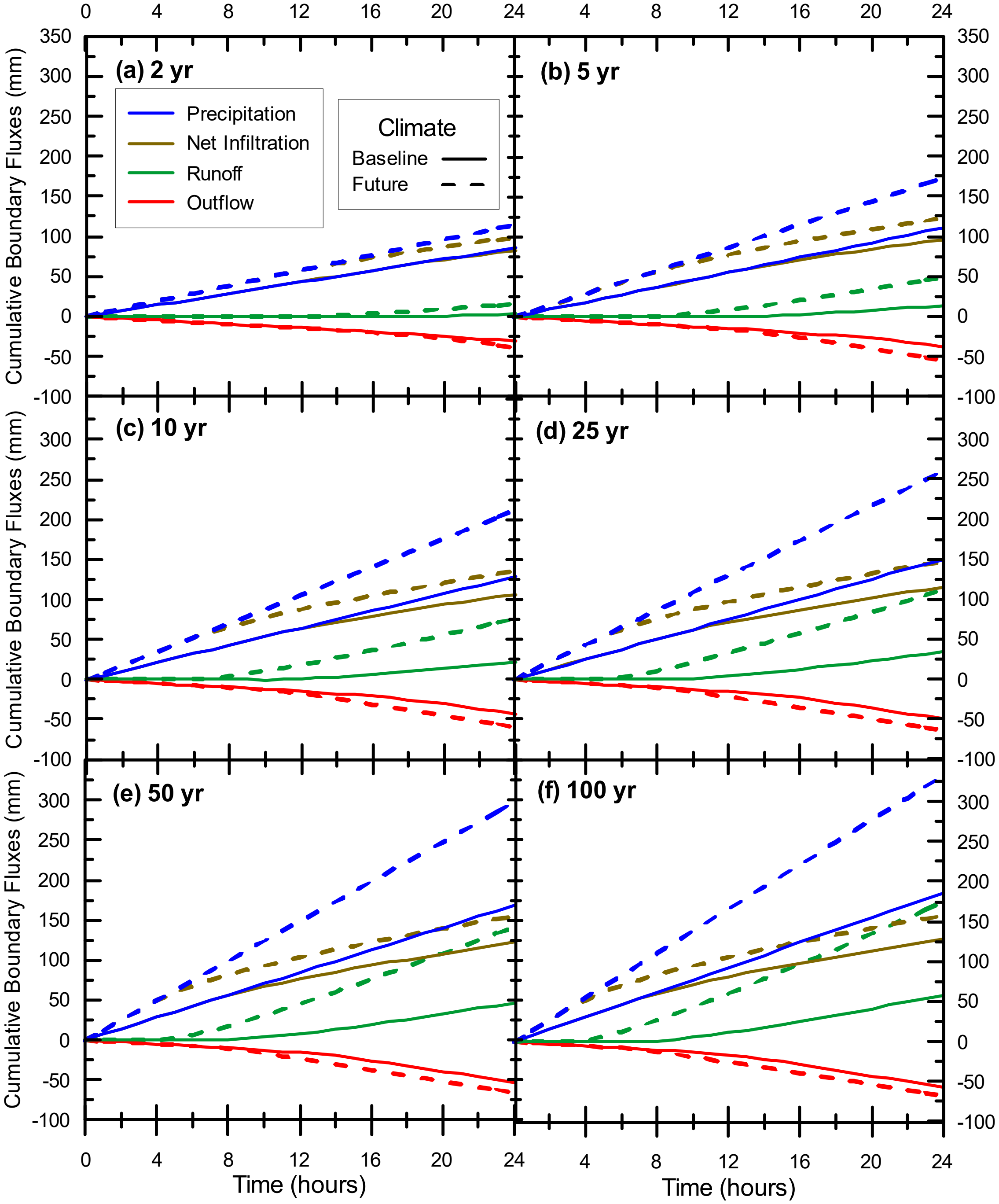

Figure 6.13 Cumulative boundary fluxes of the silt embankment after 24-hour storms baseline and future storms of six different return periods

The cumulative *OF* is presented as negative value in Figure 6.13. It can be seen that the cumulative *OF* is the lowest for the 2 year storms, and then gradually increases with return periods. The difference on cumulative *OF* between the baseline and future climates at the end of the 24 hour storms does not show any consistent trend. The highest difference of 17 mm is observed for the storm of 5 year return period (Figure 6.13b), while the lowest difference of 8 mm is observed for the 2-year storm (Figure 6.13a). This inconsistent pattern of the cumulative *OF*s shows a good agreement with the pattern of *NI*. Therefore, it can be concluded that the infiltrated precipitation from the 24-hour storms flows through the silt embankment, and reaches the *OF* boundary.

6.3.2.2 Pore-water pressures distribution

Similar to the sand embankment, the variations of PWP were calculated at three vertical sections (shown in Figure 6.14a). It can be seen in Figure 6.14a that the initial PWP at all three sections is negative from the ground surface down to an elevation of 16 m, after which they are hydrostatic.

The PWP in the top 2 m of silt embankment for the three cross-sections were plotted for further analysis (Figure 6.14b, c, and d respectively). Similar to the sand embankment, the silt embankment also shows similar pattern in PWP distributions across the three cross-section profiles. However, there is a significant increase in PWP moving from A-A’ to C-C’. In section A-A’, the PWP for all the baseline storms are negative (Figure 6.14b), while at section B-B’ the PWPs are negative for the 4 baseline storms (Figure 6.14c), and at section C-C’ for only 2 (Figure 6.14d). This indicates that the embankment is saturated at the toe of the slope for nearly all climate scenarios, which has significant implications in stability analysis.

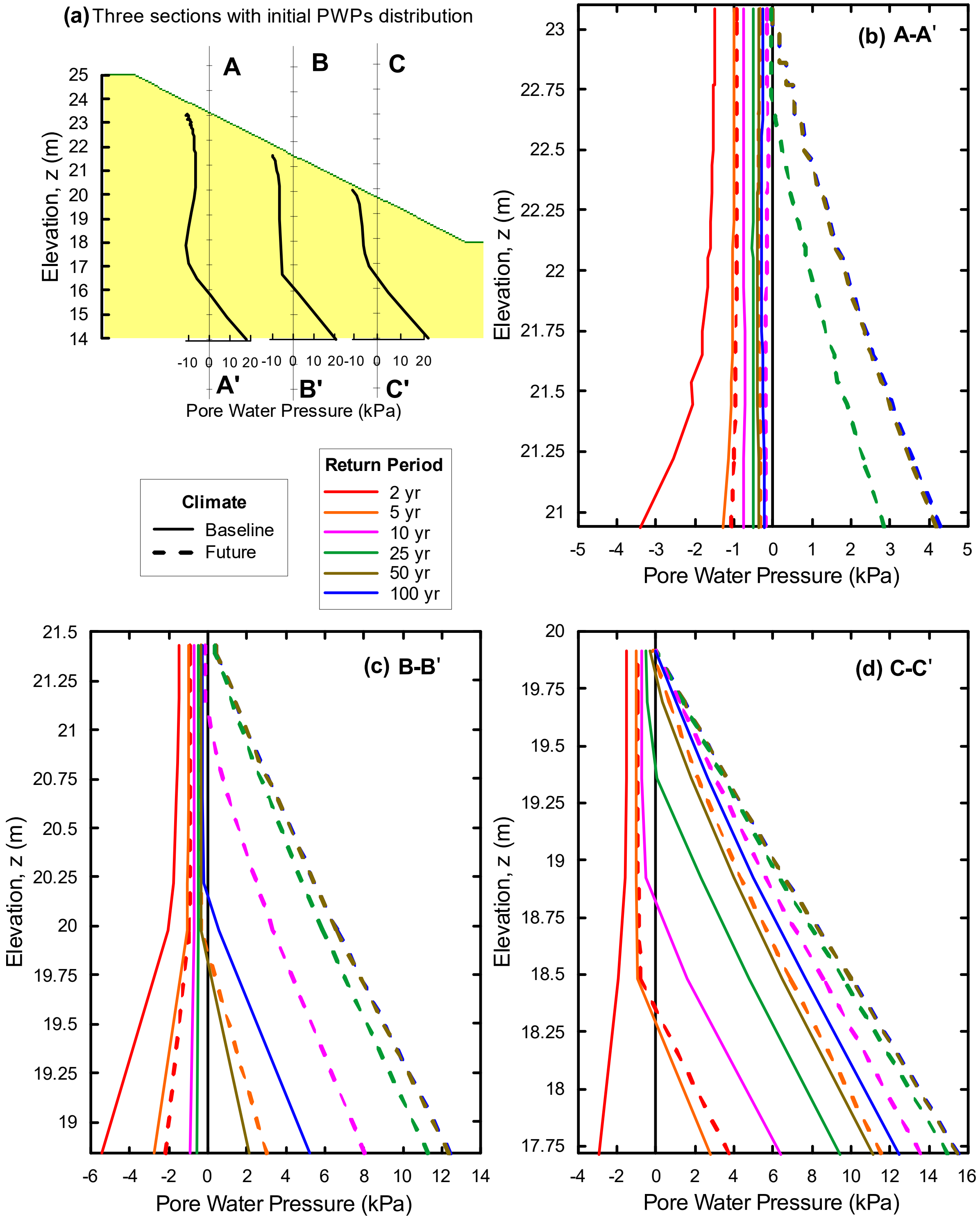

Figure 6.14 PWP distributions for the silt embankment (a) at the beginning, and after 1 hour storms in section (b) A-A′, (c) B-B′, and (d) C-C′

The FC with higher *P* and *NI* generates considerably higher PWP comparing with the BC. In Figure 6.14b, it can be seen that the BC-2 generates a linear PWP profile starting at around -1.5 kPa at the ground surface decreases to -3.5 kPa at a depth of 2m. In contrast, FC-2 has a nearly vertical PWP profile of -1 kPa. For return periods 10 year and greater, positive PWP can be observed for FC at section A-A' (i.e., 4.5 kPa in FC-100). Similar observations can be made for the sections B-B' (Figure 6.14c) and C-C' (Figure 6.14d) respectively. This excess PWP has the potential for triggering instability events and should be examined in details for the FC.

6.3.2.3 Factor of safety

The FOS of the silt embankment was calculated in 1-hour interval over the 24-hour storm duration. The temporal variations of the FOS values are shown in Figure 6.15. It can be seen that the initial FOS values for all storms is 1.71, and then it decreases with time. The FOS of the silt embankment at the end of 24 hours for BC-2 and FC-2 are 1.44 and 1.35 respectively, resulting in a difference of 0.09. Similar to the sand embankment, the difference in FOS between the baseline and future climates increases as the return periods increase. Consistent the PWP results, the future storms of 10 year and higher return periods have lower FOS values than the FC-100. The FOS of the FC-100 was 1.17, whereas the FOS for the FC-10, 25, 50, and 100 were1.1, 1.0, 0.9, and 0.9 respectively.

With a failure event being triggered in the silt embankment at the end of the 25-year storm, and in the 20th hour for the 50 and 100 year storms it is clear that FC scenarios can have a detrimental effect on the stability of a silt embankment.

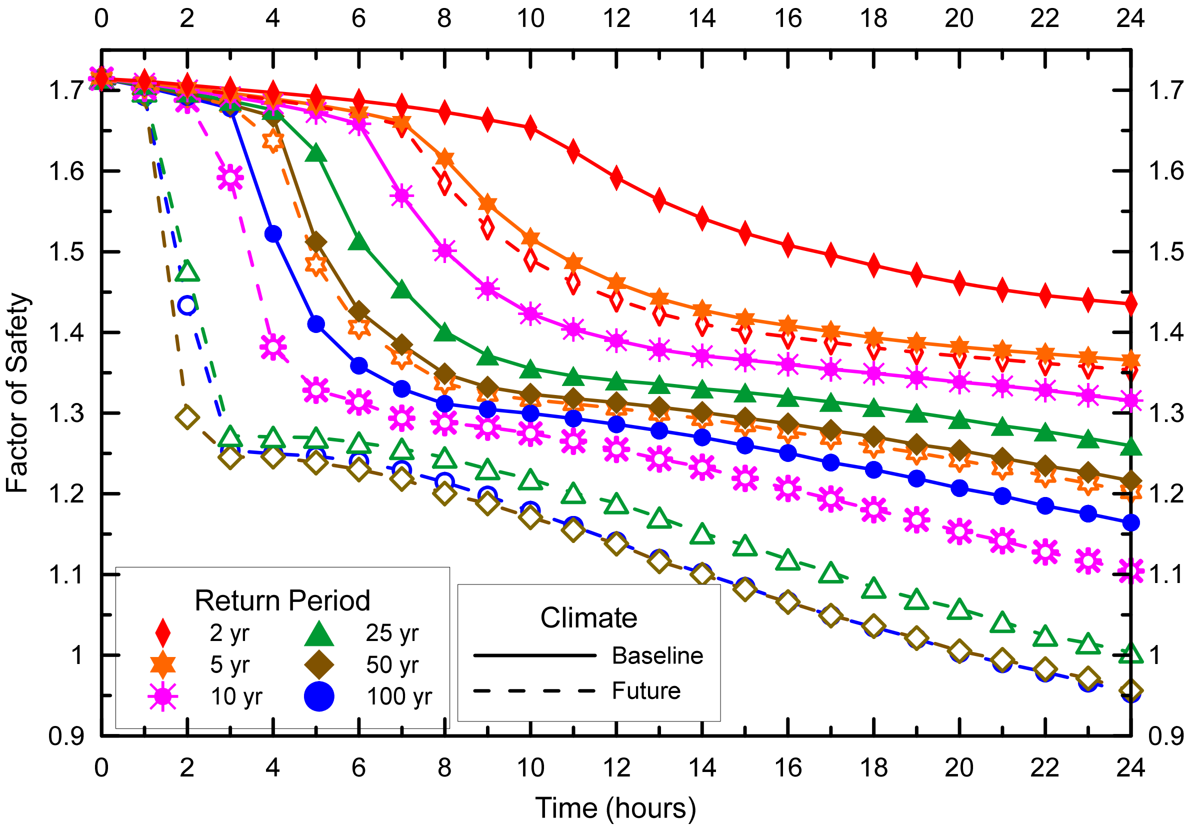

Figure 6.15 Temporal variations of the FOS of the silt embankment for the baseline and future storms of six different return periods

6.3.3 Overall findings from Design Climate 2

The objectives of the DC2 were to investigate the effects of increasing intensity and frequency of future extreme precipitation events. The results presented in the above sections show that the future extreme precipitation events can have significant impacts on the water balance at the ground surface, pore-water pressure distribution, and resulting stability of the embankments. The higher intense future storms could potentially add large amounts of *NI* to the sand embankment. For silt embankments, it is antcipaited that future storms can generate, large quantites of *RO*. The highly permeable sand material have the capability to allow large qunatities of precipitation to infiltrate without generating any significant amounts of *RO*. As the sand embankment allowed water to pass through with relative ease without development of signficant excess porewater pressure, it is antcipated that the sand embankment considered in this research would remain stable for the future climatic condition considered in this research.

In contrast to sand embakment, the silt embankment would probaly see realtivly little increases in *NI*, due to its high water retention and low drainage characteristics. However, due to the hydrulic properties of the silt materail, excess pore pressure can devlop in silt embankmets resulting in FOS below 1 for certain future climatic conditions conisderd in this research. Moreover, results also indicate that the silt embankments might be more prone to surface erosion problems due to generation of large qunatities of *RO*. In conclusin the results from DC2 show that for the extreme precipitation events of future cosnidered in this reserach, sand embankments would remain stable, but the silt embankment have the higher probablity to fail.

Chapter 7. Conclusions and Recommendations

7.1 Introduction

The objectives of this thesis were to understand and quantify how a changing climate will affect the stability of soil embankments in Ontario. The first phase of this research was to quantify future climate changes by calculating how climate variables will change over the next 90 years. The impacts of this changing climate on the stability of soil embankments were then estimated by comparing the future and historical factors of safety. This chapter presents the major conclusions of this thesis. This chapter ends with the contributions of this research and recommendations for further avenues of research.

7.2 Overall Conclusions

7.2.1 Changes in future climate variables for Toronto, Ontario

The increasing trend of temperatures is expected to continue over the 21st Century in Toronto. It was found that the mean annual temperature could rise as high as 6°C at the end of this century. The potential evaporation follows a similar trend as temperature increasing with time. The annual precipitation also shows an increasing trend, with the highest observed increase in the 2080s of 18.5%. However, these increases in precipitation are not consistent throughout a water year. The increasing precipitation is predicted to occur mostly in the inactive period, while the active period could experience a mix of increase and decrease. The extreme precipitation events show a significant increase for the future climate, and the number of extreme events in the 2080s could be more than double of the baseline period. The changes in extreme precipitation also shows variations over the water year. However, the majority of extreme precipitations are predicted to occur in the active period.

7.2.2 Effects of climate change on soil embankments in Ontario

The effect of climate change on the stability of soil embankments was investigated using two DCs for two different soil types. It was found that the future design climates affected the stability of both the sand and silt embankments stability, though not equally. Overall, the highly permeable sand showed greater stability over time when compared to the silt embankments. The sand embankment is capable to quickly drain excess PWPs, and thereby increases in *NI* due to climate change did not significantly decrease the embankments stability. In contrast, the less permeable silt embankment was able to store greater volumes of water from increasing precipitation events, which in turn generated excess pore-water pressures triggering instabilities. Most importantly it was found that the silt embankments experienced surficial failures during precipitation events which have the potential to trigger global failures.

7.2.3 Effects of temporal resolution of precipitation on the stability of soil embankments

In most instances, precipitation values are recorded as daily values, where in reality precipitation events rarely last for a full 24 hours. As such, precipitation data of higher resolutions is necessary to accurately estimate the embankment instability due to precipitation (Davies 2011). The results of this study show that the effects of the temporal resolution of precipitation also depends on the hydraulic properties of fill materials of embankments. The intense precipitation events of higher resolutions create a large volume of *NI* over a short period of time for the sand embankment. In contrast, the low permeability of silt does not allow more water to infiltrate into the embankment, and thereby generates a large volume of *RO*. For precipitation events of less intensity and smaller temporal resolutions, the majority of precipitation infiltrated into both the sand and the silt embankments. When this occurs, the sand embankment can drain the water with limited impact on stability whereas in the silt embankment excess PWPs are generated which trigger failure events.

Therefore, embankments with coarse fill materials are more susceptibility to instability for short and intense precipitation events, and the longer and less intense precipitation events will be more likely to trigger instabilities in silt embankments. Using daily precipitation data therefore could lead to a falsely high estimation of stability for a sand embankment, while opposite results could be observed for the silt embankment.

7.2.4 Annual moisture index method of design climate construction

Geotechnical and geoenvironmental engineers frequently use the I_m method to construct design climates. However, this research found that the I_m method overestimates the factor of safety for both of the sand and silt embankments and therefore should be used carefully.

Two shortcomings of using I_m were identified. Firstly, I_m calculates water balance at the ground surface based on annual *P*, and *PE,* but *AE* and hydraulic properties of the surface soil play an important role in actual amount of water that can be lost by evaporation. Secondly, I_m does not take into account the temporal distribution of *P*, and *PE* over smaller time scales. Over a span of a day, the *PE* follows the daily diurnal cycle, but *AE* also depends on the intensity of the precipitation and the fact that whether event happens in the peak evaporation hours or not.

7.3 Impact of research

The results of this research found that climate change can have a direct impact on the stability of soil embankments in Ontario. The findings of this research can be now used to modify current embankment design guidelines and specifications to incorporate climate change into the design process. In addition, it is anticipated that the findings of this research will be used not only for improving design methodology for future embankments, but also for evaluating stability risk for current soil embankments.

This thesis shows that the temporal resolution of climate data has potential to affect the end results, and it is important to measure higher resolutions climate data. This research also illustrates that the commonly used I_m method of design climate construction has limitations, and could lead to overestimation of the FOS of embankments.

7.4 Next Steps

This research has yielded significant findings and results for understanding how climate change will impact the stability of soil embankments in the future in Ontario. However, the inherent nature of research is that inquiry should lead to further inquiry and additional research questions. As such, a number of next steps and avenues for further investigation have arisen, and are suggested as areas of future work.

7.4.1 Multiple locations and embankment profiles

In any one study only a number of parameters can be varied. This study was carried out for the city of Toronto in Ontario. The next step in this research would be to investigate multiple locations in order to understand how climate change will impact embankment stability at other locations in the province of Ontario. In addition, the geometry of embankment profile was not varied in this research. A parametric study on the design parameters such as height, slope, geology, and material properties of embankment would provide additional understanding on transportation embankments behavior under changing climate.

7.4.2 Temporal resolution of climate data

In this research study, daily climate data was used to generate the design climates. It was observed that the climate data of higher temporal resolutions can be helpful to accurately predict the PWPs within the embankments. Although the effect of temporal resolution of the climate data was quantified indirectly it would be interesting to use sub-daily to sub-hourly climate data to further investigate the influence of temporal resolution water dynamics in embankment and associated stability.

7.4.3 Probabilistic study on the stability of embankment

This study focused on the impacts of increasing soil water content from future climates on the stability of embankments. However, it was also shown in this research that climate change has the potential to create moisture deficits within the embankment triggering vegetation loss, desiccations, volume change, and cracks. All of these have potential to affect the strength of soil embankments. Therefore, a probabilistic study on the stability of soil embankments considering all the consequences of moisture deficit would be an excellent pursuit for the dry years when climate is predicted to become drier.

References

Allen, R.G., Pereira, L.S., Raes, D., Smith, M., and others. 1998. Crop evapotranspiration-Guidelines for computing crop water requirements-FAO Irrigation and drainage paper 56. FAO, Rome, **300**(9): D05109.

Alvarez-Acosta, C., Lascano, R.J., Stroosnijder, L., and others. 2012. Test of the Rosetta pedotransfer function for saturated hydraulic conductivity. Open Journal of Soil Science, **2**(03): 203.

Barnes, G.E. 2010. Soil mechanics: principles and practice. *In* 3rd edition. Palgrave Macmillan, New York.

Bashir, R., Sharma, J., and Stefaniak, H. 2015. Effect of hysteresis of soil-water characteristic curves on infiltration under different climatic conditions. Canadian Geotechnical Journal, **53**(2): 273–284. doi:10.1139/cgj-2015-0004.

Bishop, A.W. 1959. The principle of effective stress. Teknisk ukeblad, **39**: 859–863.

Bo, M.W., Fabius, M., and Fabius, K. 2008. Impact of global warming on stability of natural slopes. Presse de Univ. Laval, Quebec. p. 594.

Borah, D.K., and Bera, M. 2003. Waterhed-scale hydrologic and nonpoint-source pollution models: review of mathematical bases. Transactions of the ASAE, **46**(6): 1553–1566. doi:10.13031/2013.15644.

Brinkgreve, R.B.J., and Vermeer, P.A. 1998. Plaxis manual. Version, **7**: 5–1.

Buma, J. 2000. Finding the most suitable slope stability model for the assessment of the impact of climate change on a landslide in southeast France. Earth Surface Processes and Landforms, **25**(6): 565–582.

Buma, J., and Dehn, M. 1998. A method for predicting the impact of climate change on slope stability. Environmental Geology, **35**(2–3): 190–196. doi:10.1007/s002540050305.

Camargo, A.P., Marin, F.R., Senteltas, P.C., and Picini, A.G. 1999. Adjust of the Thornthwaite's method to estimate the potential evapotranspiration for arid and superhumid climates, based on daily temperature amplitude. Rev. Bras. Agrometeorol., **7**(2): 251–257.

Carsel, R.F., and Parrish, R.S. 1988. Developing joint probability distributions of soil water retention characteristics. Water Resources Research, **24**(5): 755–769. doi:10.1029/WR024i005p00755.

CCDP. 2017. Ontario Climate Change Data Portal. Available from http://www.ontarioccdp.ca/ [accessed 10 January 2017].

Chiang, S.-H., and Chang, K.-T. 2011. The potential impact of climate change on typhoon-triggered landslides in Taiwan, 2010–2099. Geomorphology, **133**(3–4): 143–151. doi:10.1016/j.geomorph.2010.12.028.

Cloutier, C., Locat, J., Geertsema, M., Jacob, M., and Schnorbus, M. 2016. Summary of the report Potential Impacts of Climate Change on Landslides Occurrence in Canada. Canadian Geotechnical Society, Vancouver.

Collison, A., Wade, S., Griffiths, J., and Dehn, M. 2000. Modelling the impact of predicted climate change on landslide frequency and magnitude in SE England. Engineering Geology, **55**(3): 205–218.

Colombo, S.J., McKenney, D.W., Lawrence, K.M., Gray, P.A., and others. 2007. Climate change projections for Ontario: practical information for policymakers and planners. Climate Change Research Report-Ontario Forest Research Institute, (CCRR-05). Available from http://www.cabdirect.org/abstracts/20073207505.html [accessed 21 December 2016].

Coutinho, A.P., Lassabatere, L., Montenegro, S., Antonino, A.C.D., Angulo-Jaramillo, R., and Cabral, J.J.S.P. 2016. Hydraulic characterization and hydrological behaviour of a pilot permeable pavement in an urban centre, Brazil. Hydrological Processes, **30**(23): 4242–4254. doi:10.1002/hyp.10985.

Davies, O. 2011. Numerical analysis of the effects of climate change on slope stability. PhD Thesis, Newcastle University, Newcastle, UK. [accessed 9 December 2016].

Dehn, M., and Buma, J. 1999. Modelling future landslide activity based on general circulation models. Geomorphology, **30**(1–2): 175–187. doi:10.1016/S0169-555X(99)00053-7.

Deng, Z.J. 2016a, December 1. Personal communication on the downscaling of climate data.

Deng, Z.J. 2016b, December 1. Personal communication on the performance of GCMs.

Dingman, S.L. 2015. Physical hydrology. Waveland press, Illinois, United State.

Dixon, N., and Brook, E. 2007. Impact of predicted climate change on landslide reactivation: case study of Mam Tor, UK. Landslides, **4**(2): 137–147. doi:10.1007/s10346-006-0071-y.

Environment Canada. 2011a, October 31. Historical Climate Data - Climate - Environment Canada. Available from http://climate.weather.gc.ca/ [accessed 22 December 2016].

Environment Canada. 2011b, October 31. Engineering Climate Datasets - Climate - Environment and Climate Change Canada. Available from http://climate.weather.gc.ca/prods_servs/engineering_e.html [accessed 27 May 2017].

Environment Canada. 2011c, October 31. Canadian Climate Normals - Climate - Environment and Climate Change Canada. Available from http://climate.weather.gc.ca/climate_normals/index_e.html [accessed 16 July 2017].

Feddes, R.A., Bresler, E., and Neuman, S.P. 1974. Field test of a modified numerical model for water uptake by root systems. Water Resources Research, **10**(6): 1199–1206.

Flato, G., Marotzke, J., Abiodun, B., Braconnot, P., Chou, S.C., Collins, W.J., Cox, P., Driouech, F., Emori, S., Eyring, V., Forest, C., Gleckler, P., Guilyardi, E., Jakob, C., Kattsov, V., Reason, C., and Rummukaines, M. 2013. Evaluation of Climate Models. In: Climate Change 2013: The Physical Science Basis. Contribution of Working Group I to the Fifth Assessment Report of the Intergovernmental Panel on Climate Change. *In* Climate Change 2013. Cambridge University Press. pp. 741–866. Available from https://www.ipcc.ch/pdf/assessment-report/ar5/wg1/WG1AR5_Chapter09_FINAL.pdf [accessed 9 December 2016].

Fredlund, D.G., Morgenstern, N.R., and Widger, R.A. 1978. The shear strength of unsaturated soils. Canadian geotechnical journal, **15**(3): 313–321.

Fredlund, D.G., Rahardjo, H., and Fredlund, M.D. 2012. Unsaturated soil mechanics in engineering practice. John Wiley & Sons, Inc., Hoboken, New Jersey.

Fredlund, D.G., and Xing, A. 1994. Equations for the soil-water characteristic curve. Canadian geotechnical journal, **31**(4): 521–532.

Fredlund, D.G., Xing, A., Fredlund, M.D., and Barbour, S.L. 1996. The relationship of the unsaturated soil shear to the soil-water characteristic curve. Canadian Geotechnical Journal, **33**(3): 440–448. doi:10.1139/t96-065.

Fredlund, M.D. 2001. SVFluxManual, SoilVision Systems. Saskatoon, SK.

Fredlund, M.D., Zhang, J.M., Tran, D., and Fredlund, D.G. 2011. Coupling heat and moisture flow for the computation of actual evaporation. *In* Proceedings of the Canadian Geotechnical Conference and Fifth Pan-American Conference, Toronto, Ont. pp. 2–6.

Geo-Slope International Ltd. 2014a. Vadose Zone Modeling with VADOSE/W. Available from https://www.geo-slope.com/ [accessed 20 February 2017].

Geo-Slope International Ltd. 2014b. Stability modeling with SLOPE/W. GEO-SLOPE International Ltd. Available from https://www.geo-slope.com/products/slope-w [accessed 21 February 2017].

Geo-Slope International Ltd. 2017. GEO-SLOPE > Products > GeoStudio. Available from https://www.geo-slope.com/products/geostudio [accessed 28 July 2017].

Giorgi, F., and Mearns, L.O. 1991. Approaches to the simulation of regional climate change: a review. Reviews of Geophysics, **29**(2): 191–216.

Golder Associates. 2015. Foundation investigation and design report on embankment widening and RSS wall construction of highway 400 from north of king road to north of south canal bridges, Regional Municipality of York. Foundation Report, Golder Associates, Toronto, Canada.

Government of Canada, A. and A.-F. 2013, May 1. Length of growing season in Ontario. publication. Available from http://www.agr.gc.ca/eng/science-and-innovation/agricultural-practices/agriculture-and-climate/future-outlook/climate-change-scenarios/length-of-growing-season-in-ontario/?id=1363033977515 [accessed 14 July 2017].

Government of Canada, E. and C.C.C. 2010a, February 1. Environment and Climate Change Canada - Climate Change - Climate Modelling and Analysis. Available from https://www.ec.gc.ca/ccmac-cccma/ [accessed 24 July 2017].

Government of Canada, E.C. 2010b, February 1. Environment Canada - Climate Change - Canadian Climate Data and Scenarios. Available from http://ccds-dscc.ec.gc.ca/?page=main&lang=en [accessed 3 April 2017].

Grundstein, A. 2008. Evaluation of climate change over the continental United States using a moisture index. Climatic Change, **93**(1–2): 103–115. doi:10.1007/s10584-008-9480-3.

Gupta, S.C., and Larson, W.E. 1979. Estimating soil water retention characteristics from particle size distribution, organic matter percent, and bulk density. Water resources research, **15**(6): 1633–1635.

Halifax Regional Municipality. 2007. Climate change risk management strategies for the Halifex Municipality. Halifax Regional Municipality, Halifix.

Hungr, O., Leroueil, S., and Picarelli, L. 2014. The Varnes classification of landslide types, an update. Landslides, **11**(2): 167–194. doi:10.1007/s10346-013-0436-y.

IPCC. 1996. Climate Change 1995: The Science of Climate Change: Contribution of Working Group I to the Second Assessment Report of the Intergovernmental Panel on Climate Change. Cambridge University Press.

IPCC. 2013. Climate Change 2013: The Physical Science Basis. Contribution of Working Group I to the Fifth Assessment Report of the Intergovernmental Panel on Climate Change. Cambridge University Press.

ITASCA Consulting Group, Inc. 2017. 2D geomechanical & geotechnical continuum numerical modeling software, Itasca Consulting Group. Available from http://www.itascacg.com/software/flac [accessed 29 July 2017].

Kim, J., Jeong, S., and Regueiro, R.A. 2012. Instability of partially saturated soil slopes due to alteration of rainfall pattern. Engineering Geology, **147**: 28–36.

Leao, S. 2014. Mapping 100 Years of Thornthwaite Moisture Index: Impact of Climate Change in Victoria, Australia. Geographical Research, **52**(3): 309–327. doi:10.1111/1745-5871.12072.

Lu, N., Godt, J.W., and Wu, D.T. 2010. A closed-form equation for effective stress in unsaturated soil. Water Resources Research, **46**(5). Available from http://onlinelibrary.wiley.com/doi/10.1029/2009WR008646/full [accessed 27 July 2016].

Lu, N., and Likos, W.J. 2006. Suction Stress Characteristic Curve for Unsaturated Soil. Journal of Geotechnical and Geoenvironmental Engineering, **132**(2): 131–142. doi:10.1061/(ASCE)1090-0241(2006)132:2(131).

Malek, E. 1987. Comparison of alternative methods for estimating ETp and evaluation of advection in the Bajgah area, Iran. Agricultural and Forest Meteorology, **39**(2): 185–192. doi:10.1016/0168-1923(87)90036-0.

McCabe, G.J., and Wolock, D.M. 1992. Effects of climatic change and climatic variability on the Thornthwaite moisture index in the Delaware River basin. Climatic Change, **20**(2): 143–153. doi:10.1007/BF00154172.

Mekis, É., and Vincent, L.A. 2011. An Overview of the Second Generation Adjusted Daily Precipitation Dataset for Trend Analysis in Canada. Atmosphere-Ocean, **49**(2): 163–177. doi:10.1080/07055900.2011.583910.

Montgomery, D.R., and Dietrich, W.E. 1994. A physically based model for the topographic control on shallow landsliding. Water resources research, **30**(4): 1153–1171.

MTO. 2017. IDF Curve Look-up - Ministry of Transportation, Ontario. Available from http://www.mto.gov.on.ca/IDF_Curves/terms.shtml [accessed 30 May 2017].

Mualem, Y. 1976. A new model for predicting the hydraulic conductivity of unsaturated porous media. Water resources research, **12**(3): 513–522.

Natural Resources Canada. 2014. An overview of Canada's changing climate. Natural Resources Canada, Canada. Available from http://www.nrcan.gc.ca/environment/resources/publications/impacts-adaptation/reports/assessments/2014/16309 [accessed 7 September 2016].

Neuman, S.P., Feddes, R.A., Bresler, E., and others. 1974. Finite element simulation of flow in saturated-unsaturated soils considering water uptake by plants. Available from http://agris.fao.org/agris-search/search.do?recordID=US201300536275.

OCCP. 2017. Ontario Climate Change Projections. Available from http://www.lamps.yorku.ca/ [accessed 22 January 2017].

PC-Progress. 2014. HYDRUS slope stability module user manual. PC-PROGRESS. Available from https://www.pc-progress.com/en/Default.aspx?h3d2-Slope [accessed 21 February 2017].

Pelton, W.L., King, K.M., and Tanner, C.B. 1960. An Evaluation of the Thornthwaite and Mean Temperature Methods for Determining Potential Evapotranspiration. Agronomy Journal, **52**(7): 387–395. doi:10.2134/agronj1960.00021962005200070006x.

Penman, H.L. 1948. Natural evaporation from open water, bare soil and grass. *In* Proceedings of the Royal Society of London A: Mathematical, Physical and Engineering Sciences. The Royal Society. pp. 120–145. Available from http://rspa.royalsocietypublishing.org/content/royprsa/193/1032/120.full.pdf [accessed 27 December 2016].

Pereira, A.R., and Pruitt, W.O. 2004. Adaptation of the Thornthwaite scheme for estimating daily reference evapotranspiration. Agricultural Water Management, **66**(3): 251–257. doi:10.1016/j.agwat.2003.11.003.

Pk, S., and Beddoe, R. 2016. Influence of the soil-atmospheric boundary conditions on slope stability analyses. *In* 69th Annual Canadian Geotechnical Conference. Canadian Geotechnical Society, Vancouver. p. 262.

Pruitt, W.O., and Doorenbos, J. 1977. Empirical calibration, a requisite for evapotranspiration formulae based on daily or longer mean climate data? International Commission on Irrigation and Drainage, Budapest, Hungary. p. 20.

Rahardjo, H., Nio, A.S., Leong, E.C., and Song, N.Y. 2010. Effects of groundwater table position and soil properties on stability of slope during rainfall. Journal of Geotechnical and Geoenvironmental Engineering, **136**(11): 1555–1564.

Rahardjo, H., Satyanaga, A., and Leong, E.-C. 2013. Effects of flux boundary conditions on pore-water pressure distribution in slope. Engineering Geology, **165**: 133–142.

Rajkai, K., and Várallyay, G. 1989. Estimating soil water retention from simpler properties by regression techniques. Riverside, CA. pp. 11–13.

Rawls, W.J., Brakensiek, D.L., and Saxtonn, K.E. 1982. Estimation of Soil Water Properties. Transactions of the ASAE, **25**(5): 1316–1320. doi:10.13031/2013.33720.

Rawls, W.J., Brakensiek, D.L., and Soni, B. 1983. Agricultural Management Effects on Soil Water Processes Part I: Soil Water Retention and Green and Ampt Infiltration Parameters. Transactions of the ASAE, **26**(6): 1747–1752. doi:10.13031/2013.33837.

Richards, L. 1931. Capillary conduction of liquids through porous mediums. Physics, **1**(5): 318–333. doi:10.1063/1.1745010.

Robinson, J.D., Vahedifard, F., and AghaKouchak, A. 2017. Rainfall-triggered slope instabilities under a changing climate: comparative study using historical and projected precipitation extremes. Canadian Geotechnical Journal, **54**: 117–127. doi:10.1139/cgj-2015-0602.

Rouainia, M., Davies, O., O'Brien, T., and Glendinning, S. 2009. Numerical modelling of climate effects on slope stability. Proceedings of the ICE-Engineering Sustainability, **162**(2): 81–89.

Rushton, K.R. 2004. Groundwater hydrology: conceptual and computational models. John Wiley & Sons Ltd. [accessed 21 May 2017].

Schaap, M.G., Leij, F.J., and van Genuchten, M.T. 2001. Rosetta: a computer program for estimating soil hydraulic parameters with hierarchical pedotransfer functions. Journal of Hydrology, **251**(3–4): 163–176. doi:10.1016/S0022-1694(01)00466-8.

Schmidt, J., and Dikau, R. 2004. Modeling historical climate variability and slope stability. Geomorphology, **60**(3–4): 433–447. doi:10.1016/j.geomorph.2003.11.001.

Šimůnek, J., van Genuchten, M.T., and Šejna, M. 2016. Recent developments and applications of the HYDRUS computer software packages. Vadose Zone Journal, **15**(7).

SRK Consulting Inc. 2010. Olympic dam rock storage facility: assesment of infiltration and percolation. SRK Consulting Inc., Vancouver, BC.

Stanhill, G. 1961. A comparison of methods of calculating potential evapotranspiration from climatic data. Israel J. Agric. Res, **11**(3–4): 159–171.

Tabari, H., and Hosseinzadeh Talaee, P. 2013. Moisture index for Iran: Spatial and temporal analyses. Global and Planetary Change, **100**: 11–19. doi:10.1016/j.gloplacha.2012.08.010.

Thornthwaite, C.W. 1948. An Approach toward a Rational Classification of Climate. Geographical Review, **38**(1): 55–94. doi:10.2307/210739.

Thornthwaite, C.W., and Hare, F.K. 1955. Climatic classification in forestry. Unasylva, **9**(2): 51–59.

Thornthwaite, C.W., and Mather, J.R. 1955. The Water Balance. Centerton, Drexel Institute of Technology-Laboratory of Climatology, 104p. Publications in climatology, **8**(1).

Tindall, J.A., Kunkel, J.R., Anderson, D.E., and others. 1999. Unsaturated zone hydrology for scientists and engineers. Prentice Hall. [accessed 21 May 2017].

Tomasella, J., and Hodnett, M.G. 1998. Estimating soil water retention characteristics from limited data in Brazilian Amazonia. Soil science, **163**(3): 190–202.

Tratch, D.J. 1995, September. A Geotechnical Engineering Approach to Plant Transpiration and Root Water Uptake. Thesis. Available from https://ecommons.usask.ca/handle/10388/7605 [accessed 21 May 2017].

Vahedifard, F., Tehrani, F.S., Galavi, V., Ragno, E., and AghaKouchak, A. 2017. Resilience of MSE Walls with Marginal Backfill under a Changing Climate: Quantitative Assessment for Extreme Precipitation Events. Journal of Geotechnical and Geoenvironmental Engineering, **143**(9). doi:10.1061/(ASCE)GT.1943-5606.0001743.

van Genuchten, M.T. 1980. A closed-form equation for predicting the hydraulic conductivity of unsaturated soils. Soil science society of America journal, **44**(5): 892–898.

Vanapalli, S.K., Fredlund, D.G., Pufahl, D.E., and Clifton, A.W. 1996. Model for the prediction of shear strength with respect to soil suction. Canadian Geotechnical Journal, **33**(3): 379–392. doi:10.1139/t96-060.

Vardon, P.J. 2015. Climatic influence on geotechnical infrastructure: a review. Environmental Geotechnics, **2**(3): 166–174. doi:10.1680/envgeo.13.00055.

Vereecken, H., Maes, J., Feyen, J., and Darius, P. 1989. Estimating the soil moisture retention characteristic from texture, bulk density, and carbon content. Soil science, **148**(6): 389–403.

Vincent, L.A., and Mekis, E. 2006. Changes in daily and extreme temperature and precipitation indices for Canada over the twentieth century. Atmosphere-Ocean, **44**(2): 177–193.

Vincent, L.A., Wang, X.L., Milewska, E.J., Wan, H., Yang, F., and Swail, V. 2012. A second generation of homogenized Canadian monthly surface air temperature for climate trend analysis. Journal of Geophysical Research: Atmospheres, **117**(D18): D18110. doi:10.1029/2012JD017859.

Vuuren, D.P. van, Edmonds, J., Kainuma, M., Riahi, K., Thomson, A., Hibbard, K., Hurtt, G.C., Kram, T., Krey, V., Lamarque, J.-F., Masui, T., Meinshausen, M., Nakicenovic, N., Smith, S.J., and Rose, S.K. 2011. The representative concentration pathways: an overview. Climatic Change, **109**(1–2): 5. doi:10.1007/s10584-011-0148-z.

Wang, X., Huang, G., and Liu, J. 2014. Projected increases in intensity and frequency of rainfall extremes through a regional climate modeling approach. Journal of Geophysical Research: Atmospheres, **119**(23). Available from http://onlinelibrary.wiley.com/doi/10.1002/2014JD022564/full [accessed 21 April 2016].

Wayne, G.P. 2013. The beginner's guide to representative concentration pathways. skeptical science, **25**.

Whitfield, P.H., and Cannon, A.J. 2000. Recent Variations in Climate and Hydrology in Canada. Canadian Water Resources Journal / Revue canadienne des ressources hydriques, **25**(1): 19–65. doi:10.4296/cwrj2501019.

Wilson, G.W. 1990. Soil evaporative fluxes for geotechnical engineering problems. Available from http://ecommons.usask.ca/handle/10388/etd-07102008-083937 [accessed 20 February 2017].

Wilson, G.W. 1993. SoilCover, User's Manual for an Evaporative Flux Model. University of Saskatchewan, Saskatoon, SK.

Wilson, G.W., Fredlund, D.G., and Barbour, S.L. 1994. Coupled soil-atmosphere modelling for soil evaporation. Canadian Geotechnical Journal, **31**(2): 151–161.

Wilson, G.W., Fredlund, D.G., and Barbour, S.L. 1997. The effect of soil suction on evaporative fluxes from soil surfaces. Canadian Geotechnical Journal, **34**(1): 145–155.

Wösten, J.H.M., Lilly, A., Nemes, A., and Le Bas, C. 1999. Development and use of a database of hydraulic properties of European soils. Geoderma, **90**(3–4): 169–185. doi:10.1016/S0016-7061(98)00132-3.

Appendix

Results of The Trend Analyses of Future Precipitation, Temperature, Potential Evaporation, and Extreme Precipitation Events

Trend Analysis of Daily Precipitation Data

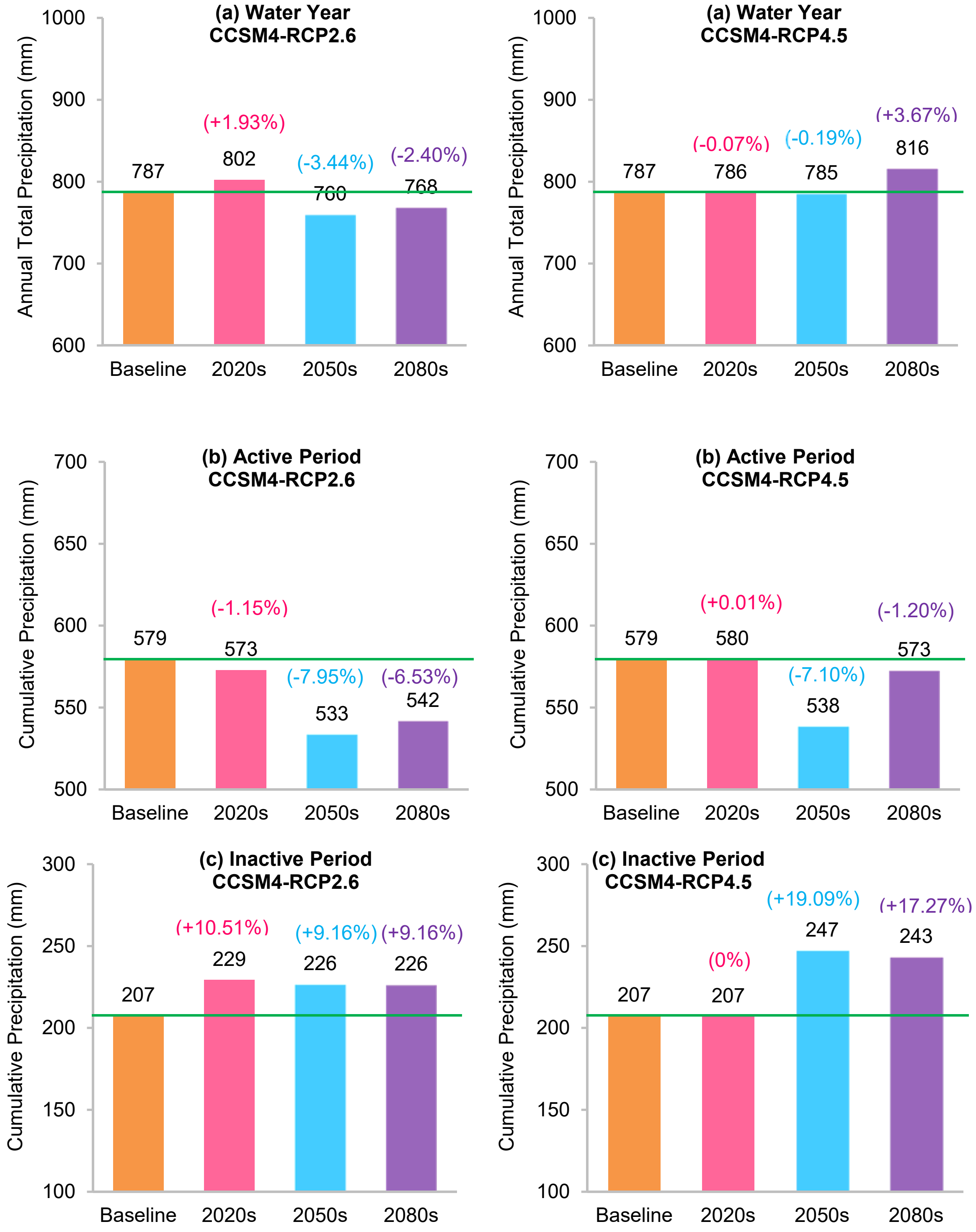

Figure A-1 Projected percentage change in cumulative precipitation over (a) water year (b) active period, and (c) inactive period for the RCP 2.6 and 4.5 of the CCSM4 model

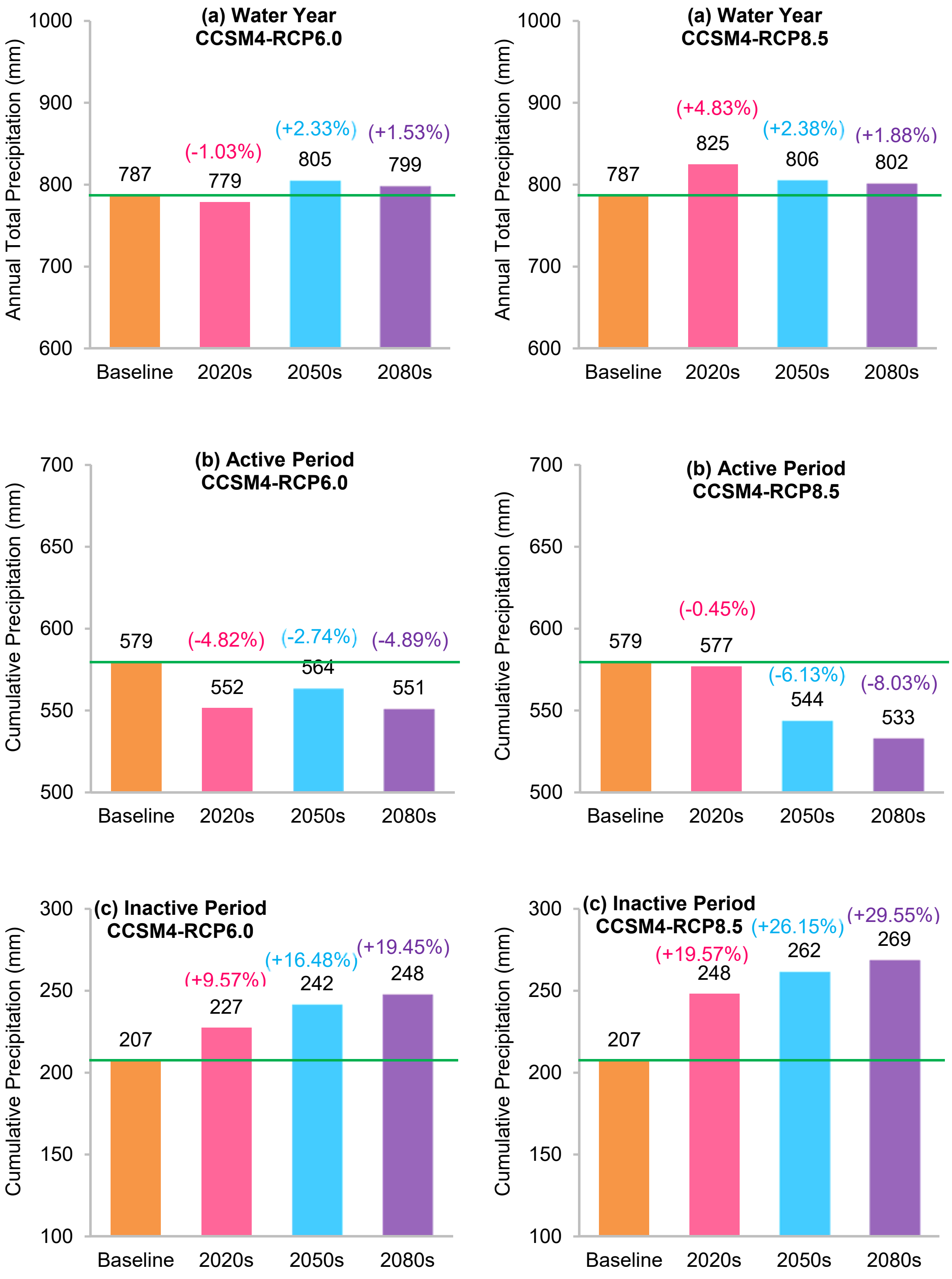

Figure A-2 Projected percentage change in cumulative precipitation over (a) water year (b) active period, and (c) inactive period for the RCP 6.0 and 8.5 of the CCSM4 model

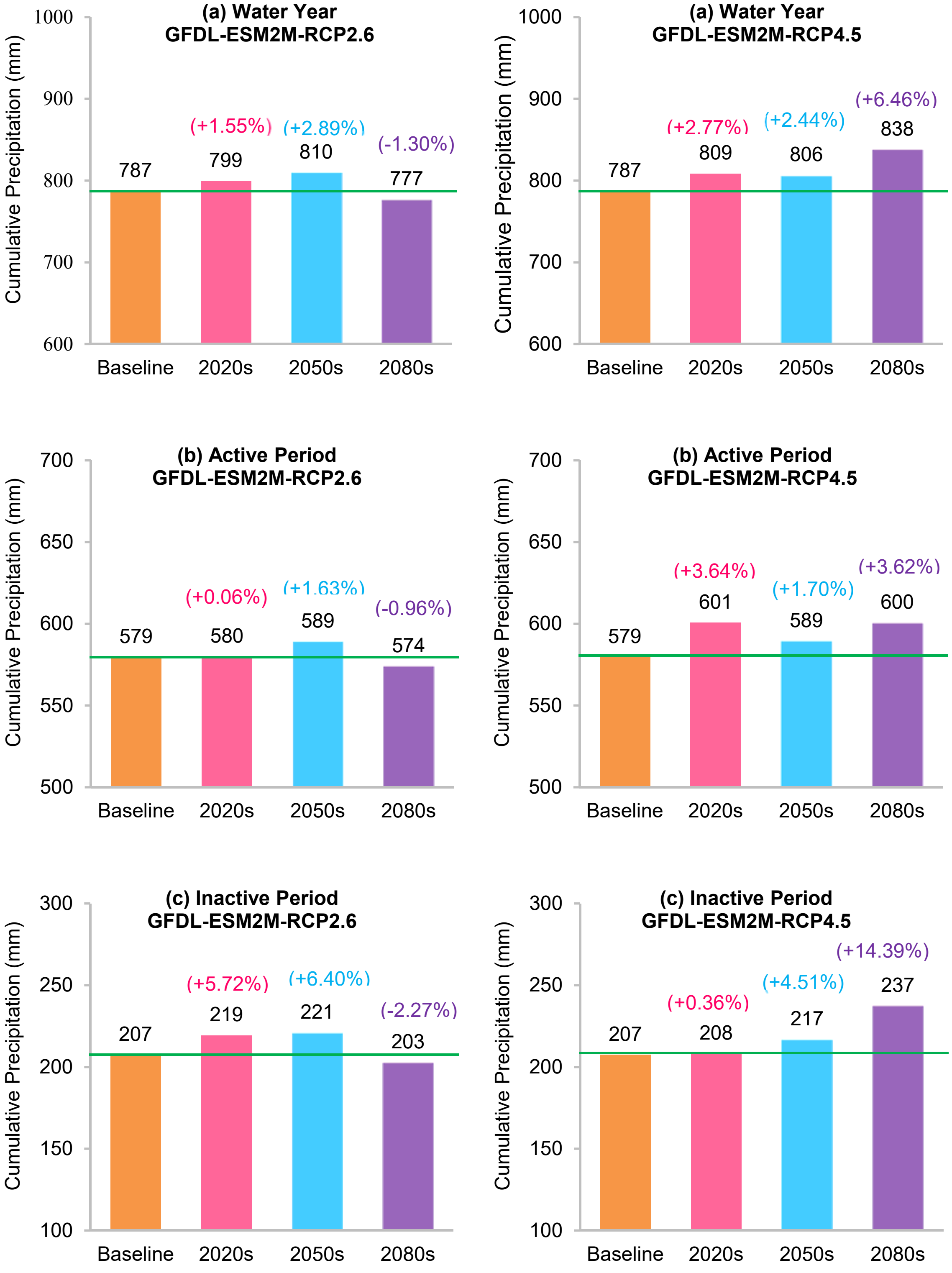

Figure A-3 Projected percentage change in cumulative precipitation over (a) water year (b) active period, and (c) inactive period for the RCP 2.6 and 4.5 of the GFDL-ESM2M model

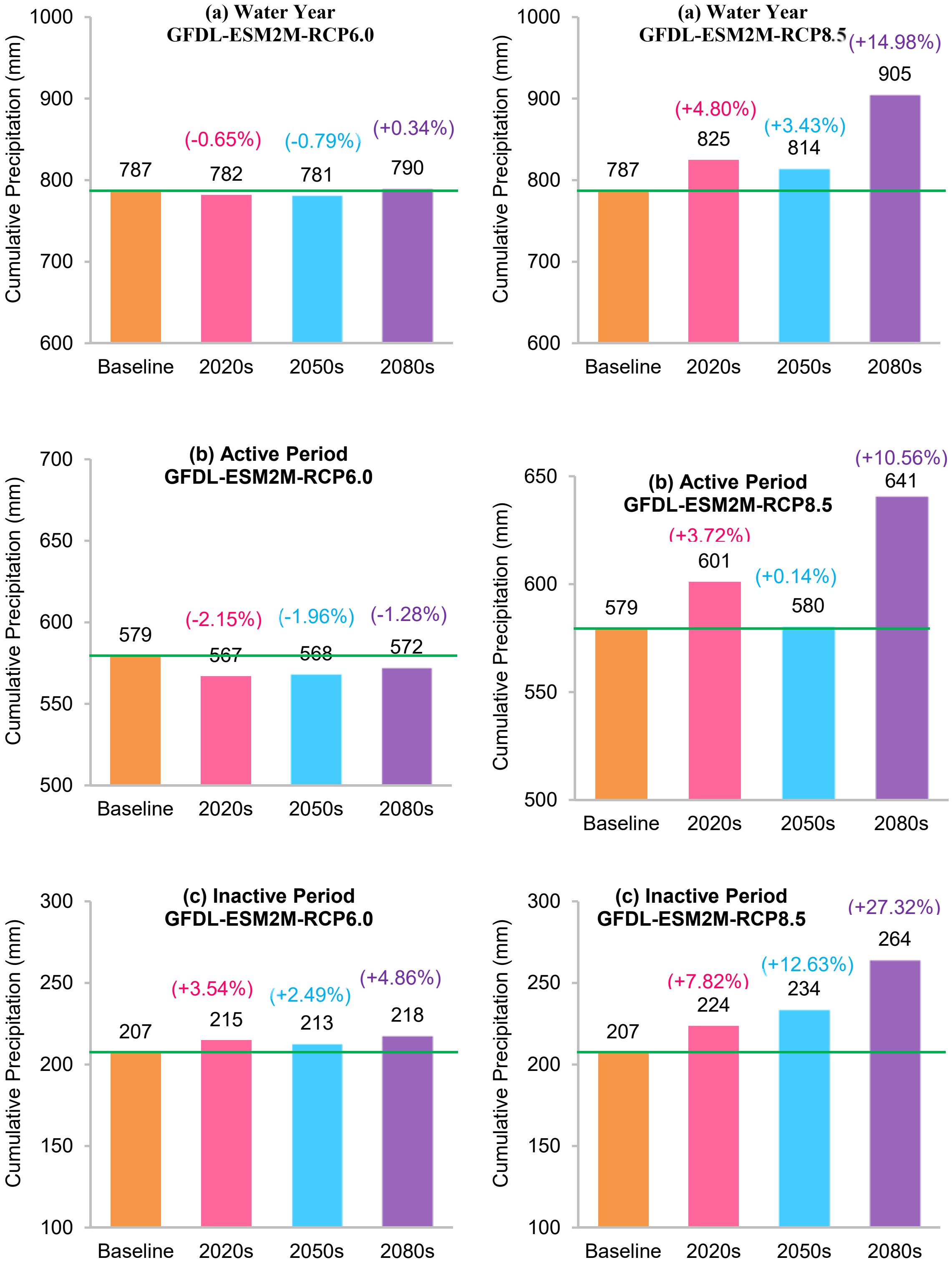

Figure A-4 Projected percentage change in cumulative precipitation over (a) water year (b) active period, and (c) inactive period for the RCP 6.0 and 8.5 of the GFDL-ESM2M model

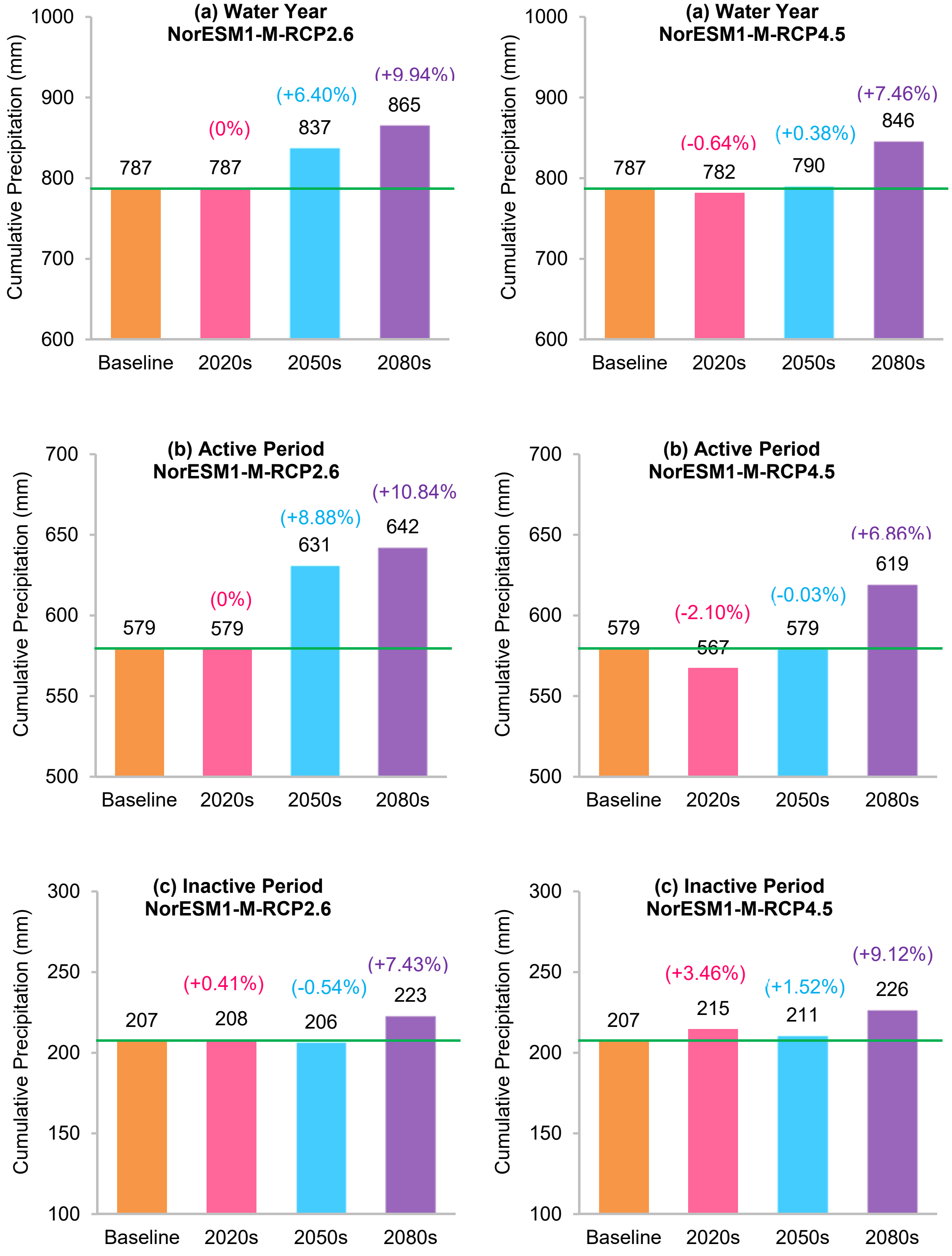

Figure A-5 Projected percentage change in cumulative precipitation over (a) water year (b) active period, and (c) inactive period for the RCP 2.6 and 4.5 of the NorESM1-M model

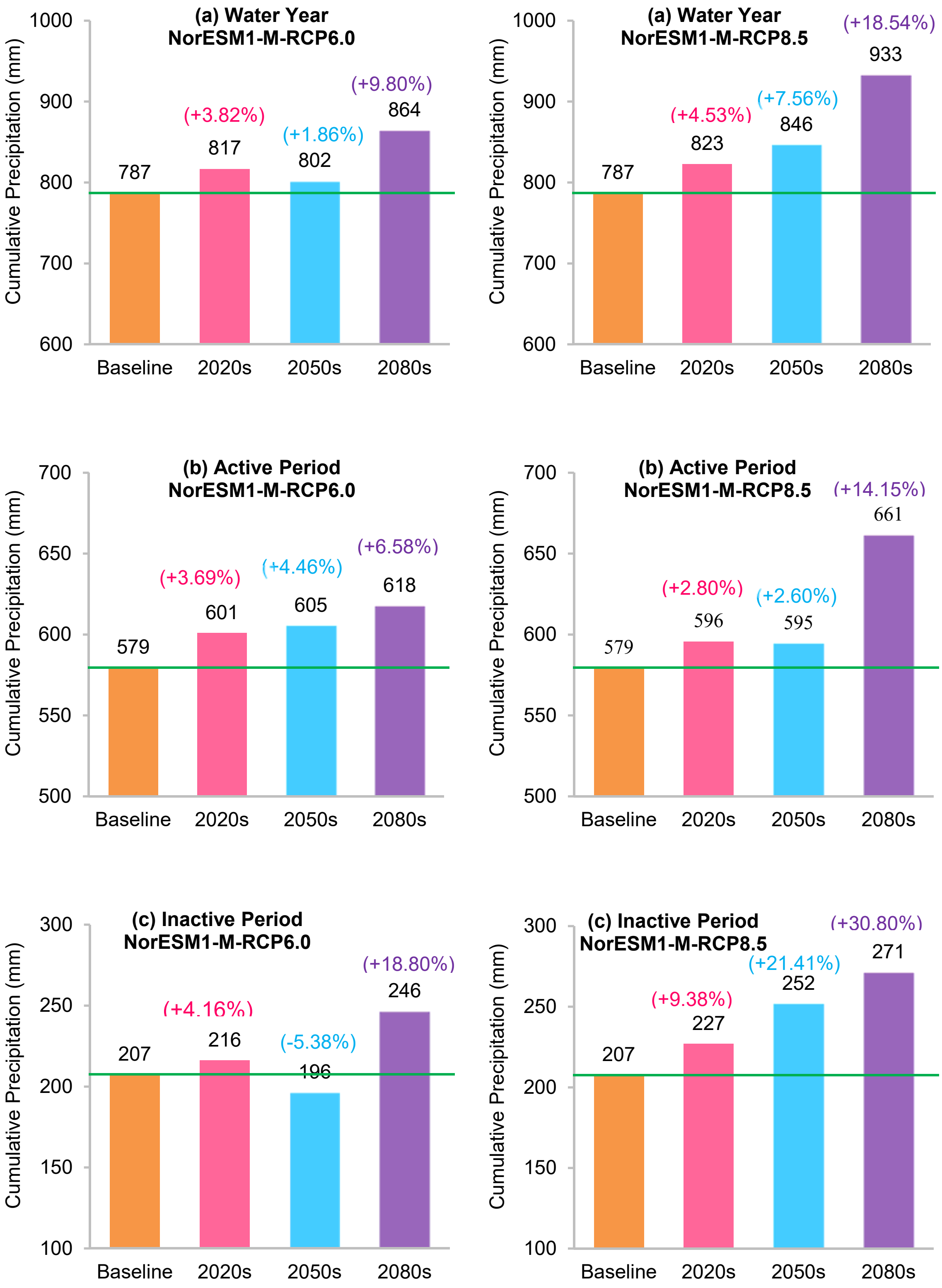

Figure A-6 Projected percentage change in cumulative precipitation over (a) water year (b) active period, and (c) inactive period for the RCP 6.0 and 8.5 of the NorESM1-M model

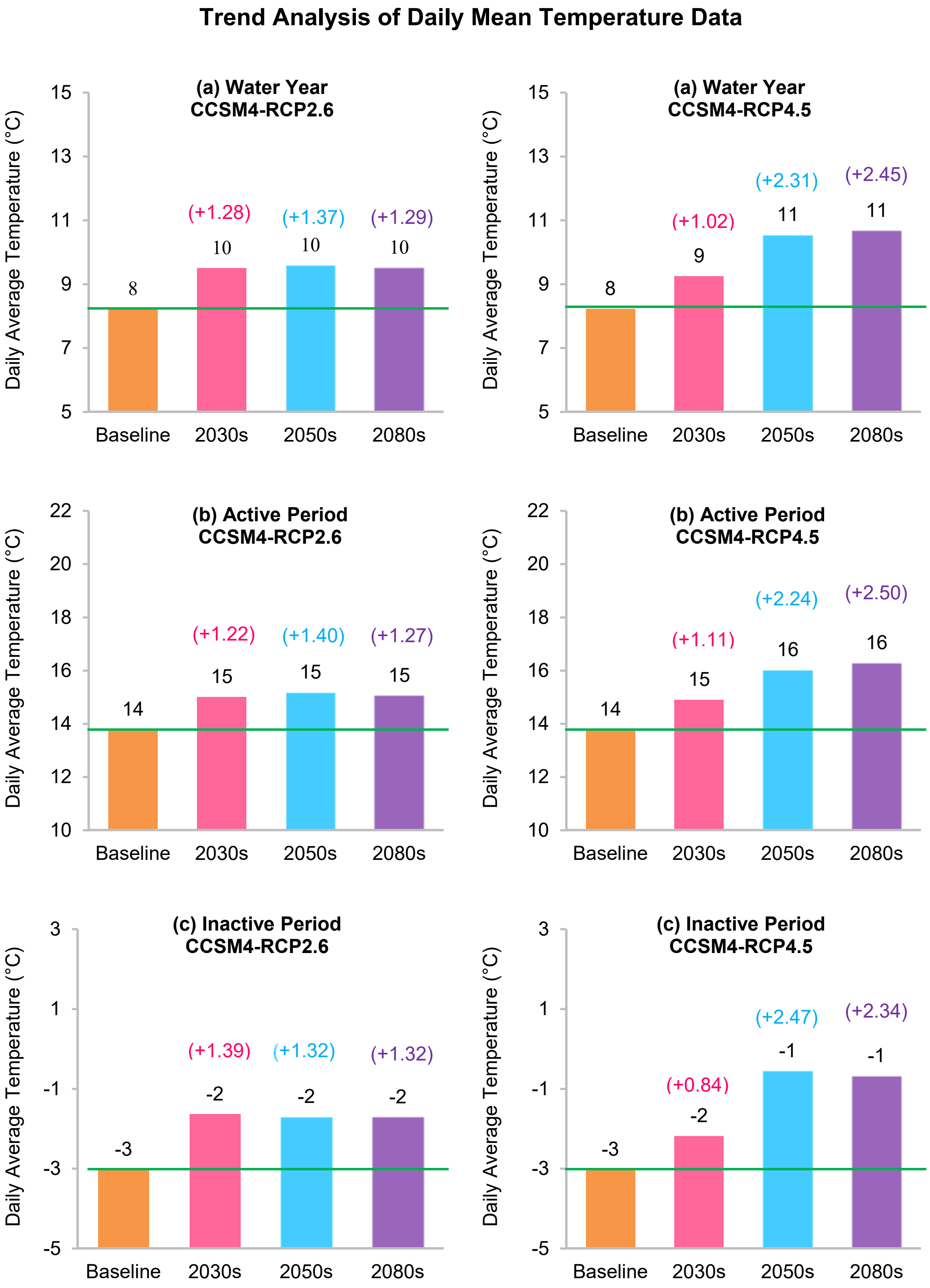

Figure A-7 Projected increase in daily mean temperature over (a) water year (b) active period, and (c) inactive period for the RCP 2.6 and 4.5 of the CCSM4 model

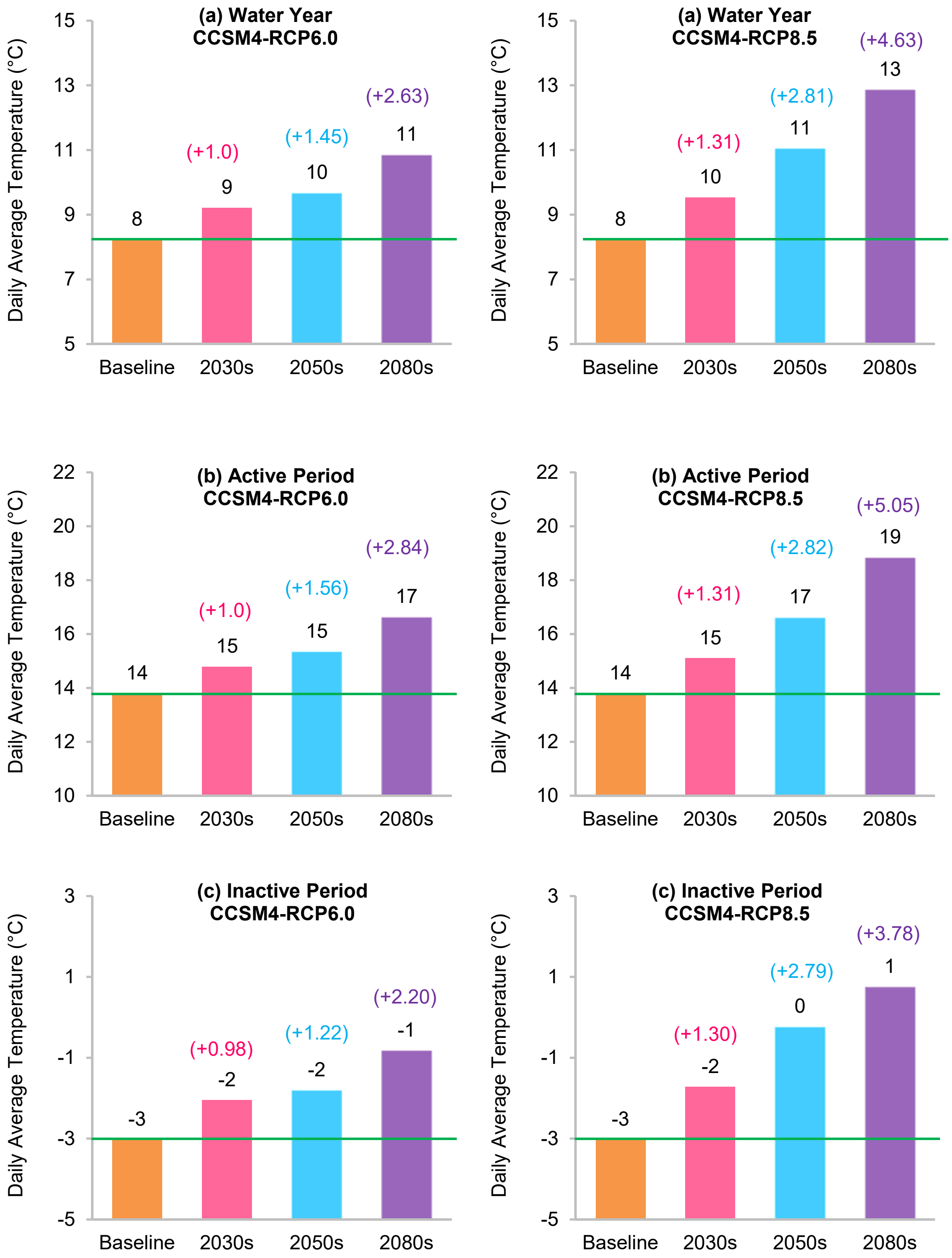

Figure A-8 Projected increase in daily mean temperature over (a) water year (b) active period, and (c) inactive period for the RCP 6.0 and 8.5 of the CCSM4 model

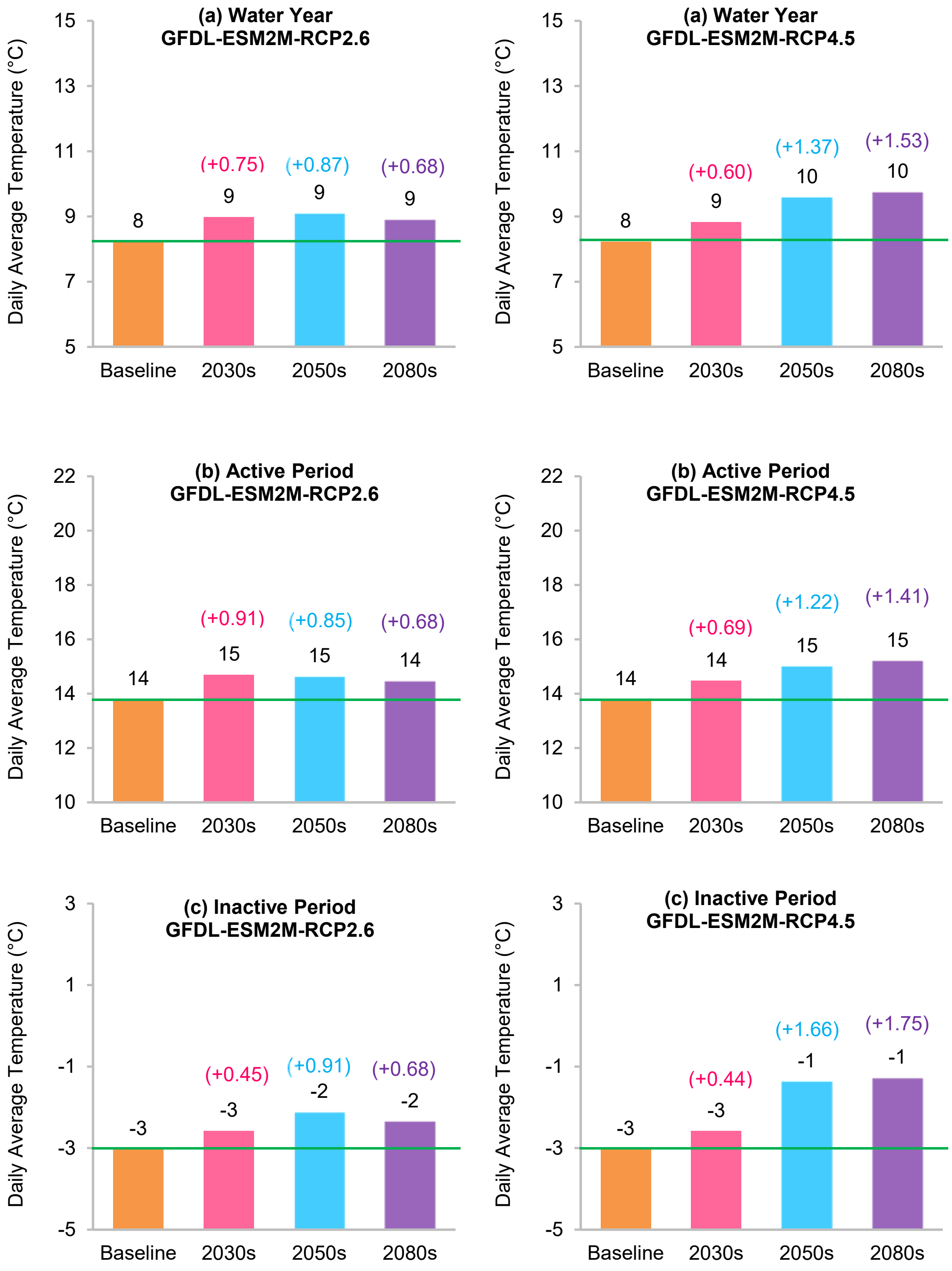

Figure A-9 Projected increase in daily mean temperature over (a) water year (b) active period, and (c) inactive period for the RCP 2.6 and 4.5 of the GFDL-ESM2M model

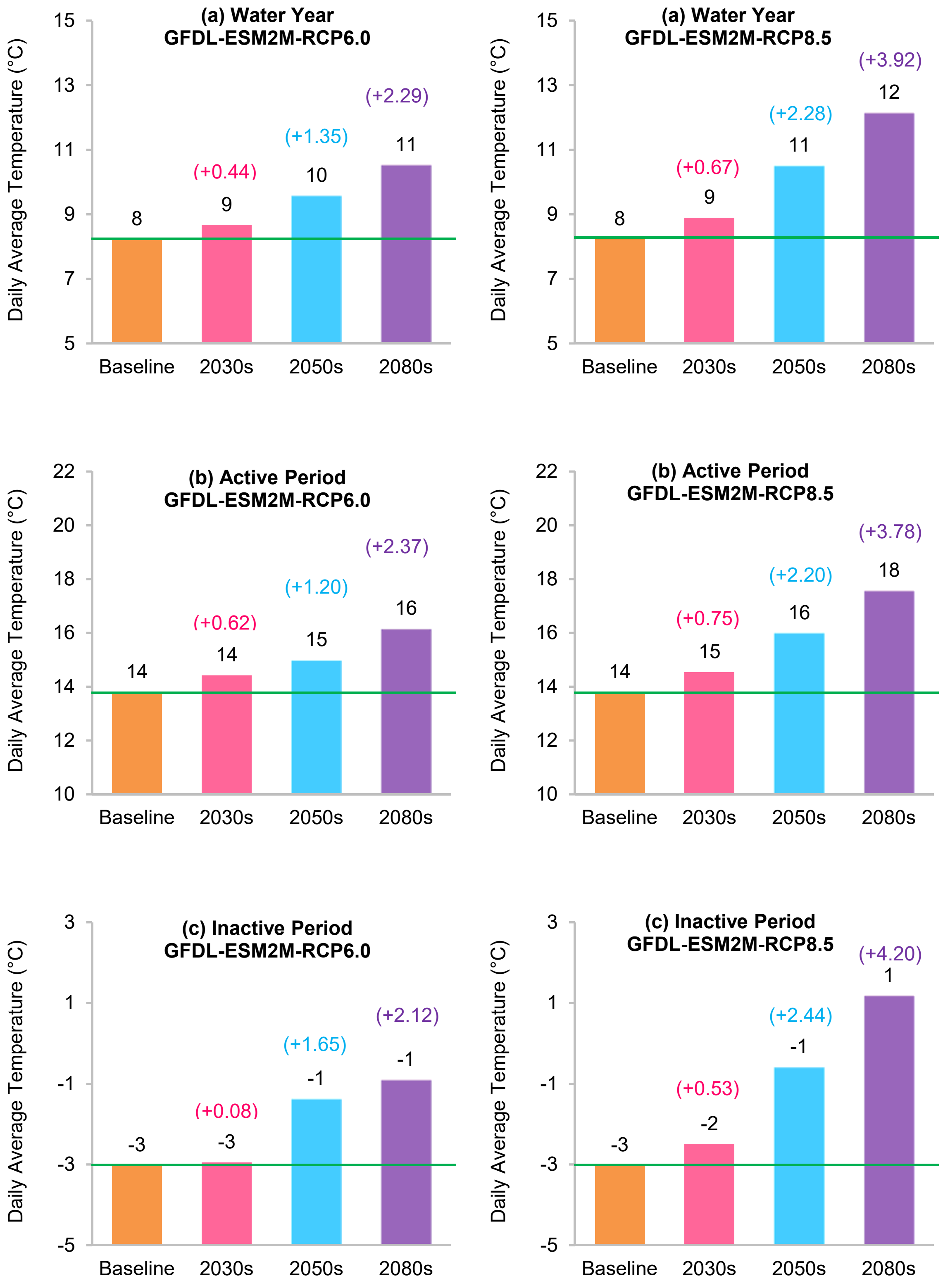

Figure A-10 Projected increase in daily mean temperature over (a) water year (b) active period, and (c) inactive period for the RCP 6.0 and 8.5 of the GFDL-ESM2M model

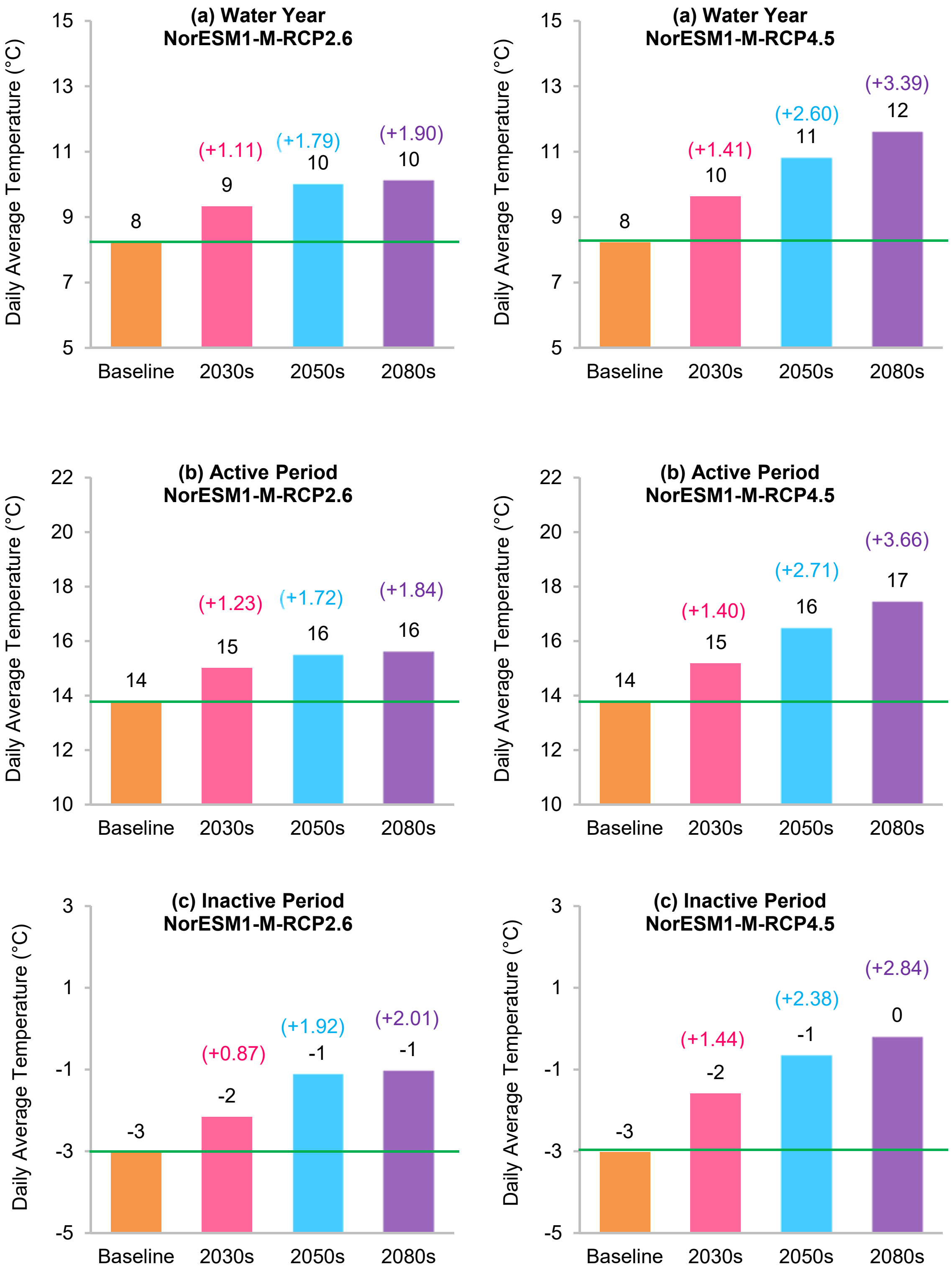

Figure A-11 Projected increase in daily mean temperature over (a) water year (b) active period, and (c) inactive period for the RCP 2.6 and 4.5 of the NorESM1-M model

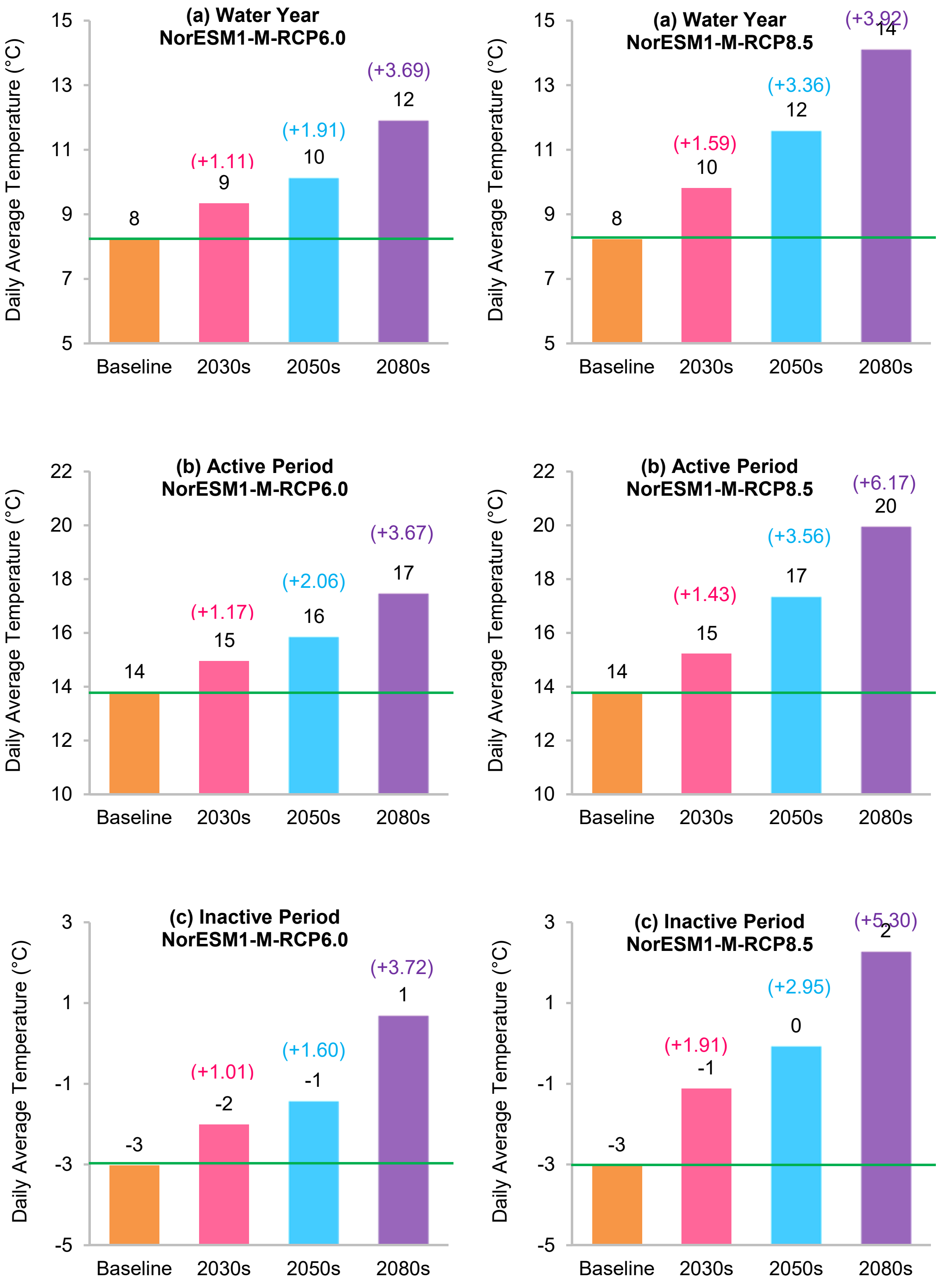

Figure A-12 Projected increase in daily mean temperature over (a) water year (b) active period, and (c) inactive period for the RCP 6.0 and 8.5 of the NorESM1-M model

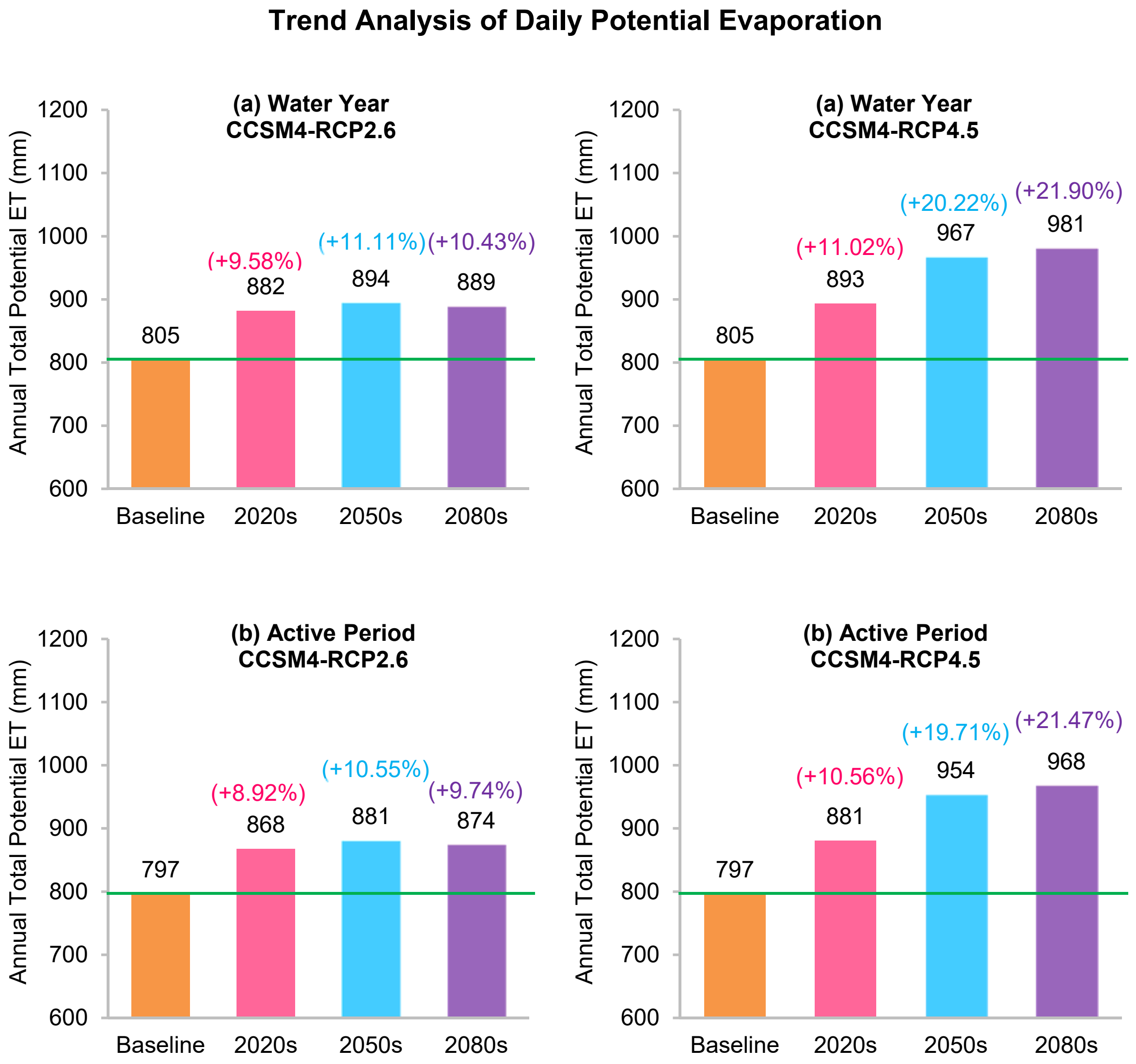

Figure A-13 Projected percentage change in PE over (a) water year, and (b) active period for the RCP 2.6 and 4.5 of the CCSM4 model

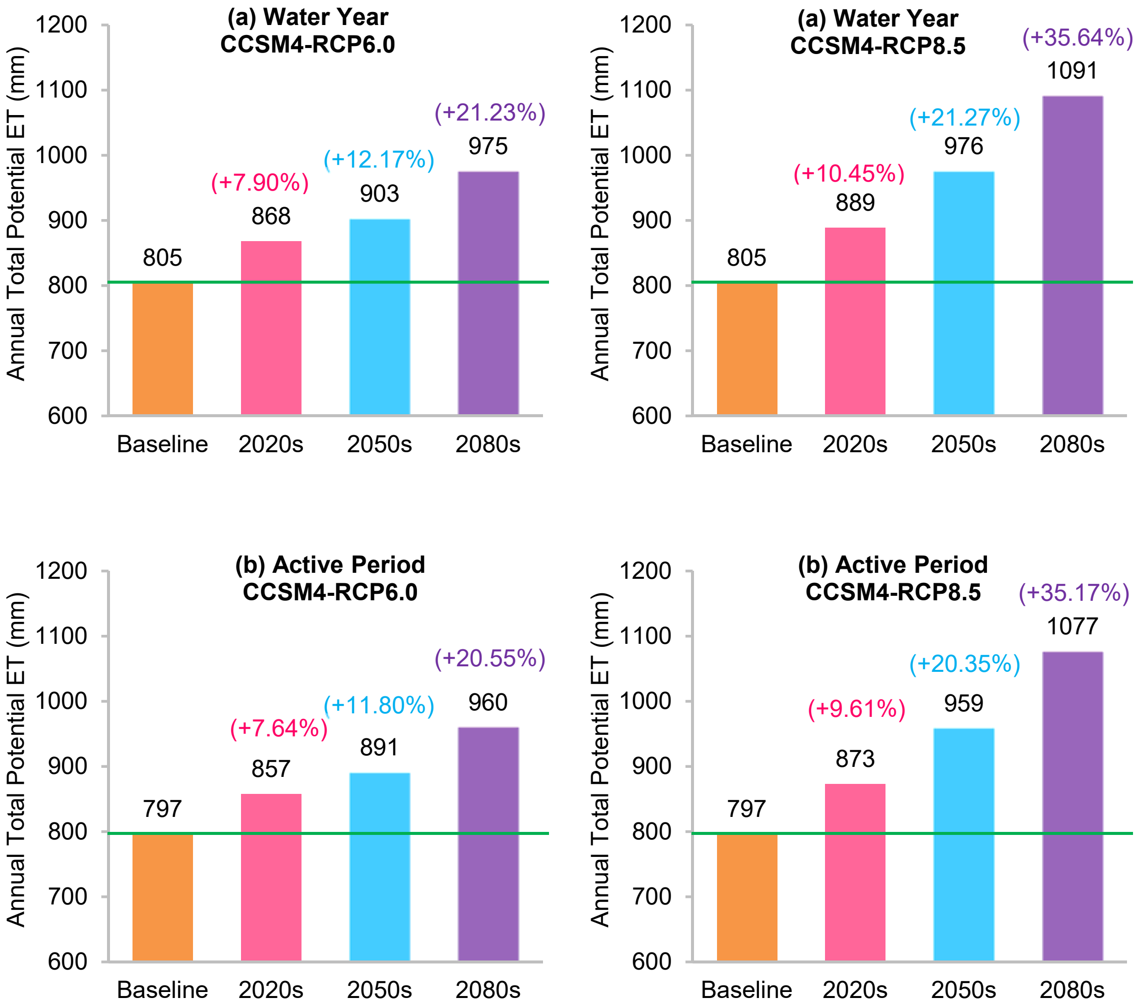

Figure A-14 Projected percentage change in PE over (a) water year, and (b) active period for the RCP 6.0 and 8.5 of the CCSM4 model

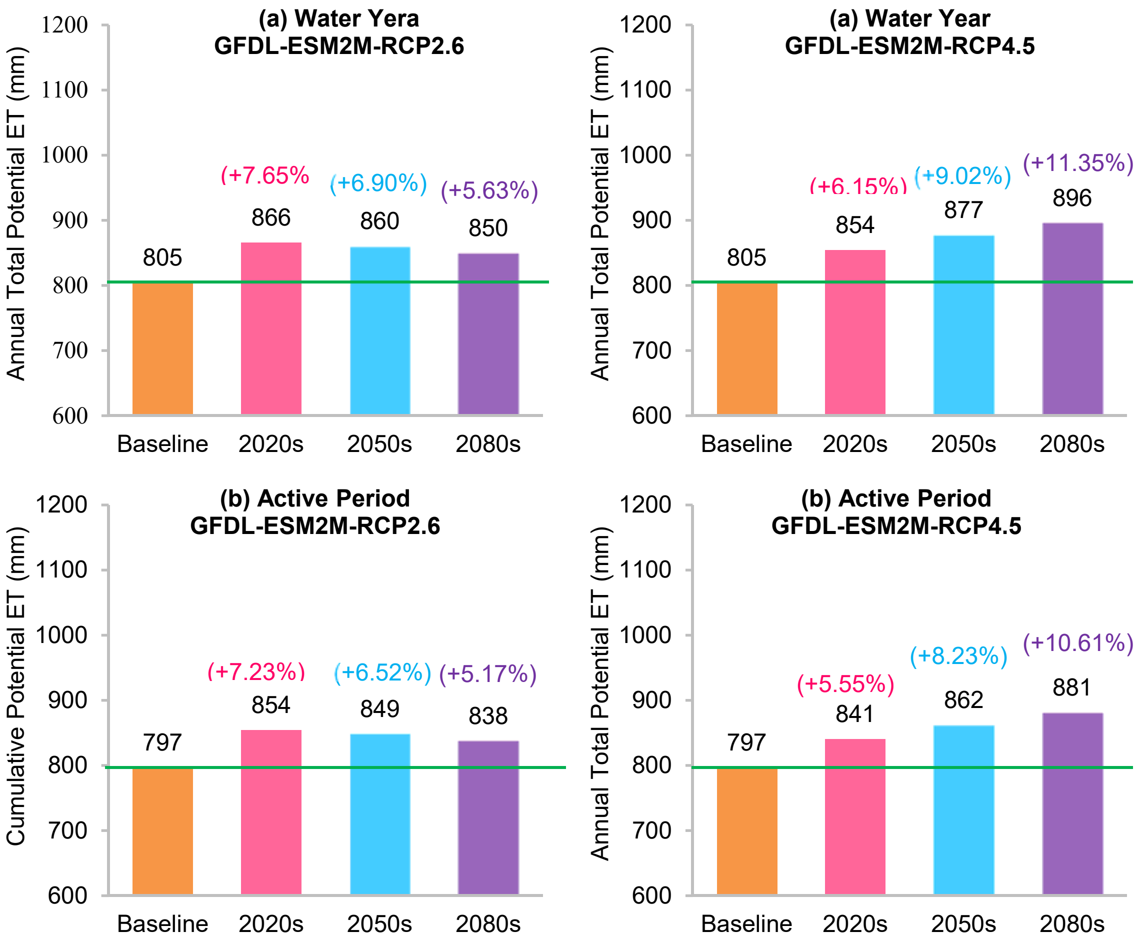

Figure A-15 Projected percentage change in PE over (a) water year, and (b) active period for the RCP 2.6 and 4.5 of the GFDL-ESM2M model

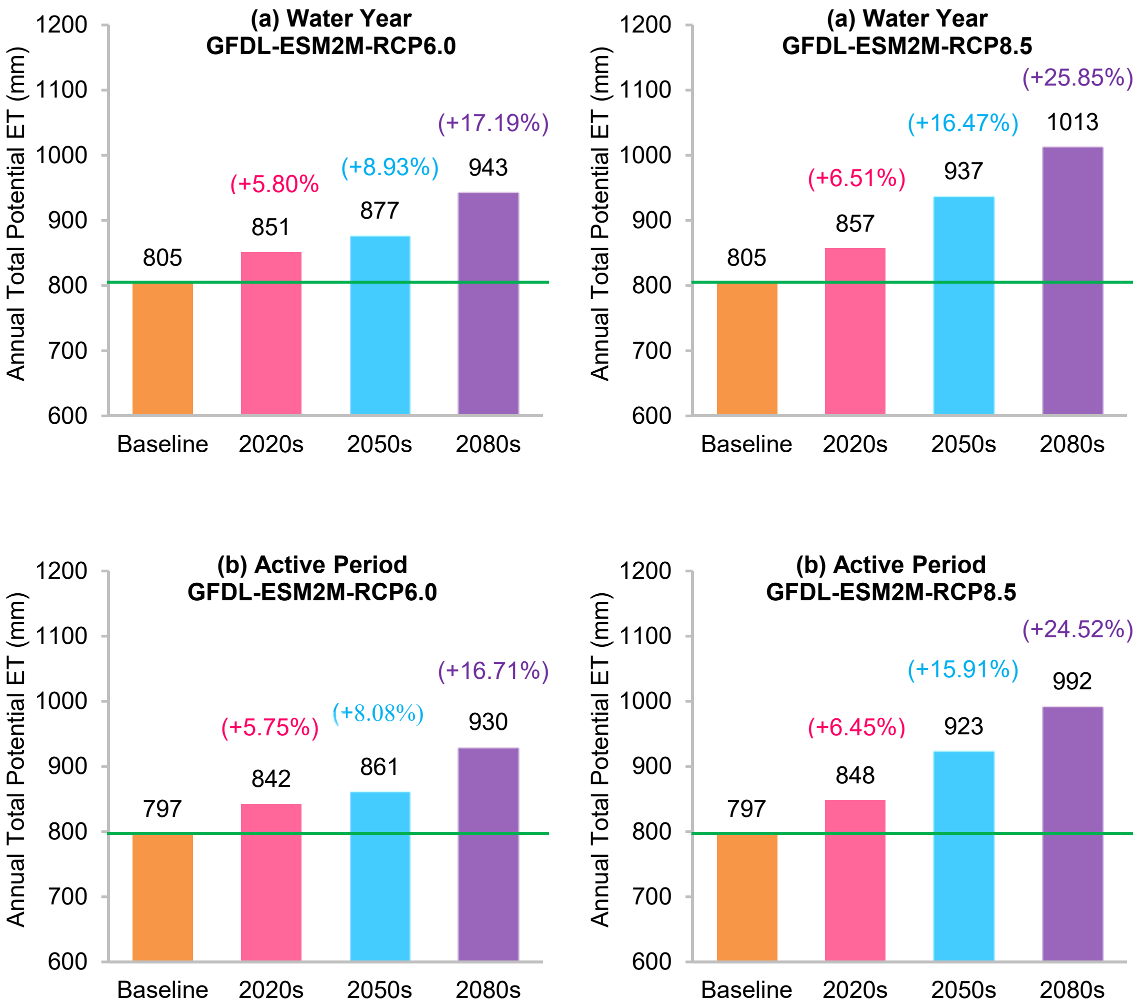

Figure A-16 Projected percentage change in PE over (a) water year, and (b) active period for the RCP 6.0 and 8.5 of the GFDL-ESM2M model

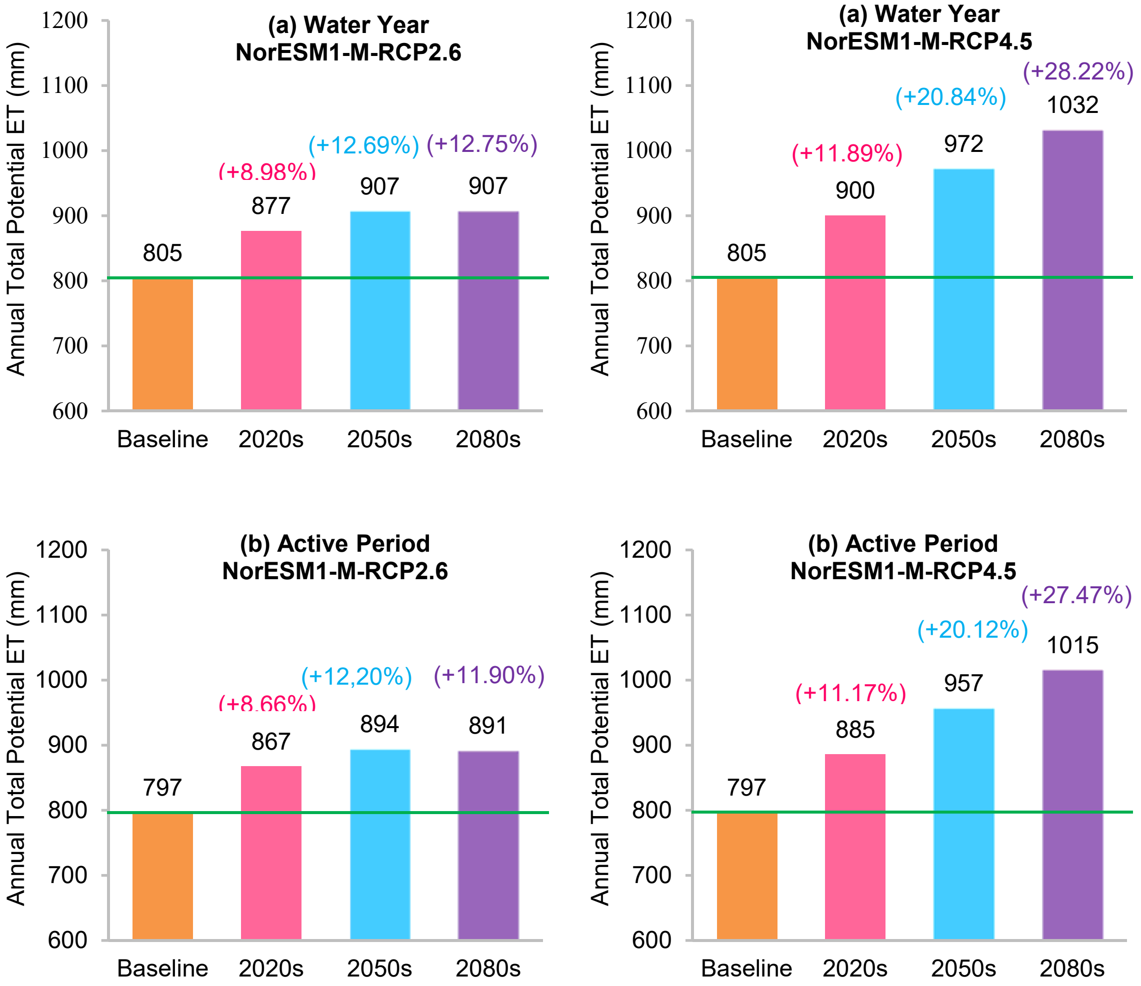

Figure A-17 Projected percentage change in PE over (a) water year, and (b) active period for the RCP 2.6 and 4.5 of the NorESM1-M model

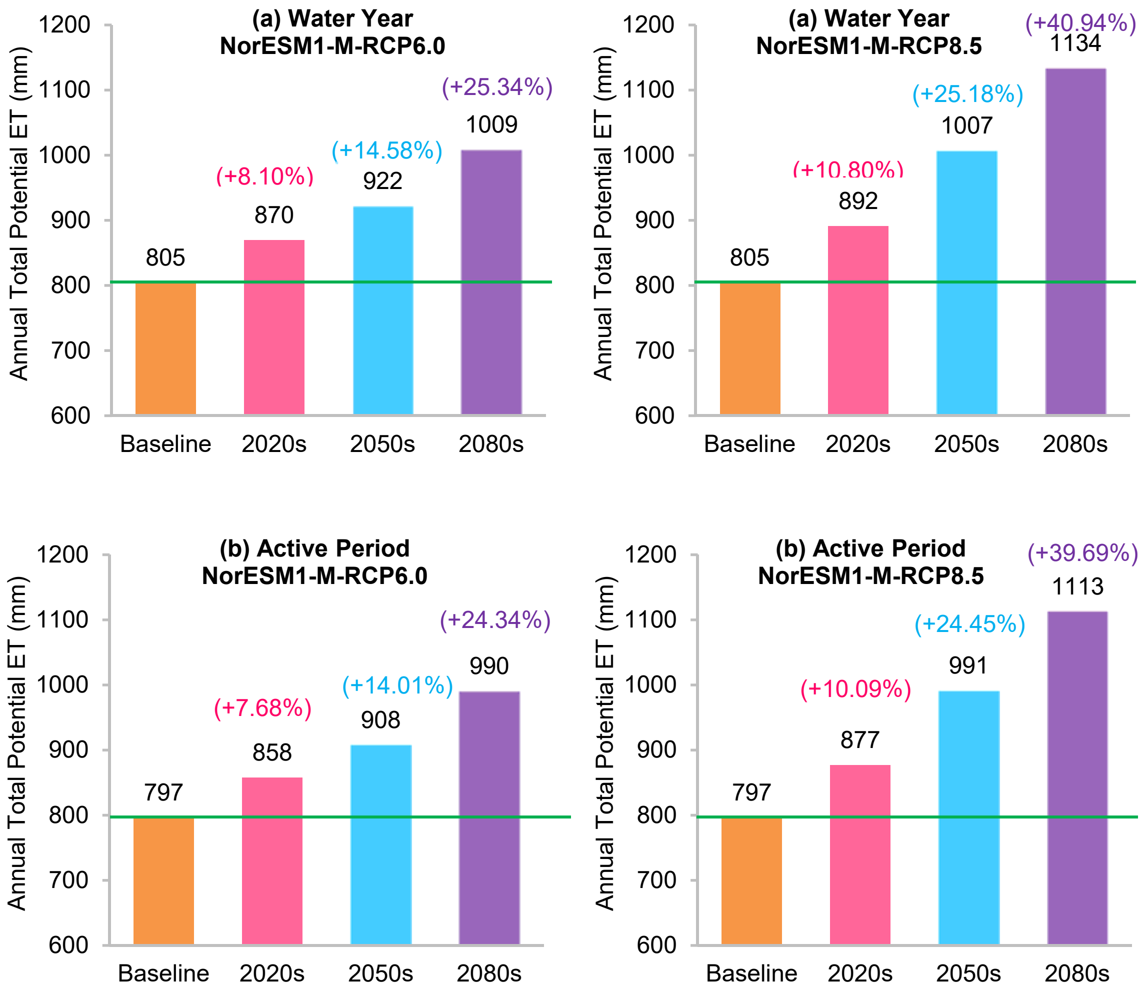

Figure A-18 Projected percentage change in PE over (a) water year, and (b) active period for the RCP 6.0 and 8.5 of the NorESM1-M model

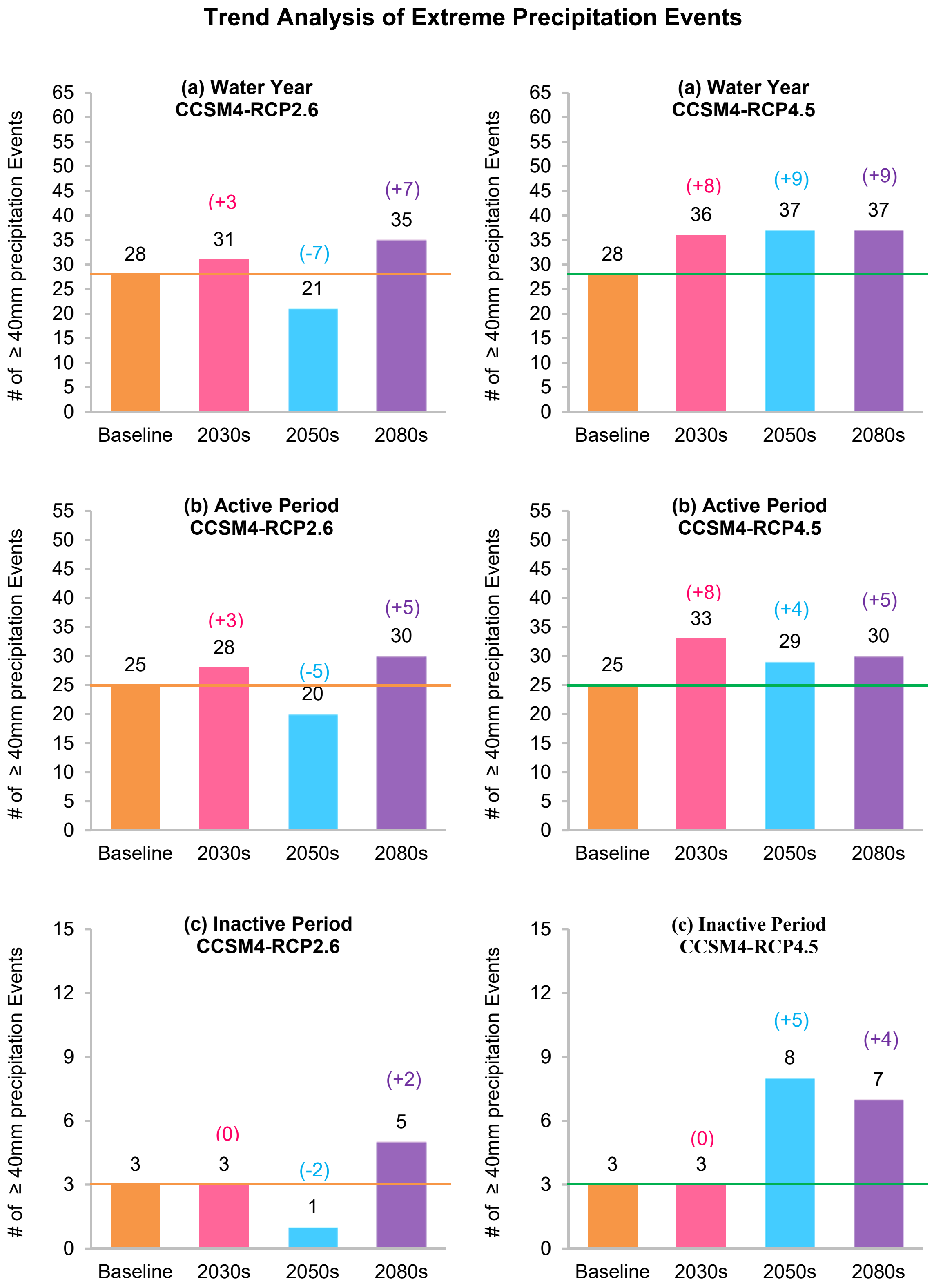

Trend Analysis of Extreme Precipitation Events

Figure A-19 Projected change in extreme precipitation events over (a) water year, (b) active period, and (c) inactive period for the RCP 2.6 and 4.5 of the CCSM4 model

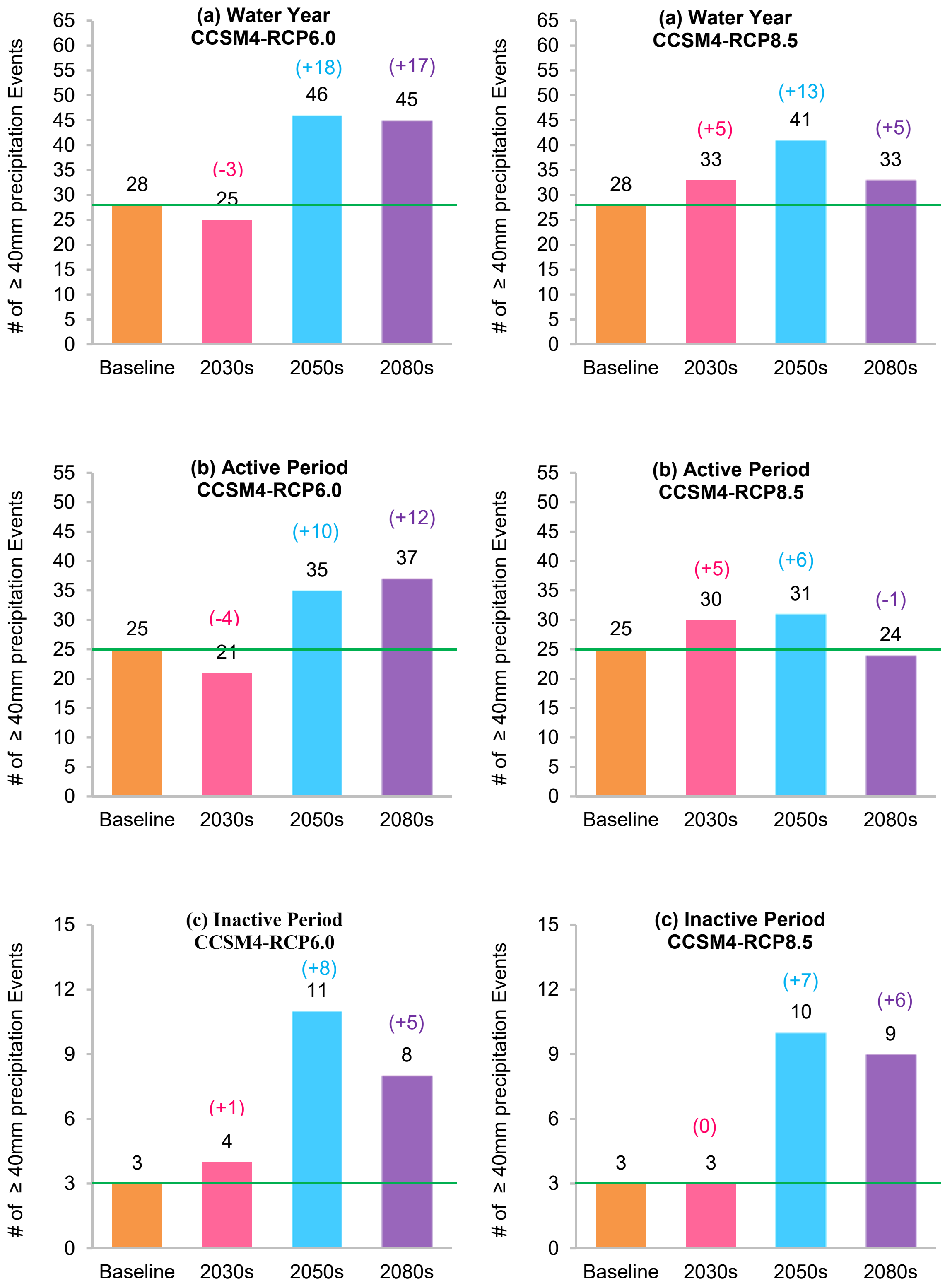

Figure A-20 Projected change in extreme precipitation over (a) water year, (b) active period, and (c) inactive period for the RCP 6.0 and 8.5 of the CCSM4 model

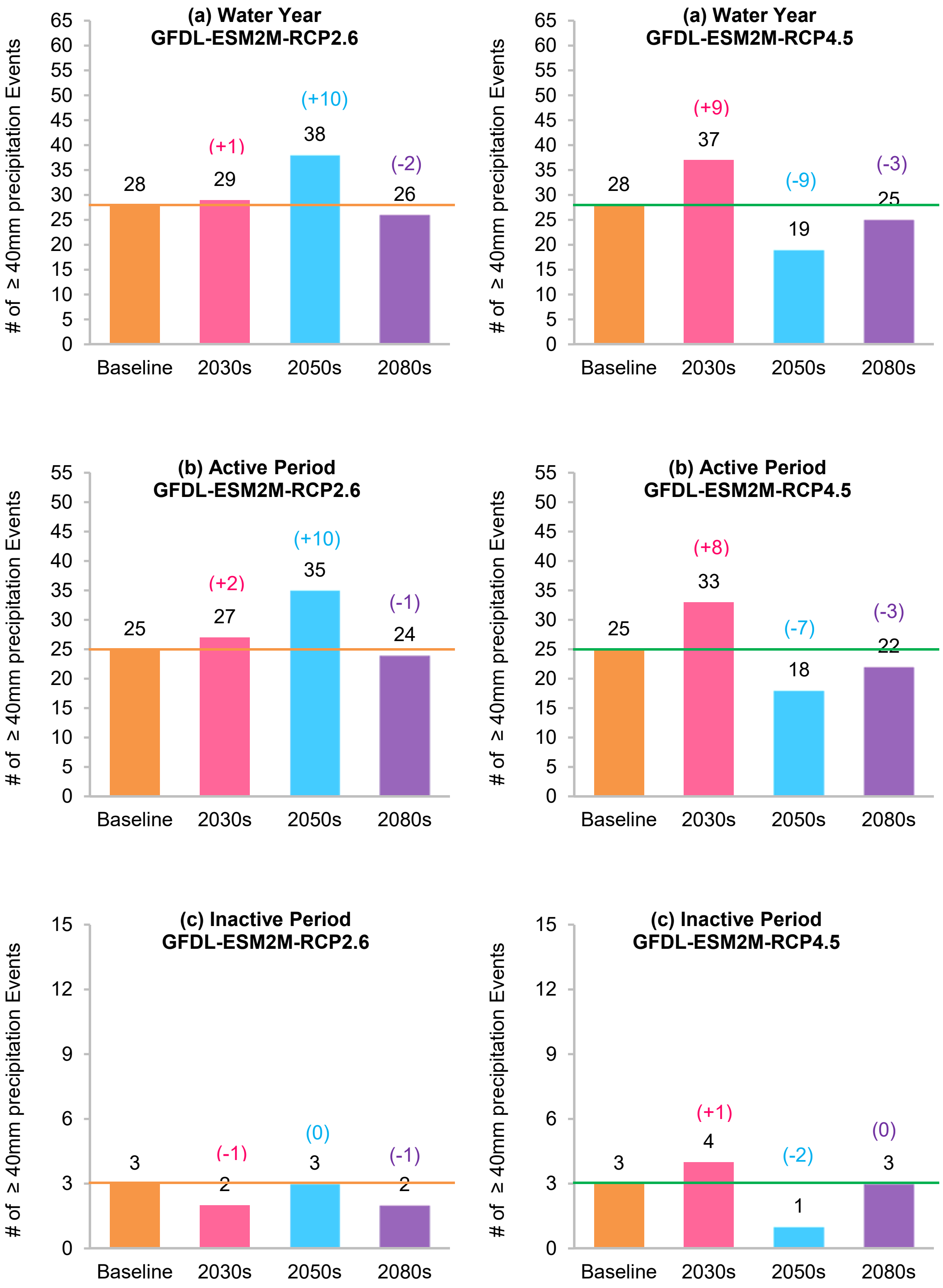

Figure A-21 Projected change in extreme precipitation events over (a) water year, (b) active period, and (c) inactive period for the RCP 2.6 and 4.5 of the GFDL-ESM2M model

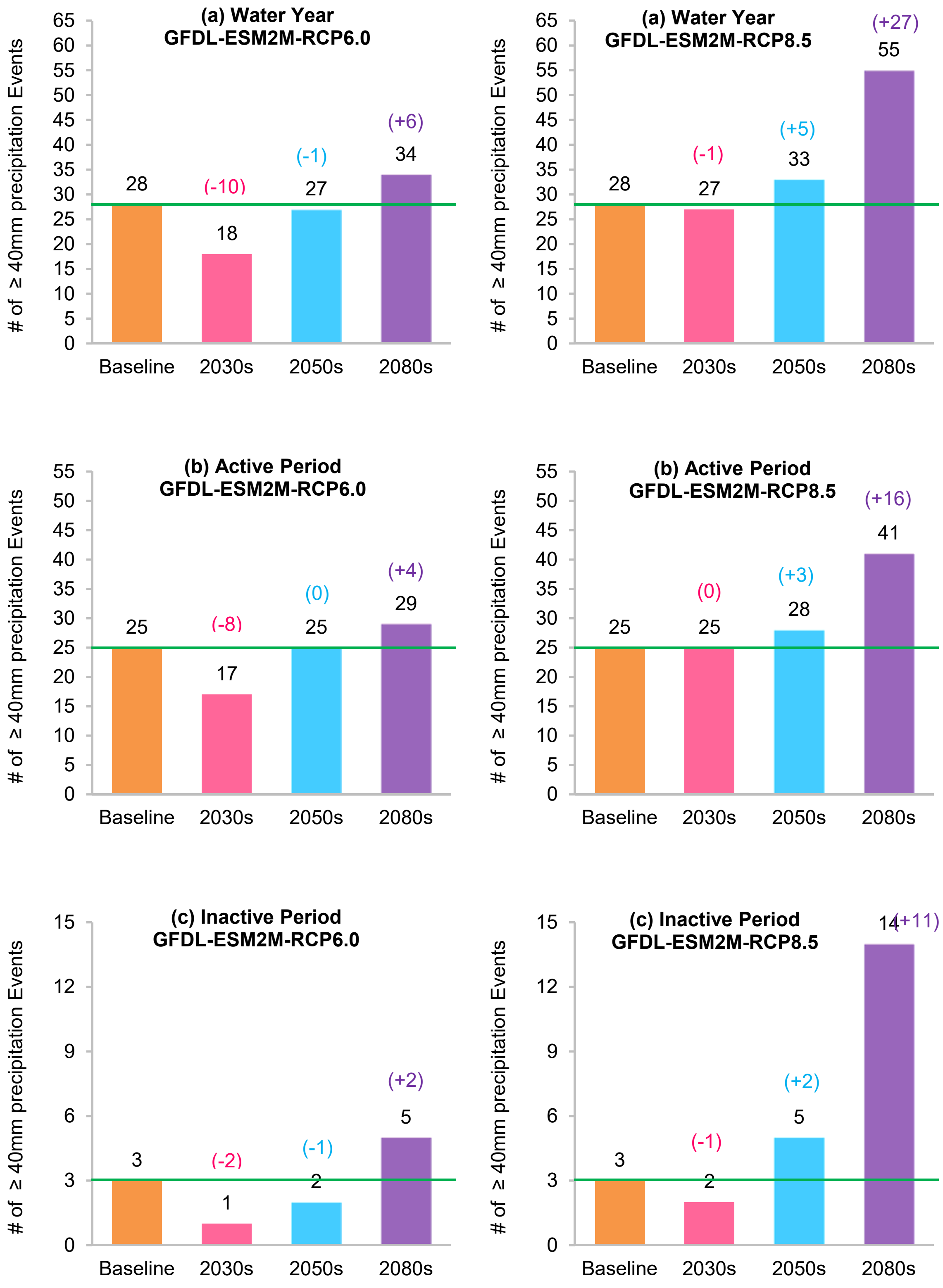

Figure A-23 Projected change in extreme precipitation events over (a) water year, (b) active period, (c) inactive period for the RCP 6.0 and 8.5 of the GFDL-ESM2M model

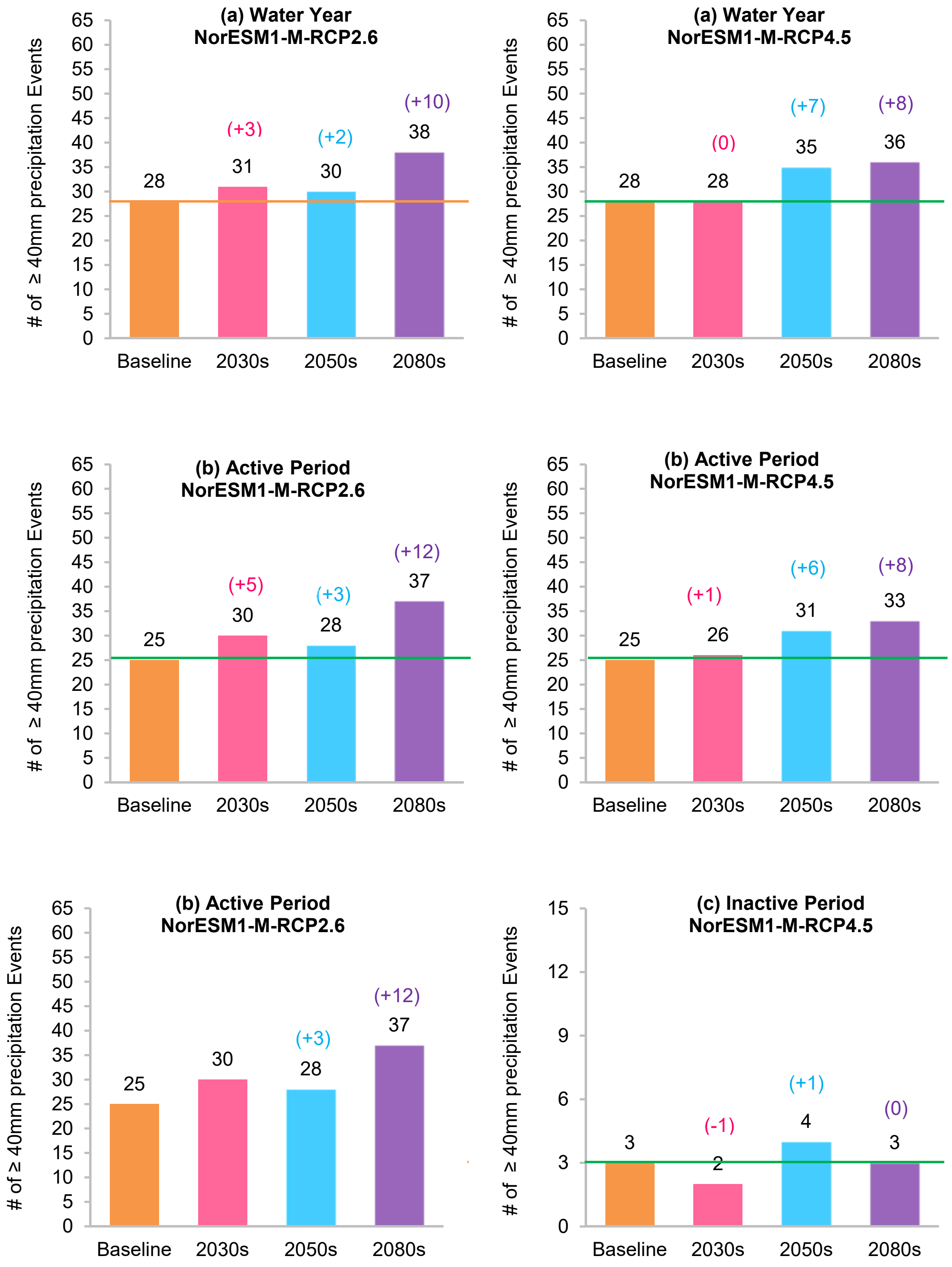

Figure A-24 Projected change in extreme precipitation events over (a) water year, (b) active period, and (c) inactive period for the RCP 2.6 and 4.5 of the NorESM1-M model.

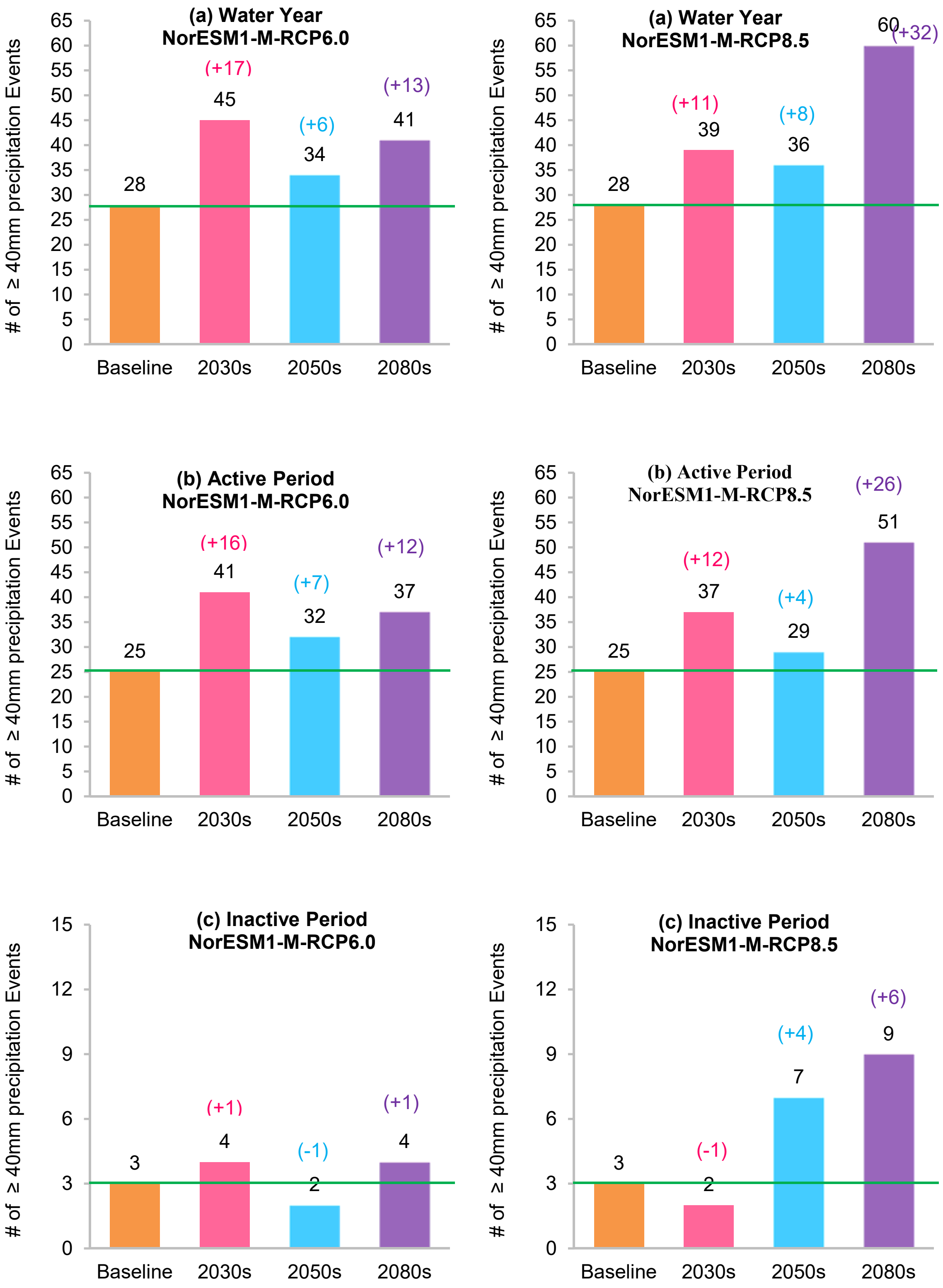

Figure A-25 Projected change in extreme precipitation over (a) water year, (b) active period, and (c) inactive period for the RCP 6.0 and 8.5 of the NorESM1-M model